UNIVERSITA’ DEGLI STUDI DI PARMA

DOTTORATO DI RICERCA IN

" *Ingegneria Industriale*"

CICLO XXXVIII

Prediction of Mechanical Responses of Additively Manufactured Lightweight Cellular Structures

Coordinatore:
Chiar.mo Prof. Alessandro Tasora

Tutore:
Chiar.mo Prof. Fabrizio Moroni

Co-Tutore:
Chiar.mo Prof. Alessandro Pirondi

Dottorando: Mostafa Abolfathi

Anni Accademici 2022/2023 – 2024/2025

To my wife and my family

Finanziato dall'Unione europea
NextGenerationEU

Ministero dell'Università e della Ricerca

Italiadomani
PIANO NAZIONALE DI RIPRESA E RESILIENZA

Acknowledgements

The author gratefully acknowledges that the Project was funded under the National Recovery and Resilience Plan (NRRP), Mission 4 Component 2 Investment 3.3 - Call for tender No. 352 of 09/04/2022 of Italian Ministry of University and Research funded by the European Union – NextGenerationEU.

I am thankful for the guidance of Prof. Fabrizio Moroni and Prof. Alessandro Pirondi throughout this work, whose insights into additive manufacturing processes and structural mechanics shaped both the experiments and to collaborators who contributed to finite-element modeling workflows. Special thanks are extended to Prof. Stefan Heirl from OTH-Regensburg University and laboratory staff and colleagues for support with printing and testing. The author also thanks industrial partners KOSME and KRONES for materials and helpful discussions on design for AM and process constraints. Any remaining errors are the author's responsibility.

Abstract

Predicting cellular structures' mechanical response to meet application needs is a practical and essential investigation in the field of structural engineering, including manufacturing tools and numerical calculations. This thesis establishes the conceptual, technological, and mechanical foundations for two complementary cellular systems: (i) polymeric grid infill fabricated by fused deposition modeling (FDM) using PLA and (ii) metallic lattices—specifically square-honeycomb-type architectures—fabricated by selective laser melting (SLM) using 316L stainless steel. Generally, the framework is on the structural property of cellular materials, focusing on relative density and unit-cell topology.

Firstly, experimental multi-axial compression of PLA infill cubes through infill ratios and raster angles has been made to quantify the role of raster angle and infill ratio on the stiffness of transversely isotropic lattices. Additionally, by multi-scale finite-element models with conventional modeling and a more sophisticated approach, integrating micro/meso/macro unit cells under periodic boundary conditions, a numerical methodology was used to increase the accuracy in predicting the mechanical behavior, while keeping the modeling complexity moderate.

Afterward, an internally pressure-loaded metallic cylindrical lattice was tested to link geometry, process constraints, and realized stiffness. This research started with designing a prototype of cellular architected SLM 316L honeycomb. A specific test rig was provided to apply pneumatic/hydrostatic pressurization on the 3D printed specimens. To understand the homogenized behavior of the target cells, a multi-directional compression test was carried out. While experimental data provided an overall behavior of the structure, FEM was used to get additional information about the deformation and stress distribution.

The thesis combines design, experiment, and simulation to deliver an industrial-level roadmap to predict mechanical behavior in AM cellular structures. Connecting the employed methodologies is beneficial to respond to industrial problems and make the use of new and advanced technologies in manufacturing with less risk and faster results.

Contents

List of figures

List of tables

Nomenclature

AM	Additive Manufacturing
FDM	Fused Deposition Modeling
SLM	Selective Laser Melting (laser powder bed fusion for metals)
PLA	Polylactic Acid (thermoplastic polymer)
ABS	Acrylonitrile–Butadiene–Styrene
IR	Infill Ratio (infill volume divided by total volume, %)
RA	Raster Angle (deposition orientation, e.g., 0°/90°, −45°/45°)
UC	Unit Cell (repeating cell of the cellular architecture)
RVE	Representative Volume Element
RVU	Representative Volume Unit cell
PBC	Periodic Boundary Conditions
E_eq	Young’s modulus; homogenized/nominal elastic modulus
DIC	Digital Image Correlation
CAD	Computer-Aided Design
FE / FEA	Finite Element / Finite Element Analysis
PF	Peak Force
MF	Mean Force
TPMS	Triply Periodic Minimal Surface
PU-TFA	Piecewise-Uniform Transformation Field Analysis
OM	Optical Microscopy
SEM	Scanning Electron Microscopy
μCT	Micro-Computed Tomography
SEA	Specific Energy Absorption
BCC	Body-Centered Cubic
BFCC	Body-Face-Centered Cubic
FCC	Face-Centered Cubic
BD	Building Direction (layer-stacking direction in AM)
BO	Build Orientation

NUS	Non-Uniform Section
CT	Cell Thickness
CW	Cell Width
ID	Inside Diameter
OD	Outside Diameter
NCC	Number of Cells in Circle
NCS	Number of Cells in Stiffeners
HS	Height of Stiffeners
SD	Stiffener Depth
SW	Stiffener Width
RC	Rectangular Cube

Chapter 1

Introduction

This thesis examines two complementary AM routes for load-bearing cellular architectures: (i) fused deposition modeling (FDM) of polylactic acid (PLA) with engineered internal infill patterns; and (ii) selective laser melting (SLM) of 316L stainless steel to fabricate metallic lattices, including regular square-honeycomb-type architectures. These choices span polymeric and metallic materials, allowing us to contrast extrusion-driven anisotropy in infills with melt-pool physics and geometric fidelity in SLM lattices. Both families show the same physics: global beam/plate response couples to local unit-cell mechanisms, where defects and geometric fidelity play an important role. Infill patterns in weight, cost, and speed are critical. In mechanical fixtures, covers, and consumer products, infill pattern and density provide a rapid way to change stiffness, strength, and damping without changing outer geometry. In domains like robotics, prosthetics, transport housings, and protective enclosures, this lets the designers trade print time and mass for performance with clear, reproducible rules. SLM 316L has higher strength, temperature capability, and durability. SLM technology has more freedom in designing, and with close mechanical response to its conventional rival is a great choice for the components that are hard to manufacture or assemble in machinery design, biomedical parts, food industry, and so on. In the following, the two manufacturing technologies with their representative investigated structures are presented to give an idea about the whole study.

1.1 FDM technology

Additive manufacturing (AM) builds parts layer-by-layer from sliced digital models, enabling complex internal features, rapid iteration, and part consolidation beyond what is possible with conventional methods. In practice, the promise of freedom in geometry comes with a new set of process–structure–property links: bead paths, layer height, and thermal history govern bonding, voids, and anisotropy, so the printed part rarely matches the bulk feedstock’s datasheet properties. Among AM routes, FDM remains the most accessible. A thermoplastic filament is heated to a viscous state and extruded along programmed toolpaths, forming shells and infill in layer-by-layer runs. Strength and accuracy are therefore sensitive to parameters such as raster angle, infill density/pattern, layer height, nozzle temperature, and build orientation. Reviews converge on a few robust messages: avoid upright ("Z-oriented") loading for tensile parts; co-optimize raster width and air gap to improve inter-run bonding [1-3]. In Figure 1.1, the schematic of the FDM process is shown, indicating the section view of the fabricated layers.

While FDM has low cost and broad material availability, easy to use for rapid prototyping and functional polymer parts, straightforward post-processing for support removal and finish improvement when needed, the studies found the following disadvantages:

- Resolution and dimensional accuracy are limited relative to some other AM processes; surface roughness and stair-stepping can appear.
- Layer-wise bonding leads to anisotropy; voids and insufficient inter-run fusion reduce strength.
- Mechanical properties are sensitive to settings (temperature, layer thickness, infill, orientation, speed), so results can vary and require optimization [1, 2].

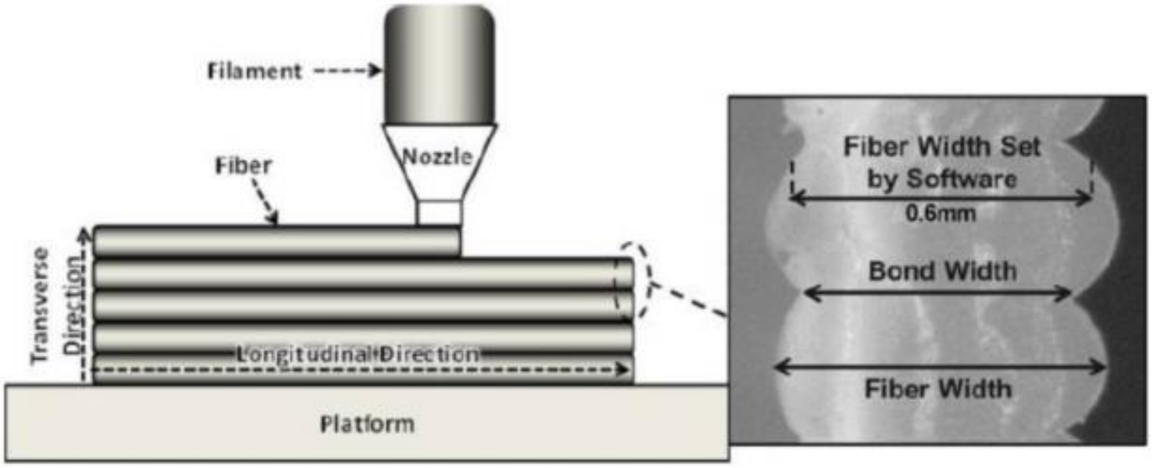

Figure 1.1 Schematic view of deposition of fibers in FDM technology [1]

PLA has become a leading FDM material due to its printability (lower extrusion/bed temperatures, reduced warping), bio-based origin, and relatively low particle emissions during printing compared with some alternatives. PLA often exhibits higher stiffness and strength than ABS in tension—though it is more brittle—and its properties remain strongly direction-dependent because fracture and damage localize along filaments and interlayer interfaces [4, 5]. A recurring feature in PLA prints is anisotropy: the same coupon can behave differently in tension vs. compression and along different build directions. Experimental campaigns document asymmetry between tensile and compressive responses and identify buckling thresholds that depend on slenderness and the compressive modulus rather than the nominal material constants. Under compression, tangent-modulus-based estimates—when calibrated with compressive data—provide conservative but useful predictions, while non-linear finite element models match tests closely [6, 7].

At the process-parameter level, studies that combine mechanical tests with thermal and morphological diagnostics show consistent trends. For neat PLA, higher infill density generally increases Young’s modulus. SEM evidence attributes failures to voids and the lack of fusion between adjacent filaments or layers; parameter tuning reduces these defects and lifts properties [8]. Meta-reviews similarly emphasize that parameter interactions matter (e.g., layer height with raster angle; raster width with air gap), and that orientation away from the Z-build direction is advantageous for tensile strength [1-3]. For multi-criteria optimization (strength, stiffness, toughness, resilience), Taguchi–GRA approaches highlight that nozzle diameter and cell geometry can be dominant contributors, not only density and layer height [9].

1.1.1 Infill structures

What distinguishes AM parts from conventionally made polymers is not only the layer-wise history, but the intentional interior architecture—the “infill”—that the slicer (a software which elaborates the 3D model to be sent to the FDM printer) writes between outer shells. Because the infill sets local load paths, porosity, and failure trajectories, two parts made from the same filament can behave very differently in service. As a result, the right question is rarely “which material?” alone; it is “which infill, at what density, with what shell strategy and orientation for the intended loading?” [10-17]. In Figure 1.2, a 3D printed structure included an infill is experimentally and numerically compared. Considering this as an example, the curiosity was raised to find a fast, confident, and comprehensive method to predict the infill effect on the structural stiffness. This type of study on other structures, such as Carabiner-like geometry, was performed. In this research, they tried to highlight the interaction of density with build orientation: X/Y-oriented builds leverage better shear and road-overlap load paths and scale well with density; Z-oriented parts, in contrast, can still fail by interlayer debonding even at 100% infill [18].

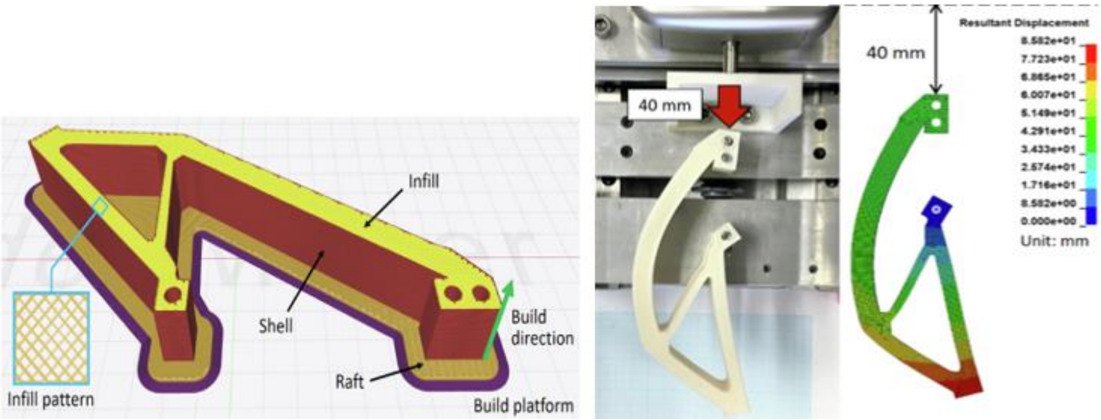

Figure 1.2 3D printing model of the compliant finger (left), the comparison between displacement contours from the FEA, experimental results (right) [13]

Most works follow established standards for tension, bending, compression, and impact when possible, adapting geometry to printed coupons. A typical study prints a series of dog-bones or rectangular beams with clear tables of parameters (nozzle temperature, line width, layer height, shells, raster angle, pattern, density), reports ultimate strength, Young’s modulus, and strain at break, and documents fracture surfaces and gauge-section features. By altering pattern (e.g., rectilinear, triangular, honeycomb, concentric, gyroid) and relative density, designers balance stiffness, strength, mass, print time, and even energy absorption without changing the outer shape. In Figure 1.3, fourteen types of infills for the cylindrical specimens are shown, which were compressed to compare their mechanical responses. Several papers analyze compression using ASTM-type cylinders or blocks to avoid thin-beam buckling and to evaluate energy absorption and plateau behavior, both essential for structural and protective applications [14-17, 19-22].

Experiments consistently show that pattern geometry changes the dominant failure mode and the efficiency of load transfer through filaments and interfaces. In tension and bending, rectilinear/grid arrangements often achieve high apparent modulus/UTS along the main run directions, while triangular/honeycomb patterns can trade some tensile metrics for improved impact energy and more gradual damage progression. Concentric infill can excel when the load aligns with the contour, because long, nearly continuous filaments follow the outer profile and provide crack-deflection barriers. Under compression, honeycomb-like and other cellular patterns produce stiff load-bearing webs with stable plastic-like plateaus; comparative surveys across many patterns provide “mechanical inventories” that designers can use for early trade-offs [10-12, 14, 15, 20-24].

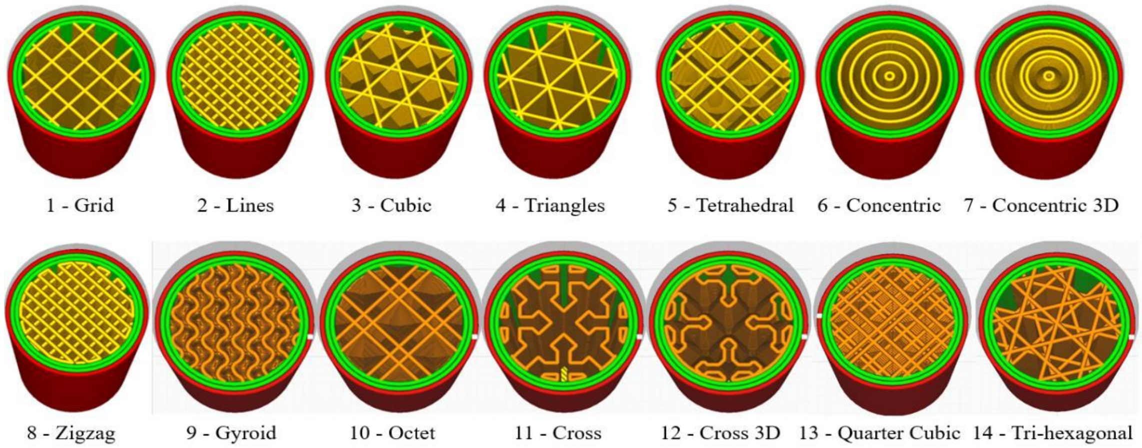

Figure 1.3 Different infill patterns inside cylindrical specimens for compression test [20].

In device-oriented optimization (e.g., implants/lattice cores), “compromise” densities around ~40–60% with appropriate cell shapes and adequate shell counts are frequently selected to maximize stiffness per mass and to control local stress concentrations. Studies show that modest upsizing of cells can reduce print time dramatically with only small stiffness penalties, but too large a cell introduces longer unsupported spans and stress concentrations, affecting both strength and repeatability. This feature-size effect is important because it interacts with layer height and bead width: you cannot rely on density alone to predict performance when the geometry of the repeating unit changes [11, 25, 26]. Another research tried to define geometric parameters of the unit cells for different infills to shape the comparison method (see Figure 1.4).

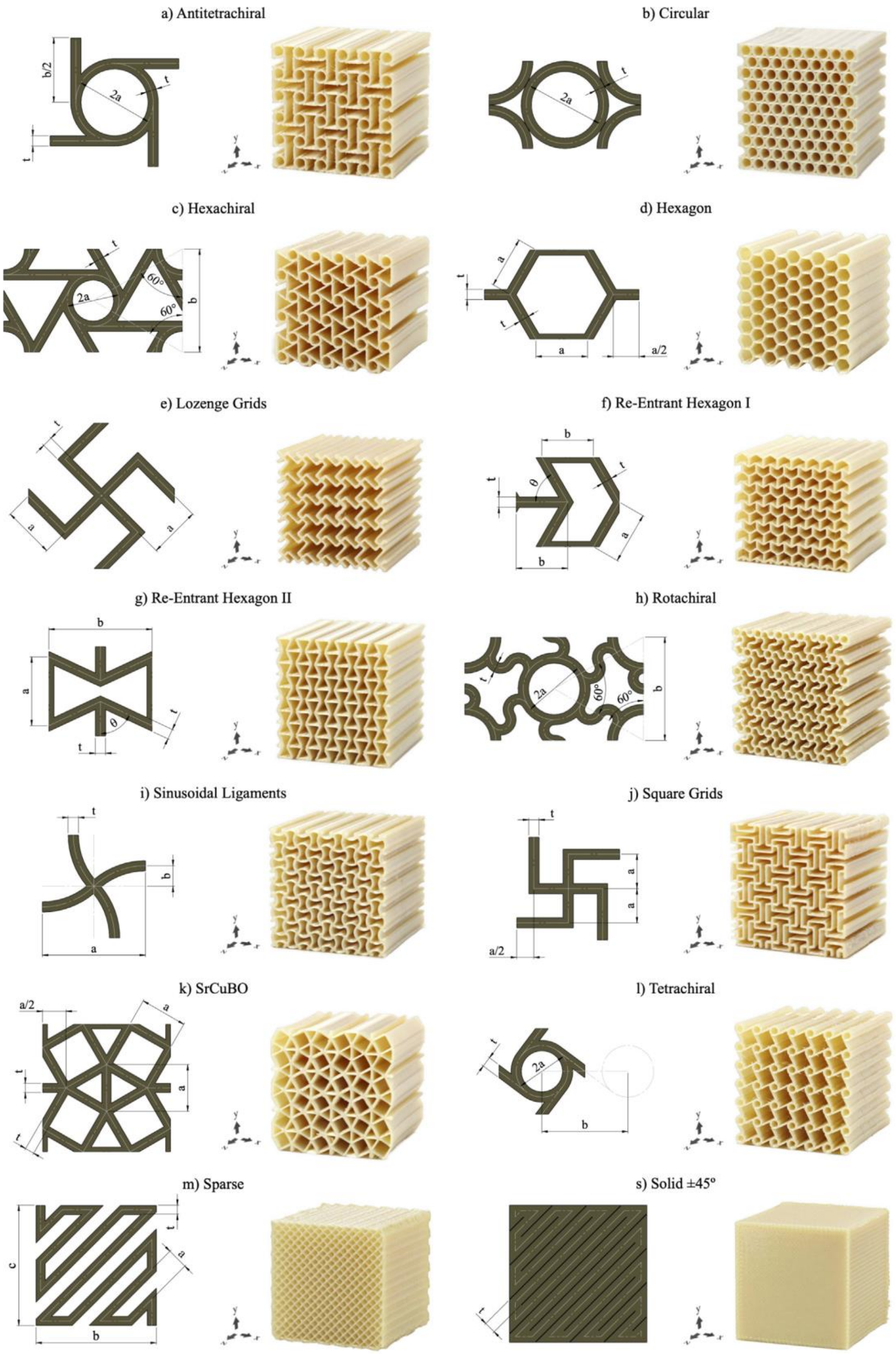

a) Antitetrachiral

b) Circular

c) Hexachiral

d) Hexagon

e) Lozenge Grids

f) Re-Entrant Hexagon I

g) Re-Entrant Hexagon II

h) Rotachiral

i) Sinusoidal Ligaments

j) Square Grids

k) SrCuBO

l) Tetrachiral

m) Sparse

s) Solid ±45º

Figure 1.4 Unit cell shapes design and corresponding FDM manufactured sample of each infill pattern assessed [25].

Raising infill density increases the amount of load-bearing material and tends to reduce porosity, lifting absolute stiffness and strength. However, specific properties (per mass) can peak at intermediate densities when shells carry a large share of the load and when pattern topology resists efficiently [10, 11, 13, 15, 19]. Several PLA-focused works report near-linear gains in modulus with density, while strength improvements saturate earlier if failures localize at interlayer interfaces or poorly fused filaments [14, 19]. Pattern–performance rankings are one of the scenarios. A pattern that is optimal in tension may not be the most efficient in compression or impact. The grid pattern, as the most relevant pattern, was studied under different densities (see Figure 1.5) [11]

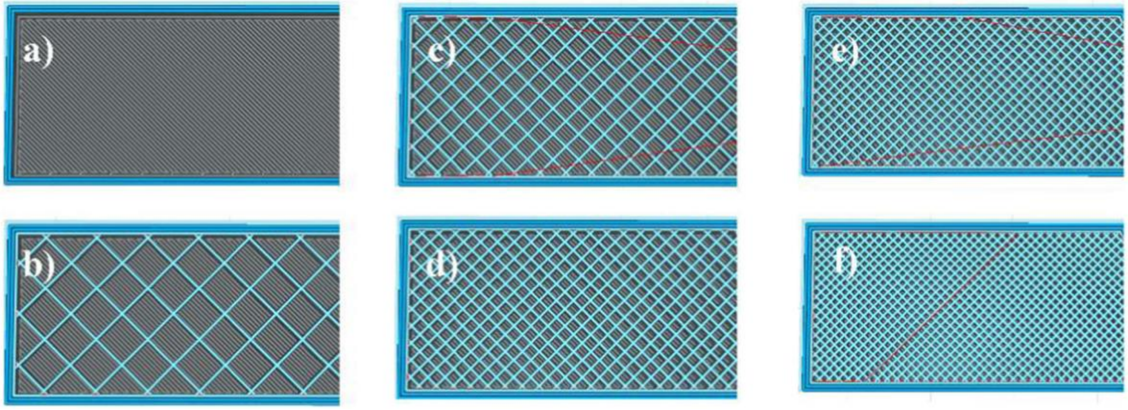

Figure 1.5 Grid pattern with different infill ratios; a) 0 %, b) 20 %, c) 40 %, d) 60 %, e) 80 %, f) 100 % [11].

Multiple publications emphasize that outer shells (contours) and top/bottom covers are not passive [18, 27-30]. The contour—filaments aligned with the perimeter—can be very stiff along the path; the cover—typically crossed raster—can behave quasi-isotropic in its plane; and the inner infill is anisotropic to a degree set by pattern and density. Partitioning a printed component into these three regions and characterizing each region’s apparent properties (testing for contour and cover; homogenization or sub-volume tests for infill) explains many apparent contradictions across coupon data and dramatically improves predicting the model’s behavior [27, 28]. The build orientation then decides how these regions stack through thickness and where interlayer interfaces sit relative to the principal stress state, which is why orientation and shell count are so influential in part-level tests and redesign studies [18, 29, 30].

A method formalized for FDM splits the structure into external partitions (aligned/crossed filaments) characterized experimentally, and an inner infill characterized via computational homogenization of a pattern RVE under periodic boundary conditions [27]. The partition properties (orthotropic stiffness, strength surrogates) are mapped into the macro FEA mesh. This has been shown to reproduce global responses while drastically reducing experimental burden [27]. With a credible apparent-property model in place, one can perform FEA-based optimization of pattern, density, cell size, and shell count against multiple objectives (stiffness, strength, energy absorption, mass, safety factor). Studies demonstrate optimization at part scale (e.g., a compression-tested bracket/model) using finite elements to guide the infill settings that meet performance targets under practical constraints [27, 28, 31].

1.1.2 Multiscale simulation and RVEs

FDM components create a mesostructured inside the part: oriented lines (“filaments”), stacked layers, and unavoidable pores. Experiments and modeling show that these printed “plies” behave like orthotropic laminae whose stiffness and strength depend on raster angle, layer thickness, and local bonding [32]. Before we homogenize anything, we need a clear picture of the void system that this process leaves behind. In Figure 1.6, the construction of the laminate in creating the voids is shown. A focused review classifies three dominant families—raster-gap, interlayer, and intra-bead voids—links them to process parameters, and summarizes imaging/quantification protocols (OM/SEM/µCT) and their impact on properties and reliability [33].

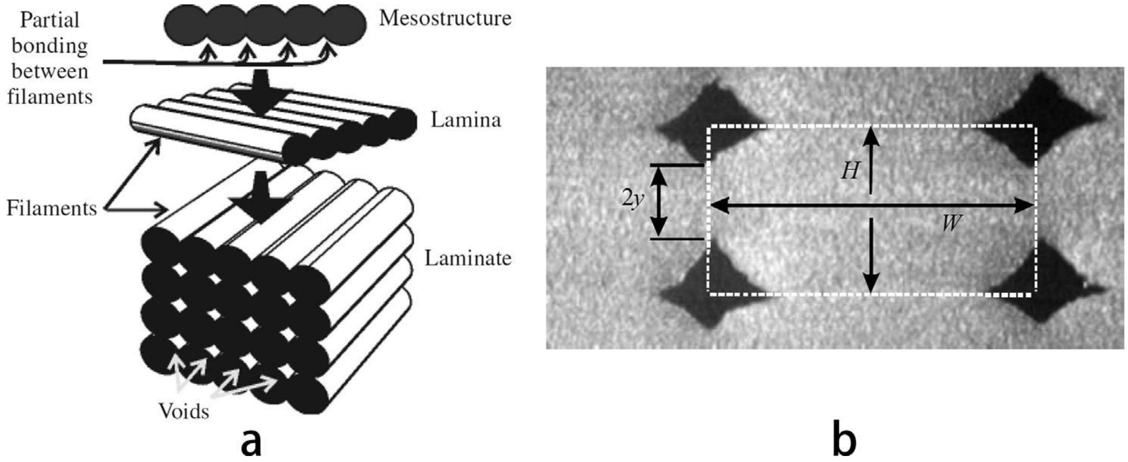

Figure 1.6 Demonstrating FDM meso-structure, lamina, and laminate to show how the voids appear [33].

FDM parts are architected across three coupled scales: (i) micro (filament material, bead–bead interfaces, voids), (ii) meso (raster layout/unit cell, infill pattern), and (iii) macro (the full component and skins). Predictive models that capture flexure, crash/energy absorption, or tensile performance, therefore link unit-cell mechanics to part-scale response via homogenization and scale bridging [34-36]. For printed cellular cores, the route is: measure/define polymer properties (micro) → homogenize the chosen lattice/infill (meso) → simulate beam/plate response (macro). This was used to dissect how skin rigidity steers a cellular beam between “morphing-like” and “sandwich-like” bending—making skins a first-order design parameter, not an afterthought [34]. Extract the repeating unit from CAD/μCT, characterize filament elasto-plasticity, run nonlinear macro analyses with/without homogenization, and compare responses—giving engineers a side-by-side accuracy/cost trade-off when deciding between detailed vs. homogenized models indicated in (Figure 1.7) [35].

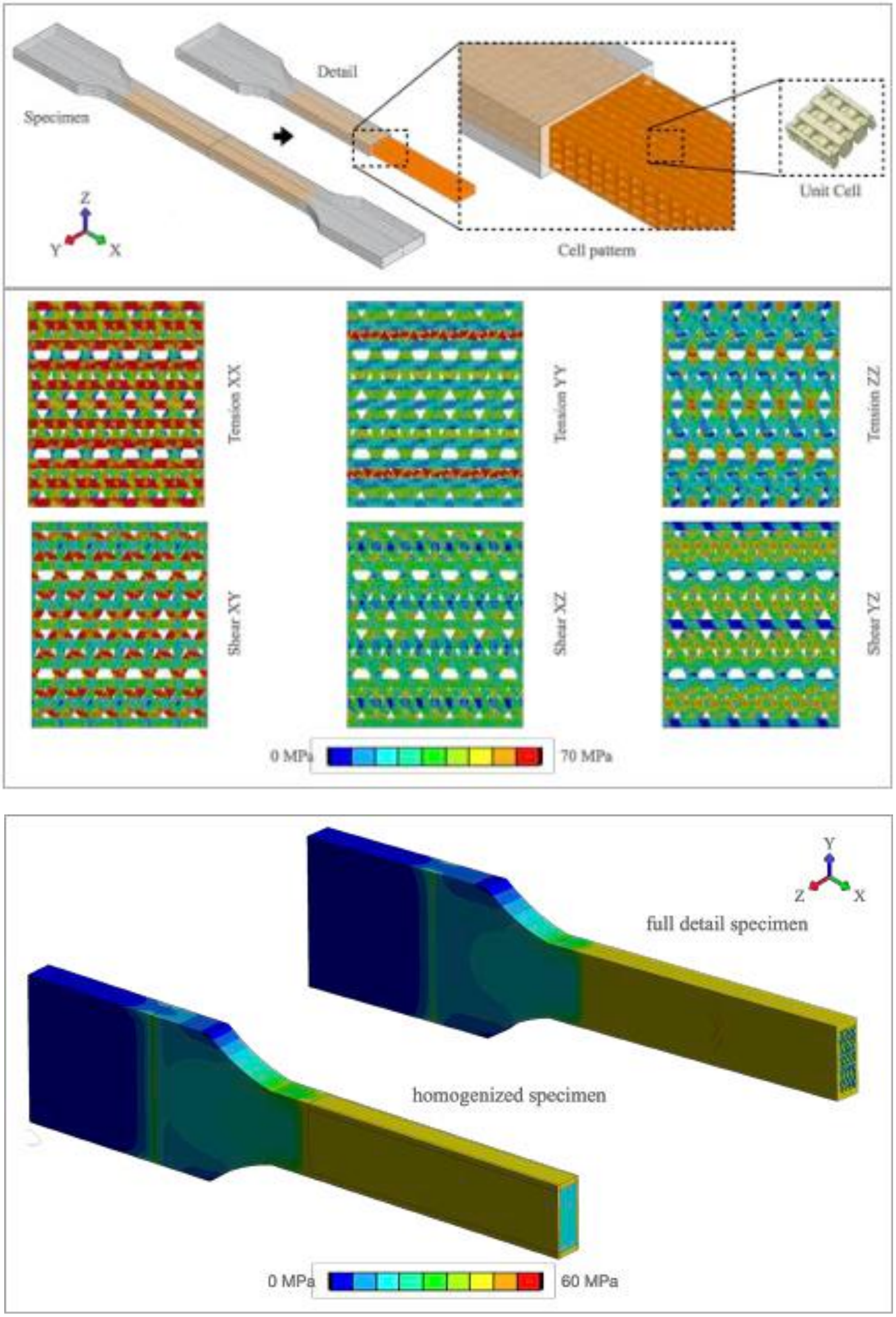

Figure 1.7 Cell structures and stress state of the selected unit cell to find homogenized properties [35].

A complementary, end-to-end path is shown in Figure 1.8. This study has experimentally characterized the printed mesostructured and directional properties. It builds a unit-cell/meso model that reflects the measured geometry and void content. Moreover, homogenize to orthotropic constants, and validate macro FEA predictions against tensile/bending tests. This characterization → homogenization → validation loop makes the multiscale link reproducible and quantifies when homogenization is accurate enough for design [37].

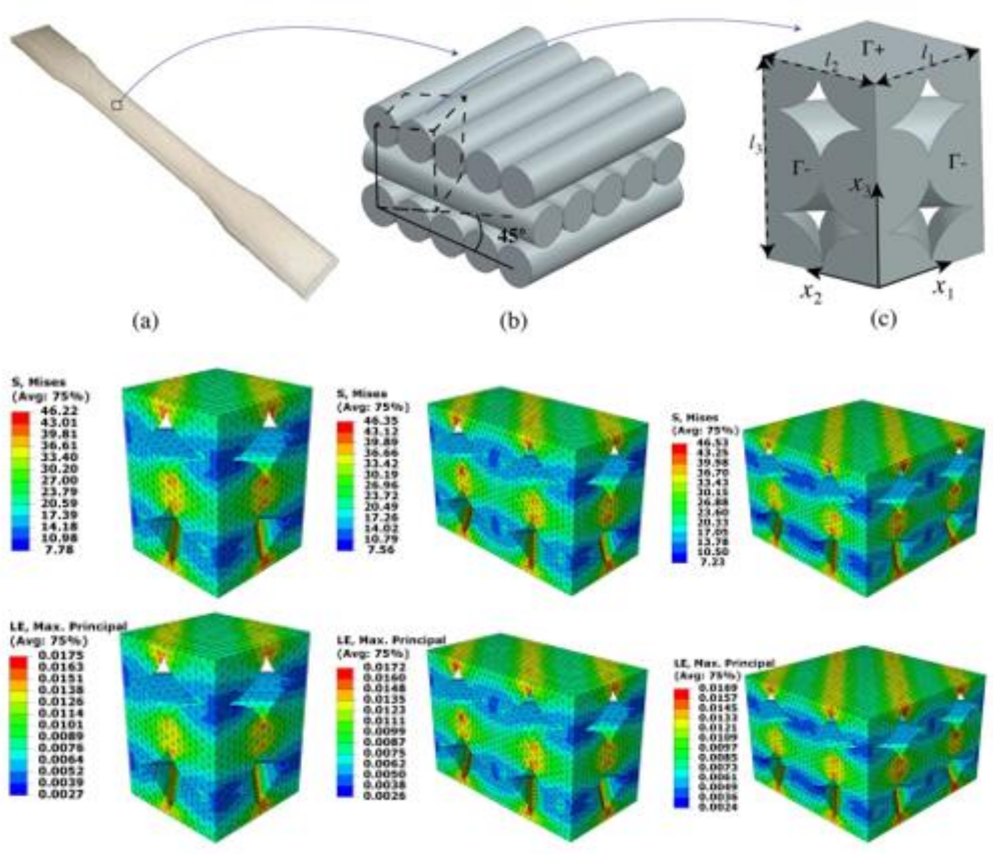

Figure 1.8 Multiscale levels of FDM 3D printed samples, indicating the stress and strain contour using FEM [37].

A process-aware view connects settings to structure and, in turn, to properties. A thermal–sintering framework predicts neck growth between adjacent lines, the evolution of porosity with layer height and environment temperature, and the resulting changes in stiffness/strength. The study closes the loop: manufacturing conditions → bond/void state → mechanical response, supplying calibrated inputs for design and simulation [38]. Directional testing across raster families (unidirectional and bidirectional) shows that classical laminate mechanics, including first-ply failure, captures elastic anisotropy and layup effects in FDM coupons; varying lamina thickness and layup order shifts tensile and flexural responses in predictable ways [39]. This provides the experimental baseline and the language we pass to multiscale models. The next step is unit-cell (RVE) homogenization. One route builds periodic RVEs of typical 0/90° or patterned cells and sweeps infill density, layer height, and orientation to obtain orthotropic moduli and response surfaces—fast tools for early screening [40]. For failure realism, an enhanced scheme inserts cohesive interfaces at filament junctions within a periodic cell; homogenized response and failure agree with tests within reported confidence bounds and separate intra- versus interlayer damage mechanisms. The resulting constants map cleanly to part-scale FE models [41].

These homogenized properties feed constitutive descriptions for structural analysis. A numerically derived stiffness matrix that reflects printing direction, build orientation, and layer thickness enables consistent stress prediction for different regions of a part (contour, cover, interior) [42]. Printed short-fiber composites demand extra caution: RVE-predicted moduli can exceed experiments, with the gap larger in sCF systems than in neat polymers due to delamination and fiber pull-out; this informs safety factors and model selection (e.g., transverse isotropy at the lamina scale) [43]. For broader scale-bridging, asymptotic homogenization provides an analytical pathway. Treating the microstructure (solid matrix + voids, or reinforcement within a matrix) as the fine scale, the method delivers macro-level effective constants and offers a way to embed infill ratio and pattern effects without resolving every road at part scale [44]. It complements computational RVEs and clarifies parameter dependencies.

Elastic orthotropic from periodic unit cells (0/90, ±45, or lattice topologies) feeds the macro model; nonlinear response at the macro level is then computed with those effective properties. This has been demonstrated for tensile specimens (procedural CIRP study), with comparisons of “full-detail” vs homogenized models to quantify modeling error and speed-ups [35]. For cellular beams, three-scale simulations recover measured flexural trends and show that apparently contradictory literature on “shear-dominated vs axial-dominated” core behavior is reconciled once skin stiffness is varied in the macro problem [34]. For PETG/carbon unit structures (triangles, hex, re-entrant), an experimental–numerical program maps how infill density, layer thickness, and pattern shift tensile/flexural/compressive properties, with FE confirming which patterns translate reinforcement into real gains—evidence that unit-cell modeling plus tests is a reliable route for design rules [45]. For composites, RVEs that include reinforcement and voids across scales (micro fiber–matrix, meso voided raster, macro lay-up) recover elastic constants with good agreement to analytical models and tests; simplified analytical micromodels can replace Mori–Tanaka in some cases, and stochastic RVEs with real fiber contours capture the effect of non-circular, jagged perimeters on effective moduli [46, 47].

Beyond polymers, a metal-FDM (BPE/FDM-like) study uses digital-twin FEA with SEM-measured porosity to quantify the tensile penalty of triangular infill vs solid (see Figure 1.9). This study shows that the same multiscale logic (unit-cell geometry + porosity → macro response) applied before for polymers works for metal filaments too [48].

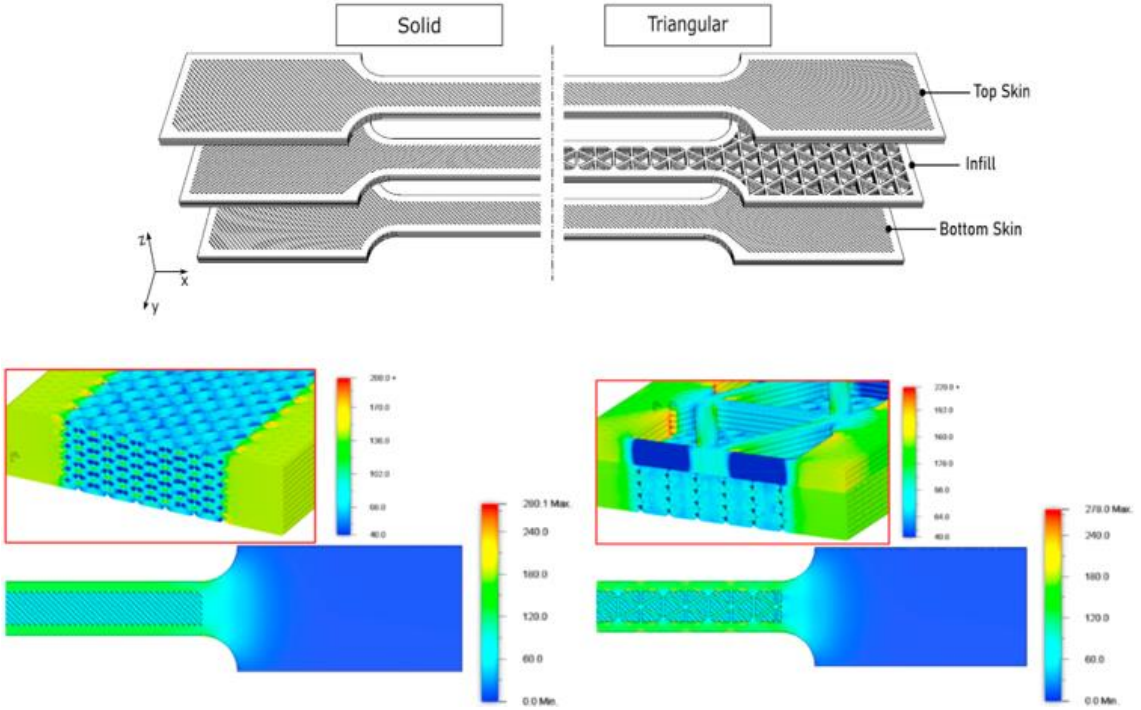

Figure 1.9 Layup of skin/ wall and infill with their representative FEM for metal-FDM [48].

1.2 SLM technology

Selective Laser Melting (SLM) builds near-net-shape components by spreading a thin powder layer, melting and fusing selected areas with a high-energy laser, then repeating layer by layer until the part is complete. The main idea of the process is shown in Figure 1.10. Supports are added for overhangs, printing occurs in an inert atmosphere, loose powder is removed, and the part is separated from the substrate after the build. Process parameters such as laser power, scanning speed, hatch spacing, and layer thickness govern fusion between tracks and layers. SLM can fully melt powders and produce fully dense parts, but surface roughness, thermal gradients, residual stress, and anisotropy are important considerations that often motivate post-processing and parameter optimization. In the following main advantages and disadvantages are mentioned:

- Fully dense near-net-shape components, improved product quality, and automated CAD-to-part workflow.
- Ability to manufacture complex geometries without molds and with high dimensional accuracy; reduced production time and material utilization benefits.
- Surface roughness (stair-stepping/track texture) often requires post-processing.
- Thermal gradients → residual stress, cracking/delamination, and anisotropic properties if not controlled.
- Equipment speed/size limits and powder-related defects/porosity that require careful process control [49].

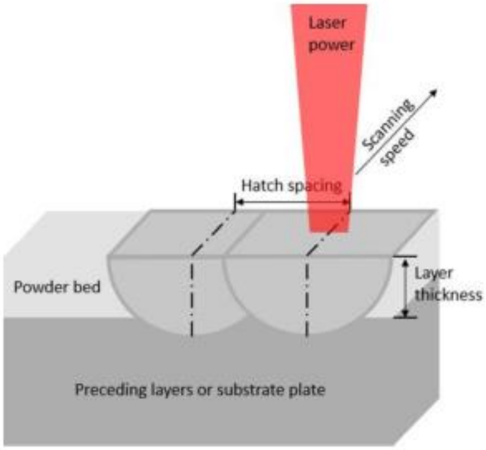

Figure 1.10 SLM process parameters: laser power, scanning speed, hatch spacing, and layer thickness [49].

1.2.1 Lattice and cellular structures

Lattice and cellular structures replace bulk material with periodic networks of struts or shells to achieve high specific stiffness/strength and controlled energy absorption at a given mass. Common families—honeycombs (three different honeycombs are shown in Figure 1.11), truss lattices (e.g., octet/Kagome), and TPMS/shell lattices—carry load differently. To categorize them, it could be mentioned that stretching-dominated trusses are efficient for peak stiffness and strength; shell-type cells favor stable, progressive collapse and high specific energy absorption (SEA) [50-52]. In practice, component response blends global bending/shear of the structure with local unit-cell mechanisms. As load increases, deformation can migrate from distributed member work to node-dominated softening, which explains why joint radii and junction quality control post-yield behavior and repeatability [53].

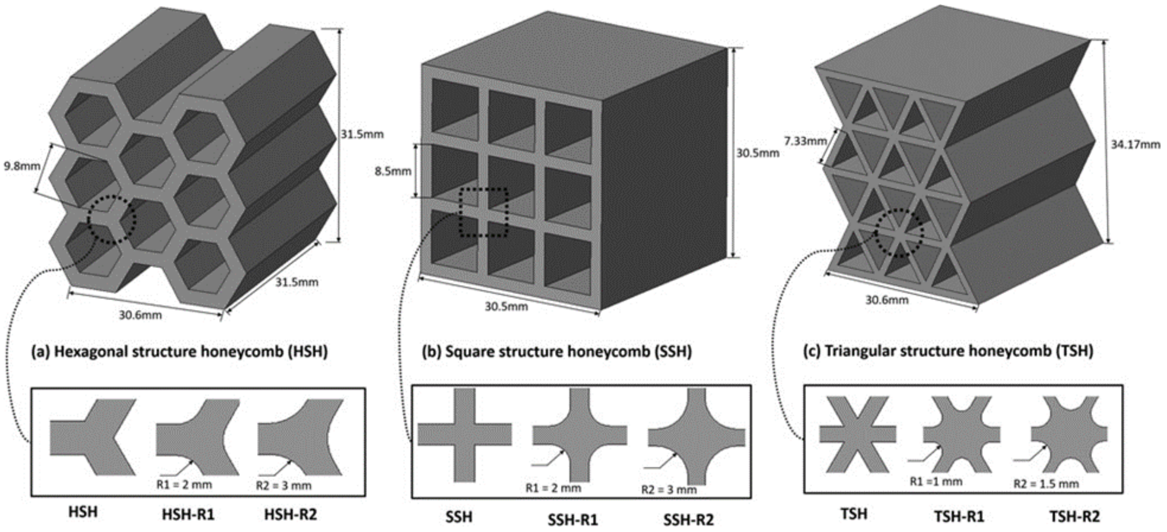

Figure 1.11 The illustration of the design methodology of three different honeycomb structures with uniform and variable material distribution by adding fillets at the edges [53].

1.2.2 Manufacturing and experiments

Real parts are never CAD-perfect. Imperfections—surface roughness, strut waviness, node flaws—reduce stiffness/strength and can alter the collapse mode. One common method for simulation is to generate a reconstructed model by combining the designed and as-built models (see Figure 1.12). Experiments and defect-aware simulations show measurable knockdowns and identify node defects as first-order drivers, which should be reflected in design margins and in unit-cell models used for prediction [54, 55]. These realities motivate the choice of SLM for metals: it provides geometric freedom and high density for internal architectures, with 316L stainless steel widely used thanks to a favorable blend of printability, ductility, and corrosion resistance. Orientation and thermal history govern bulk allowables; large builds add scan-field/overlap effects that matter when lattices span multiple fields [56-58].

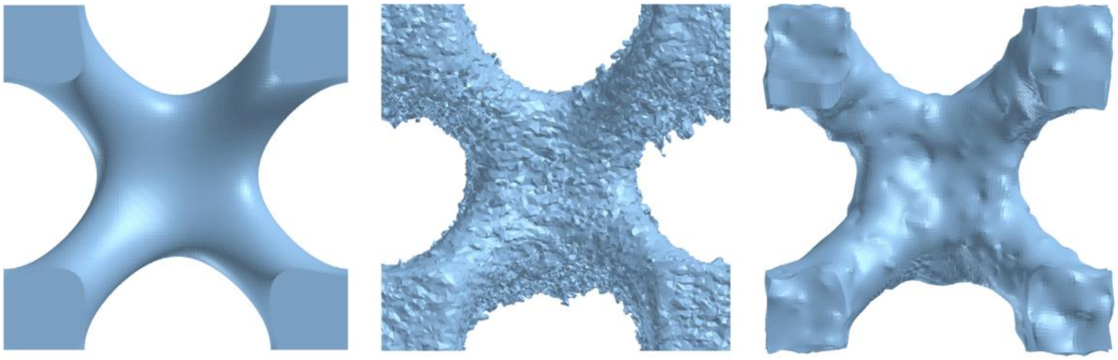

Figure 1.12 Side view of a unit cell in as-designed, as-built, and reconstructed configuration. The building direction (BD) is upward [54].

Within SLM 316L, experimental studies consistently find that sheet-type TPMS (e.g., gyroid) deliver smoother plateaus and higher SEA than skeletal forms at the same relative density, while truss lattices maximize initial stiffness/strength when load paths are aligned [59-61]. Impact/Charpy benchmarks show explicit FE captures trends but can be conservative on peak force/energy without calibrated contact/damage parameters—useful for trimming test matrices before printing [62]. Cross-alloy comparisons confirm that 316L's ductile collapse supports repeatable energy absorption, although alloy choice interacts with topology and cell size [60].

1.2.3 Hybrid structures and simulation methods

Hybrid structures are engineered systems that intentionally combine two or more different materials or architectural concepts. Manufacturing these types of structures helps to achieve performance that a single material or topology alone cannot provide. In Figure 1.13, a hybrid lattice combining two FCC-based cells (FCC with diagonal supports and FCC with cross supports) inside one structure, printed in 316L stainless steel by laser powder bed fusion. Subsequently, mechanically tested it in compression and three-point bending. Hybrid structures were studied on TPMS structures, such as Primitive, Gyroid, and IWP inside one specimen, keeping constant overall size and density. Combining different unit-cell topologies can be used to tune stiffness, strength, energy absorption, stability, and multifunctionality. It enables localized tailoring of deformation and supports application-specific lightweight structures in aerospace, biomedical, and impact protection [63-65].

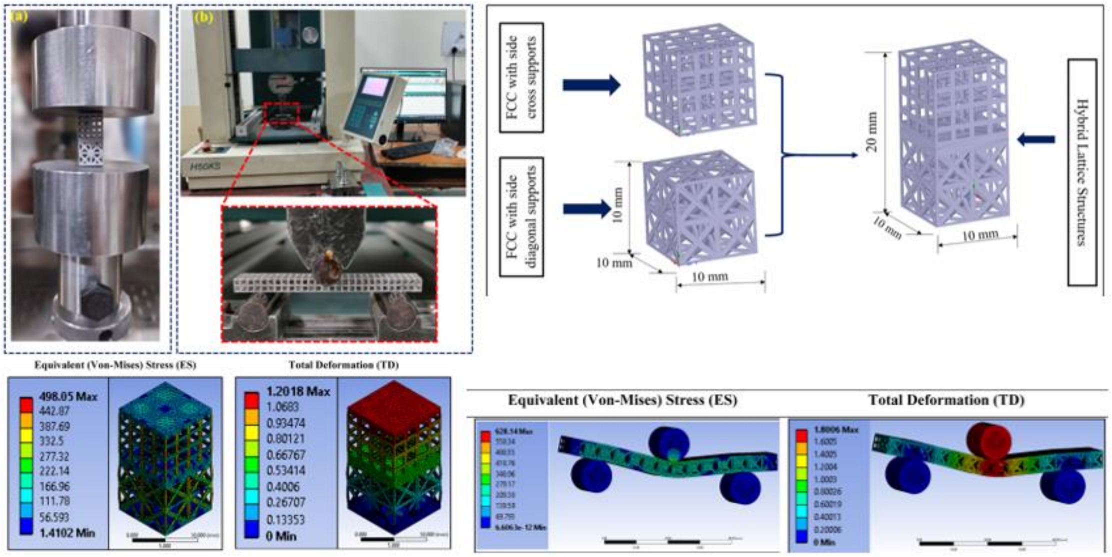

Figure 1.13 An example of a hybrid model of FCC lattice with the experimental view and FEA results [64]

To model SLM lattices, it is most effective to start at the unit cell level. A cell-level finite-element model recovers elastic response, yield onset, and collapse modes under the same loading paths we test experimentally. When local details (plastic hinges at nodes, shear bands in short members) matter, solid elements are preferred; when we only need global trends across many geometries, beam/strut models enable fast parametric sweeps. Small geometry choices at the cell—node fillet radius, strut taper, junction blending—shift stiffness and the post-yield path, so the cell CAD must reflect the manufactured shape, not an ideal sketch [66-68].

Predictions stabilize only after enough cells are included in the model. FEA and tests show stiffness/strength convergence with increasing cell count, while the end boundary conditions can bias the first layers if they are too stiff or too soft. As load rises, deformation often migrates from distributed member work to node-dominated softening. Recognizing this helps us place reinforcements or adjust transitions in graded parts so that collapse remains progressive rather than abrupt. Cell-level models are most accurate when the dominant mechanism of the chosen topology (stretching vs. bending) is represented at the meso-scale and when the material law matches metallic behavior. Using an appropriate elasto-plastic model at the strut level (with calibrated yield and hardening) brings peak stress and plateau shape close to measurements in metallic micro-lattices. This alignment makes it possible to transfer parameters across similar cells and speeds up later studies. Ideal CAD tends to over-predict strength. In practice, modest increases in node fillets or realistic taper can change the collapse sequence in FEA in the same direction as the experiments report [66-70].

Lightweight lattice structures were investigated with different materials, technologies, and methodologies. Using PA12 by multi jet fusion (MJF), a particular lattice was modeled through elastic–plastic homogenization so that its anisotropic stiffness, yield, and hardening could be treated as an equivalent continuum instead of resolving every strut in FEM. Another study, lattice architectures including BCC, a BCC/FCC hybrid, and TPMS gyroid were fabricated from a thermoset resin by SLM, post-cured, and evaluated in compression at room and elevated temperatures. The TPMS gyroid showed superior specific strength and energy absorption. In Figure 1.14, the deformed contour of the mentioned structures is shown by comparing the experimental results and simulation [71, 72]. Although the simulation method will provide insightful information about the structure, reaching a high-accuracy prediction is still a tough task.

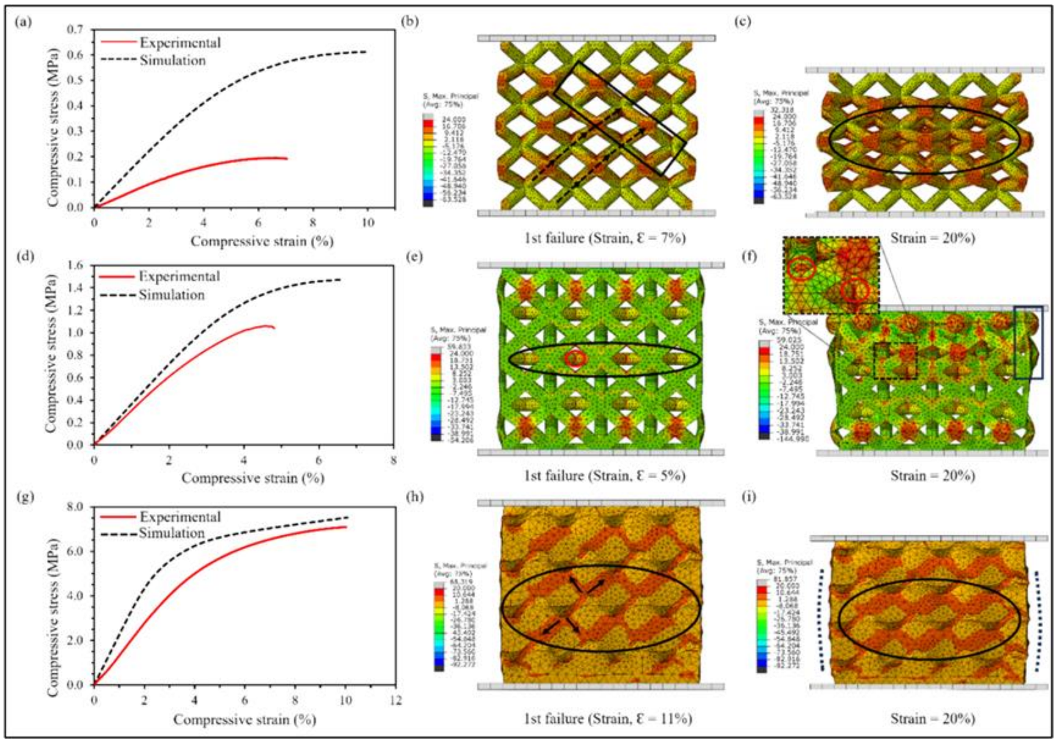

Figure 1.14 Comparison of stress–strain curves between experimental and simulation up to the first failure with max. Principal FEA observations. (a–c) BCC, (d–f) BFCC, and (g–i) TPMS gyroid lattice [72].

1.3 Contribution and Expected Impact

The cellular structures are increasingly expanding in numerous industrial sectors. The mechanical characteristics, designing methods, manufacturing cost-effectiveness, and application performance have yet to be discovered. This thesis aims to increase the insight into the current knowledge of cellular structures, while providing roudmap for future investigations. The main contribution of the present research is to make the design of 3D printed lightweight cellular structures fast and confident, giving a clear vision of cells' differentiation by performing the following studies:

- A unified experimental protocol and dataset for multi-directional elastic moduli of PLA infill cubes, resolving the role of walls and raster orientation over a wide density range. The results of this study are helpful in defining a comprehensive perspective of the variation of the elastic response in three directions by increasing the infill density. The precise quantification of these differences by presenting the trend would be a reference for designers who consider applying infill for the structures and researchers who want more investigation on homogenization methods.

- A micro/meso/macro scale simulation under Periodic Boundary Conditions was used, which achieves about 8% agreement with experimental results. This methodology demonstrates how to select a unit cell at different levels, given geometrical aspects, to reduce the efforts in predicting the mechanical behavior of infills in FFF components.
- Design, manufacturing, testing, and simulation of SLM lattice cylinders at the last step of the study demands courage. Firstly, it demonstrates one of the smart methods to design and model complex cellular structures. Secondly, there was no standard reference test for performaning of internal-pressure, and the test setup was constructed according to the study requirements. Together with three directional compression tests and FEA methods, a perfect reference was provided for lattice cylinders with square-honeycomb cells.

1.4 Thesis structure

This thesis deals with the geometric features of cellular structures and computational methods to evaluate their mechanical performance.

Chapter 1 overviews FDM and SLM technologies and their application benefits. Consequently, introduces the infill structure and honeycomb structures as the target geometry of this study. In addition, summarizes the literature that is connected to the presented research in the thesis.

Chapter 2 focuses on the experimental study on infill structures of PLA material produced by FDM 3D printing technology, considering different densities. It begins with tensile test performance on 100% unidirectional fabrication to be used in simulation. Then, a compression test was conducted on different densities of cubic structures with and without external walls. To have more data for simulation, standard specimens from 100% density were tested under compression load. The main conclusion is the trend of the elastic modulus with variation of infill densities.

Chapter 3 provides computational techniques to predict the stiffness of the infill structures. Firstly, the conventional methods were used to evaluate the real geometry. More importantly, using RVU geometry under periodic boundary conditions was applied to illustrate the smart methodology in breaking down large scale of structures into cells in meso and micro scales. The accuracy and comparison between these two methods are described in this chapter.

Chapter 4 demonstrates an innovative approach for modeling a hybrid lattice structure. The internal pressure test was performed to explore the relation between pressure and radial expansion of cylindrical lattices with two categories of fine and rough cells. The cells' geometries were selected in a way that is printable and indicate clear data on pressure resistance limits. Since the comparison between the two categories of cells is not clear, the compression test was performed to indicate a better sense for differentiating these two. Finally, simulation of the selected section of the structures provides information on this kind of loading and structures.

In the end, Chapter 5 provides the main conclusion of the thesis and future perspective.

Chapter 2

Infill structures: Experimental methods

2.1 Introduction

The main target of this chapter is to get the mechanical properties of the grid infill in three directions. As mentioned in Chapter 1, studies on different infill and different densities were conducted before. However, these studies were focused on one loading direction. The present work compares the mechanical response of different grid infill densities in three orthogonal directions. Additionally, conducting tensile and compression tests on the 100% density specimens has a reference value to compare and input data to use in FEM in Chapter 3.

2.2 Materials

All specimens were fabricated using a 2.85 mm black PLA filament supplied by BASF (Germany). Printing was performed on an Ultimaker S5 at 40 mm/s, with the nozzle set to 215 °C and the build plate to 60 °C, as is typically recommended for this material. Cubic samples were produced with infill ratios of 20%, 40%, 60%, 80%, and 100%, and raster-angle patterns of 0°/90° and −45°/45°. A single extrusion line was used to generate both the internal infill and the external wall. The nominal cube dimensions were 40 × 40 × 40 mm³; after fabrication, careful measurements were taken, and maximum deviations of 0.05–0.15 mm from the nominal size were observed. In Figure 2.1, half-printed specimens are shown to highlight the internal structure.

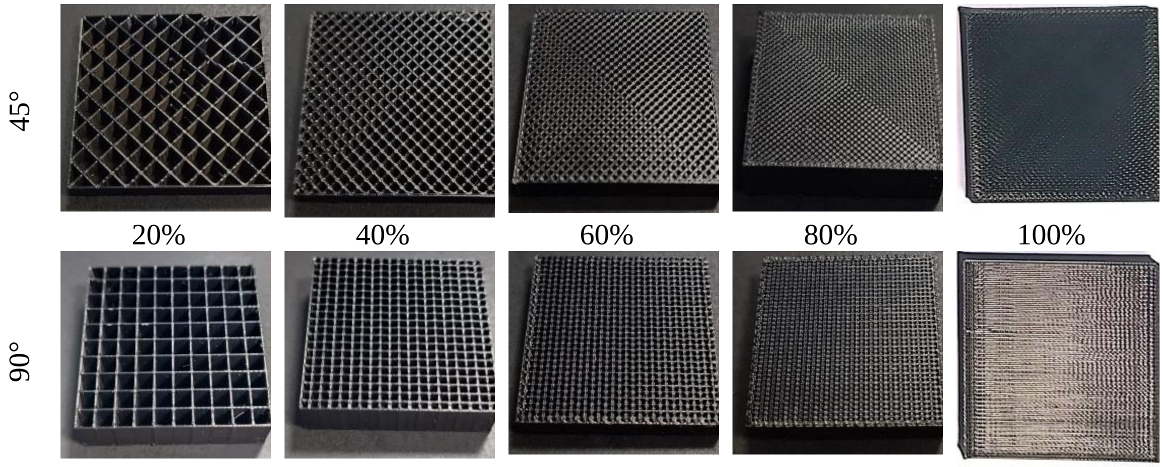

Figure 2.1 Half-printed sections of cubic specimens

From an industrial standpoint, external walls are typically included in FDM parts and are known to contribute substantially to global stiffness. Although internal grid infill behavior was the main focus, the influence of external walls was also assessed. To isolate the infill response, a dedicated set of specimens without walls was tested. Specimen dimensions of 40 mm per side were selected so that, even at low infill densities, a sufficient number of unit cells was ensured for statistically reliable results. To enable the mechanical properties of the PLA filament used in this work to be employed in simulations, standard-dimension specimens were fabricated at 100% deposition. Accordingly, the compression test ASTM D695 [73] was applied to bidirectional deposited specimens, and the tensile test ISO 527 [74] was applied to unidirectional deposited specimens. In total, 88 experiments were conducted, as organized in Table 2.1.

Table 2.1 Tensile and compression categories indicate the number of specimens.

IR	**20%**		**40%**		**60%**		**80%**		**100%**		
RA	**45°**	**90°**	**45°**	**90°**	**45°**	**90°**	**45°**	**90°**	**45°**	**90°**	**Tensile**
Normal cubes	6	6	6	6	6	6	3	3	6	6	-
No walls	3	3	3	3	3	3	-	-	-	-	-
ASTM D695	-	-	-	-	-	-	-	-	-	12	-
ISO 527	-	-	-	-	-	-	-	-	-	-	4

2.3 Tensile test

Unidirectional properties of the PLA along the printed filaments were obtained through tensile testing. Specimen geometry was selected in accordance with ISO 527, and four specimens were fabricated and tested. Tests were carried out on an MTS 810 frame fitted with a 25 kN load cell. Longitudinal strain was measured by an extensometer, while digital image correlation (DIC) was employed to capture both longitudinal and transverse strains for the computation of Poisson’s ratio. During each test, images of one face of the specimen—prepared with a suitable speckle pattern—were acquired every 3 s using a 5 MP Dinolite digital camera (Almere, The Netherlands). Image correlation was performed with the DICe (Digital Image Correlation Engine) software to extract longitudinal and transverse strain fields. In Figure 2.2, the test setup and the details of the specimens are shown.

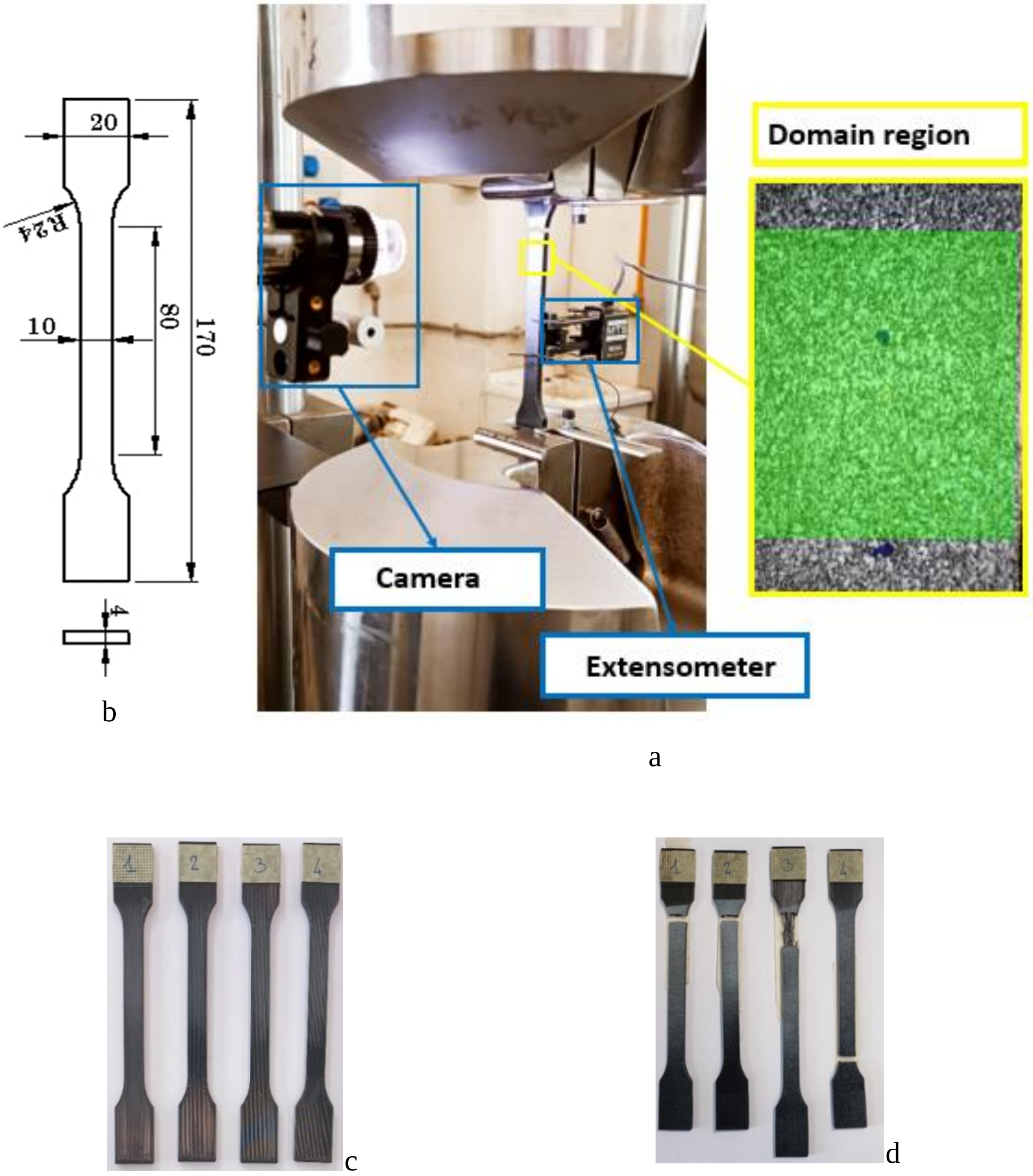

Figure 2.2 Tensile test setup with domain region (a), dimension of specimens (b), and tensile specimens before (c) and after (d) the test.

The Young’s modulus for each test was determined by linear regression over the initial linear segment of the stress–strain response. Poisson’s ratio was obtained as the slope of the linear regression of transverse strain versus longitudinal strain. A representative stress–strain curve, with strain measured by both extensometer (EX) and DIC, is provided in Figure 2.3; close agreement between the two measurements can be observed, thereby supporting the validity of the DIC-based results. The average values and standard deviations from the four tensile tests are reported in Table 2.2.

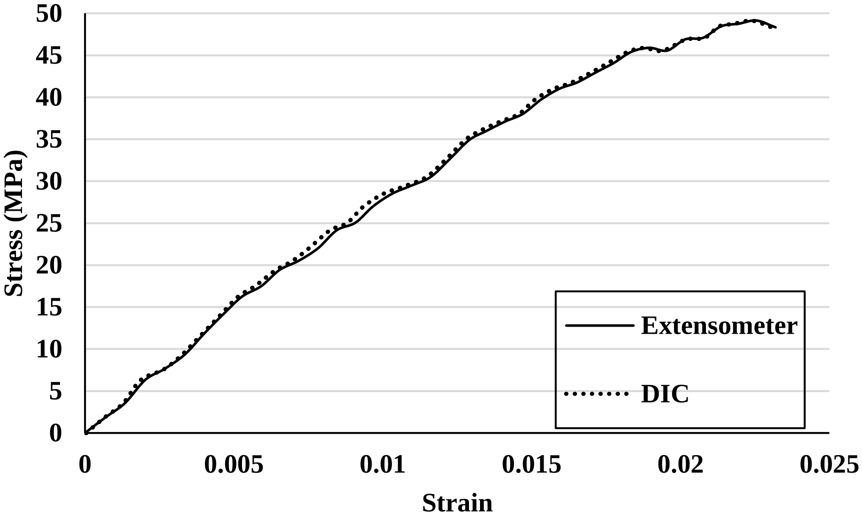

Figure 2.3 Engineering stress _ strain curve results from both extensometer and DIC measurement.

Table 2.2 Mechanical properties of the 3D printed PLA from the tensile test

	Young’s modulus (E) [GPa]	**Poisson’s ratio (v)**	**Yield stress (σ_y)** [MPa]
AVG.	2.84	0.37	43.2
STD. DEV.	0.05	0.01	2.6

2.4 Compression tests

Compression tests on the cubes were conducted on an MTS 810 testing machine equipped with a 250 kN load cell. Loading was applied through two rigid plates secured in the machine grips. Each test was displacement-controlled to 20 mm (≈50% global strain) at a crosshead speed of 0.01 mm/s. To obtain accurate deformation measurements and limit the influence of frame compliance, a Digital Image Correlation (DIC) system was employed. Images were acquired every 3 s using a Dantec Dynamics Q400 3D DIC system with two 2 MP cameras and were subsequently processed. For displacement analysis, the loading plates were tracked, and the Dantec system recorded the displacement with a mesh size of 11 pixels (see Figure 2.4).

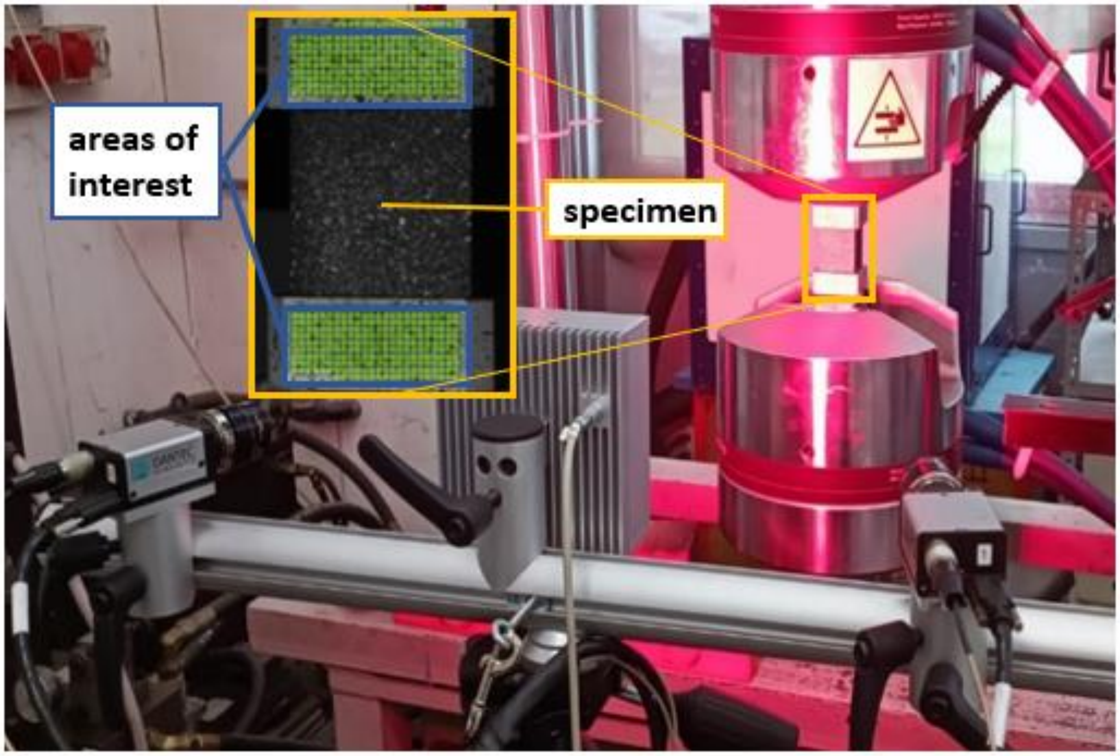

Figure 2.4 Compression test setup indicating the area of interest for DIC measurement.

2.4.1 Cubes with walls

In FDM parts, external walls (skins) are included at all infill densities and are recognized to contribute substantially to stiffness; their bonding to the infill is considered critical. For the test specimens, a single wall layer was adopted in every case, irrespective of the design plan. To distinguish loading configurations, directions were defined with respect to the manufacturing process: the two in-plane directions parallel to the build plate were assigned as axes 1 and 2, while the through-thickness (build-up) direction normal to the plate was assigned as axis 3. After fabrication, compression tests were categorized as C_i (i = 1, 2, 3), where the subscript indicates the loading direction (see Figure 2.5).

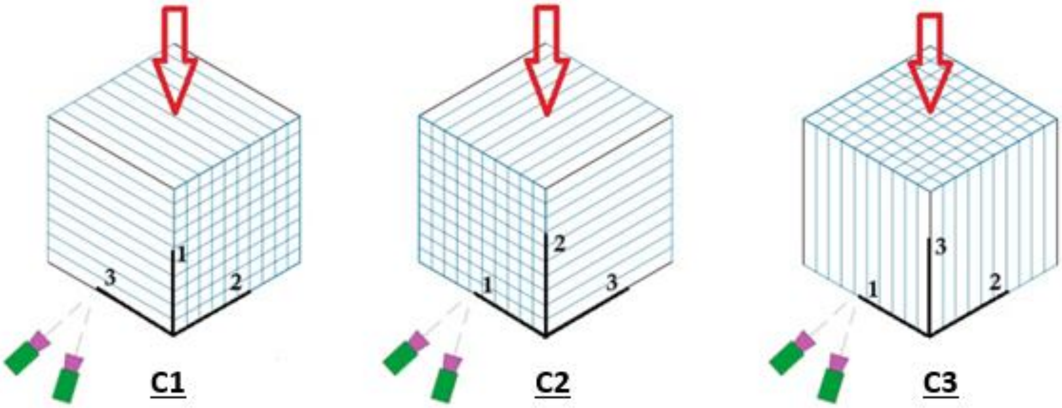

Figure 2.5 Three loading directions according to printing directions.

2.4.2 Infill without walls

In addition to the previous cubes, modified specimens (removed walls) were also tested. Firstly, for selected sets of cubes (20%, 40%, and 60% with both types of raster angle), in each set of three specimens, the walls were machined out to leave only the infill structure, enabling the compression tests to be performed on the infill alone. The test execution followed exactly the procedure explained for cubes with walls, with the only difference being that for the displacement evaluation through DIC, only the plates were considered as the area of interest (Figure 2.6). It was not possible to record the deformation of specimens because it required to have a united face in front of the cameras.

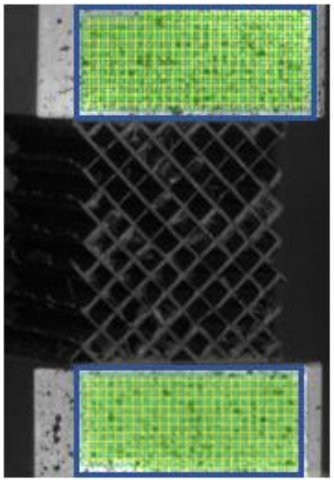

Figure 2.6 Specimens without walls under compression test with the indicated domain region.

2.4.3 Standard-sized specimens

To characterize the material according to an international standard, 12 specimens (three cubes, each cube with four specimens) were machined out from a 100% IR cube, with a size 12.7 x 12.7 x 40 mm^3, to have a specimen compliant with ASTM D 695. Compression tests on machined specimens were performed with the same procedure for cubes, with the only difference being that for the displacement evaluation through DIC, only the face of the specimen was considered as the area of interest (see Figure 2.7).

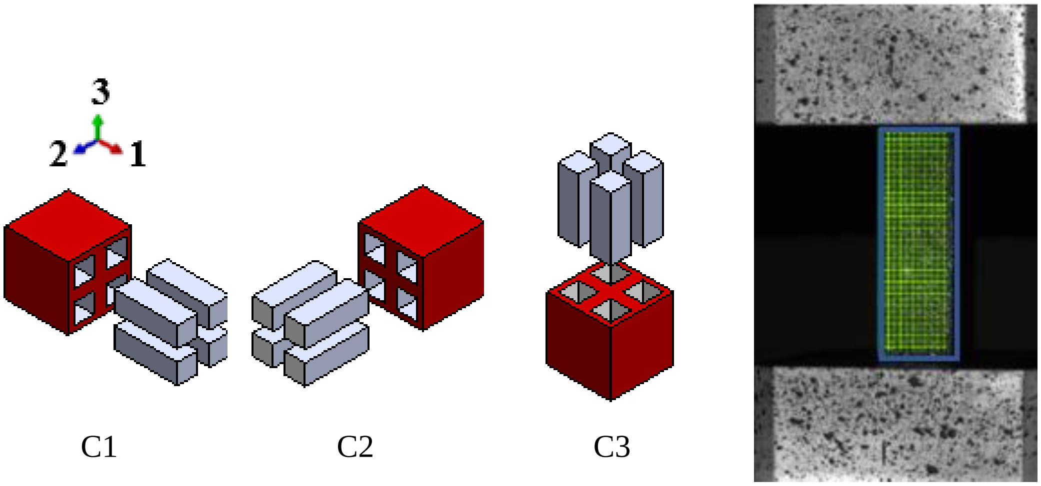

Figure 2.7 Extracted standards specimens by removing red regions (left), specimens according to ASTM D695 under compression test with indicated domain region (right).

2.4.4 Compression test data processing

For the complete cubes, the linear elastic mechanical response of each specimen was characterized by the equivalent of Young's modulus (Eeq) and Transverse strain (εx). The equivalent stress (σeq) was determined by dividing the recorded force (F) by the initial cross-sectional area (Ain) for each specimen (Equation (2.1)). For cubes, the longitudinal strain (εy) was obtained by dividing the displacement of the loading plate by the initial plate distance (Equation (2.2)). Young's modulus (Eeq) was derived from the stress-strain curve as the slope of the curve in the initial linear elastic region. For the cubes without the wall, only the vertical strain was investigated, and the nominal area was assumed as the initial cross-sectional area.

For ASTM D695 specimens, the longitudinal and transversal strains were derived from the recorded deformation of the specimen (Equations (2.3) and (2.4)). Poisson's ratio (νeq) was calculated as the ratio of transverse strain to longitudinal strain (Equation (2.5)). To clarify the deformation evaluation, the tracked points selected for displacement analysis during testing are illustrated in Figure 2.8.

$$\sigma_{eq} = \frac{F}{A_{in}} \tag{2.1}$$

$$\varepsilon_y = \frac{L_1 - L_2}{L_1} \tag{2.2}$$

$$\varepsilon_{Ys} = \frac{\Delta Y_2 - \Delta Y_1}{\Delta Y_1} \tag{2.3}$$

$$\varepsilon_{Xs} = \frac{\Delta X_2 - \Delta X_1}{\Delta X_1} \tag{2.4}$$

$$\nu_{eq} = \frac{\varepsilon_{Xs}}{\varepsilon_{Ys}} \tag{2.5}$$

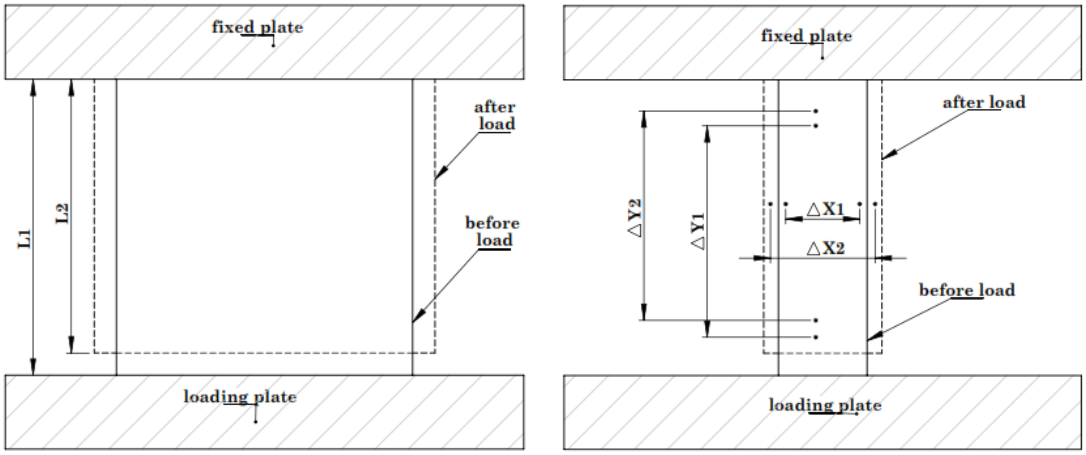

Figure 2.8 Schematic representation of deformation tracking for cubes (left) and ASTM specimens (right).

2.5 Results and discussion

2.5.1 Elastic results

This section presents a comparative analysis of experimental cases across different loading directions. Initially, a detailed evaluation is provided, followed by a comparison of elastic modulus trends across various densities (see Table 2.3). For 80% density, one repetition was tested, and there is no deviation. The visual comparison is shown in Figure 2.9; the elastic modulus of the cubes (Ei_C) varies significantly with infill ratio (IR) and build direction. For IR values between 20% and 80%, E3 is greater than E1 and E2 (in-plane directions). However, at 100% infill, the trend reverses, with E1 and E2 exceeding E3 due to the deposition of the material. To illustrate the point, the layer-wise fabrication should be considered. For infills, E1 and E2, since the parallel lines have a distance from each other, they show poor stiffness, while in E3, they have a sturdy connection. However, for 100% density, all lines are interconnected. In this type of fabrication, the number of lines aligned to the load direction governs the extent of stiffness. The more lines exist in the load direction, the stiffer the structure will be. If the lines have angles to the load directions, are they are perpendicular to it, the level of stiffness is reduced.

Table 2.3 Experimental results of the elastic modulus of all tested cubic specimens.

	(GPa)	**20**	**STD**	**40**	**STD**	**60**	**STD**	**80**	**100**	**STD**
45°	**E1**	0.09	0.001	0.21	0.004	0.47	0.01	1.11	2.55	0.021
	E2	0.11	0.005	0.21	0.018	0.47	0.016	1.14	2.52	0.234
	E3	0.5	0.011	0.99	0.023	1.47	0.034	2.03	2.23	0.1
90°	**E1**	0.33	0.032	0.71	0.006	1	0.004	1.64	2.55	0.288
	E2	0.32	0.023	0.59	0.027	0.95	0.056	1.46	2.46	0.245
	E3	0.48	0.016	0.95	0.013	1.43	0.008	1.88	2.23	0.014

Table 2.4 presents relative stiffness variations across different raster angles and infill densities:

- For a 45° raster angle, in-plane stiffness increases from 18% (at low IR) to 56% (at high IR) relative to E3.
- For a 90° raster angle, in-plane stiffness ranges from 62% to 87% relative to E3.
- At 100% infill, in-plane stiffness exceeds build-up stiffness by 10% to 14%.

Table 2.4 Relative differences in elastic modulus across the three principal loading directions of cubes.

		20%	**40%**	**60%**	**80%**	**100%**
45°	**E_1 / E_3 (%)**	18	21	32	55	114
	E_2 / E_3 (%)	22	21	32	56	113
90°	**E_1 / E_3 (%)**	69	75	70	87	114
	E_2 / E_3 (%)	67	62	66	78	110

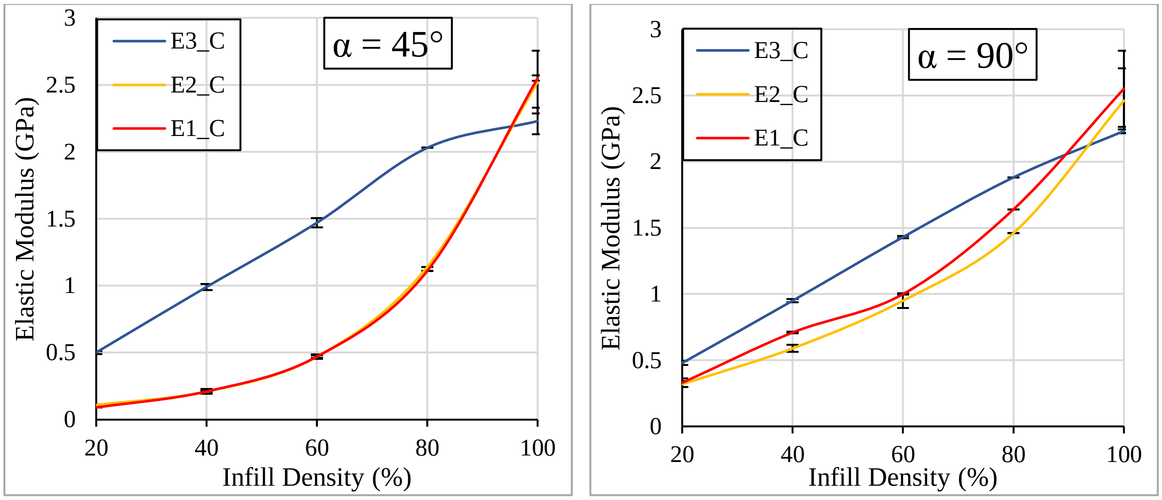

Figure 2.9 Trends of elastic modulus across different infill densities for (left) 45° and (right) 90° raster angle.

In FDM-manufactured products with embedded infill options, external walls significantly influence overall stiffness. To quantify their effect, specimens with and without walls (No Walls, NW) were tested at 20%, 40%, and 60% IR. Figure 2.10 compares the stiffness of wall-free vs. normal cubes, with exact elastic modulus values (GPa) indicated in the contribution of the wall effect for different ratios. For E3, the walls have minimal influence due to the consistent deposition alignment between the walls and infill. In contrast, for E1 and E2, stiffness is significantly lower, especially at lower IR values and with 45° raster orientations.

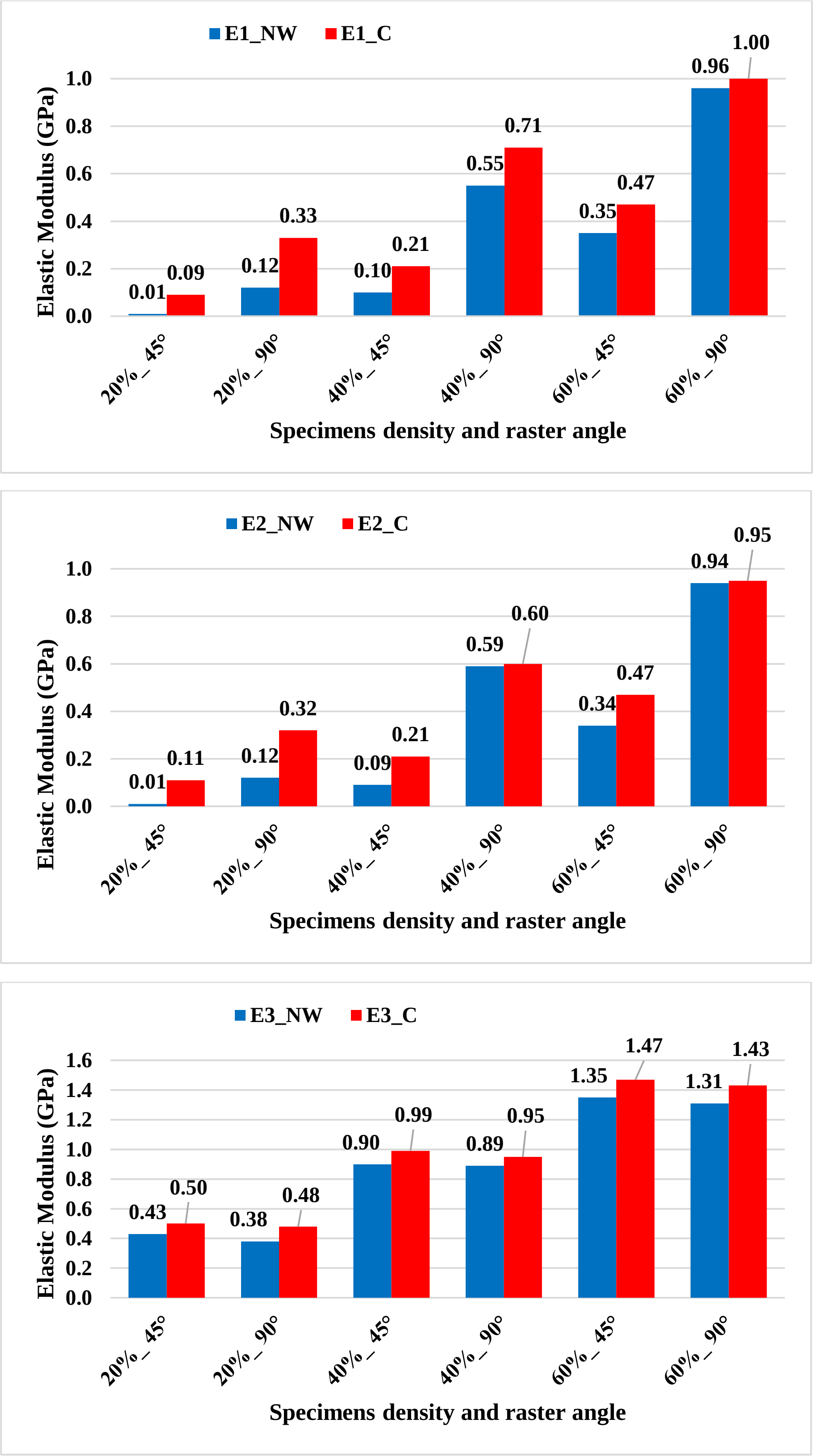

Figure 2.10 Comparison of elastic modulus between specimens with and without external walls, showing the influence of boundary layers on stiffness.

2.5.2 Failure results

In the previous sections, the focus was on the elastic behavior of infills. Now, the directional comparative approach of failure modes is evaluated. The force–displacement curves are explored to be compared for the under-studied specimens and load directions. Three loading directions on cubes are indicated according to Figure 2.5. As mentioned in section 2.4.2, for 20%, 40% and 60% densities, the removed wall specimens were tested. The elastic comparison is discussed in Figure 2.10. Since the structures lost coherence without walls, in many tests, after the elastic load, the specimens broke or slid (shifted away) from the load plates, and the most valid data for comparison is for 20% (see Figure 2.11). In Figure 2.12, the force–displacements of cubes with infill are shown. The mechanical response for fully fabricated cubes or 100% specimens is different from the lower densities, thus it is shown separately in Figure 2.13. In Table 2.5, two failure parameters, mean force (MF) and peak force (PF), for the tested specimens are indicated to compare. In addition, in terms of illustration, in Figure 2.14, for 20% the stepwise increments of specimens are shown. In general, the following results are discussed:

- By removing the walls, roughly 4 % to 5 % of the mass is removed. However, the stiffness and strength reduce more than the mass reduction. It means that the interconnection between walls and infills supports the entire structure. Comparing 20% infill with and without walls, it can be concluded that, as indicated in Figure 2.10, the effect of the wall in 20% is higher than the infill itself. In particular, for L1 and L2, the force for failure is beyond comparison, 4 to 18 times lower than the cubes with walls. However, for L3, by removing the wall, the MF reduction is (75% for 45°and 95% for 90°), and the PK reduction is (37% for 45°and 47% for 90°).
- 20%: The MF for L3 is too much higher than L1 and L2 (more than 6 times) and the PF for L3 is even higher in comparison to L1 and L2 (3 to 4 times for 90º and 8 times for 45º). In addition, the PF for L3 is 70% higher than the MF, while in L1 and L2, PF and MF are close. Although for L3, 45° and 90° are almost the same, in L1 and L2, 90° has several regional peaks (for each layer

when failure is happening), whereas in 45° the curves are smooth after the first peak.

- 40%: The difference between failure parameters reduces in comparison to 20% and L3 has a longer PF. The MF for L3 is (3 times for 90º and 5 times for 45º) bigger than L1 and L2. This difference is for PF (2 times for 90º and 5 times for 45º). While L3 for both 45° and 90° is almost the same, the oscillation at 90° for L1 and L2is very high.
- 60%: L3 changes the same as 40%. On the other hand, at 90°, L1 and L2 have less oscillation in comparison and are closer to L3. Moreover, L1 and L2 are less close than this pair for lower densities. Quantitatively, MF for L3 is (1.2 times for 90º and 2.5/3.5 times for 45º).
- 80%: The structural behavior is altering the trends. Although the PF for L3 is still larger than L1 and L2 when the failure continues, the MF is rising, but L3 diminishes.
- 100%: In 45°, there are slight differences between loads in three directions. At 90°, L1 and L2 have higher PF and MF than L3.

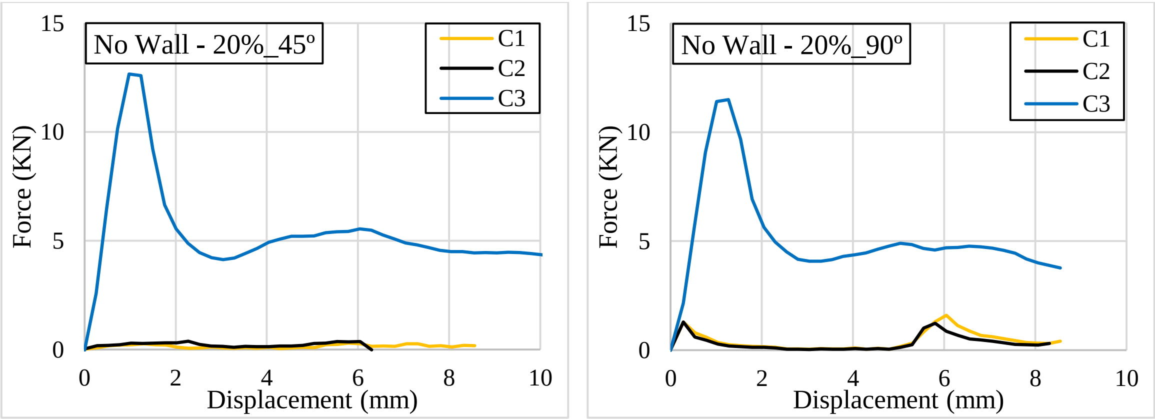

Figure 2.11 Load-displacement curve of cubes with 20% infill (removed wall).

Table 2.5 The mean and peak forces for the compression test.

		45º		90º	
(KN)		**Mean force**	**Peak force**	**Mean force**	**Peak force**
No Wall _ 20%	**L1**	0.1	0.3	0.4	1.3
	L2	0.2	0.4	0.4	1.2
	L3	6.0	12.7	5.3	11.5
20%	**L1**	1.8	2.1	1.6	5.1
	L2	1.7	2.3	1.6	4.2
	L3	10.4	17.5	10.3	17.0
40%	**L1**	6.1	6.7	8.6	22.0
	L2	6.6	8.0	11.0	19.2
	L3	29.9	38.4	26.8	37.8
60%	**L1**	17.9	16.6	34.7	43.4
	L2	13.0	17.0	29.8	36.1
	L3	43.4	57.7	38.9	56.5
80%	**L1**	49.7	36.4	58.6	62.7
	L2	56.4	38.3	65.6	62.9
	L3	63.0	80.0	54.4	77.7
100%	**L1**	78.6	79.1	85.4	98.3
	L2	82.2	80.2	86.5	101.1
	L3	81.6	82.3	80.1	81.2

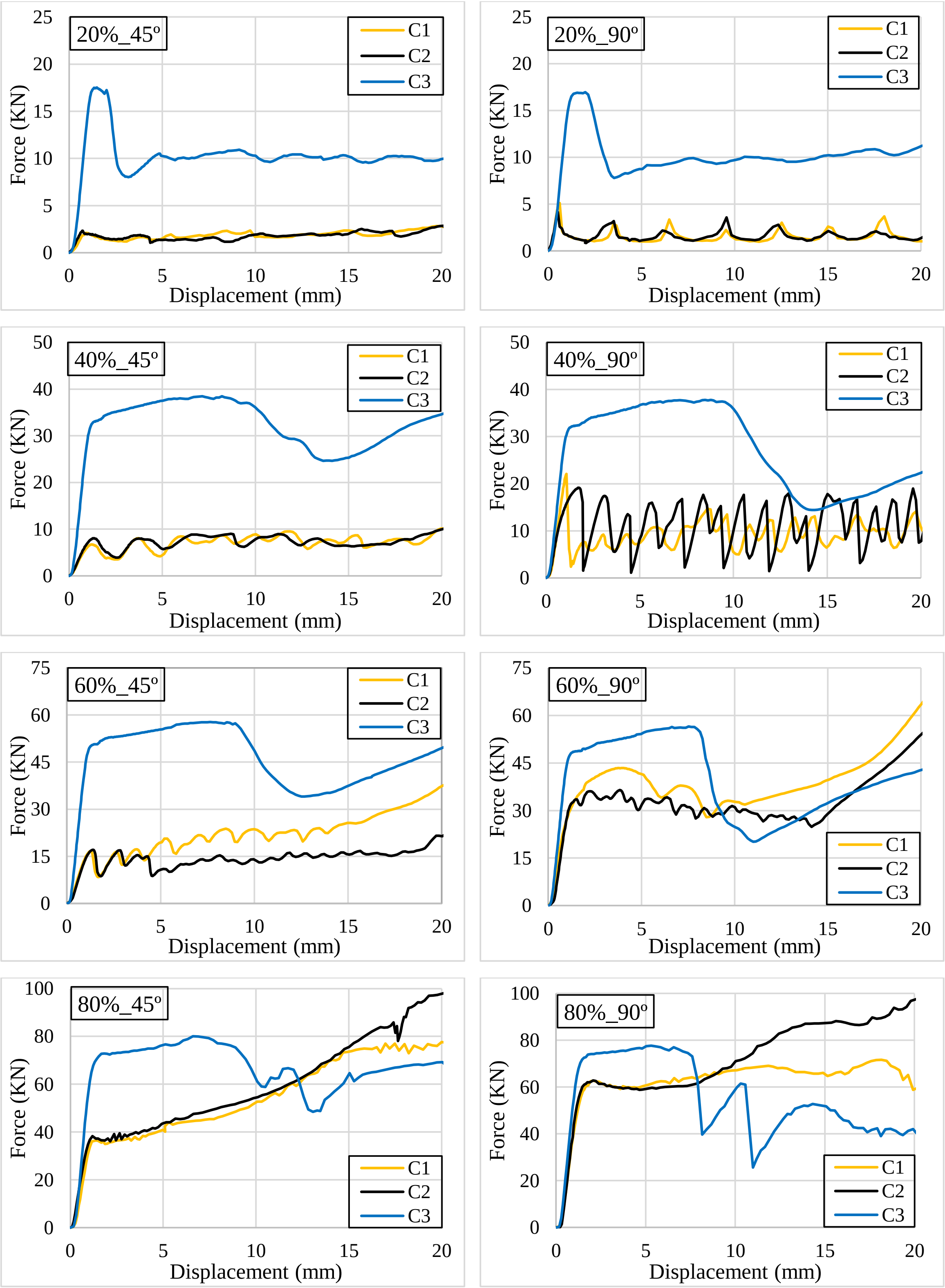

Figure 2.12 Load-displacement curve until 50% compression of cubes with infill.

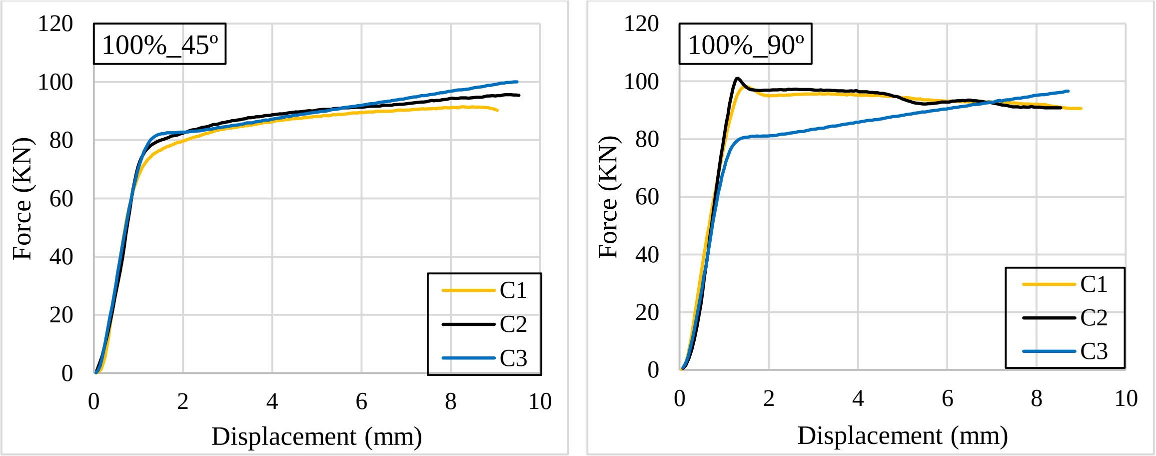

Figure 2.13 Load-displacement curve of cubes with 100% filament.

The visual deformation of the specimens helps to understand the force-displacement curves. For the cubes with walls, the figures for all densities are not that different. For the removed wall specimens, the most clear deformation is for 20%. In summary, the 20% specimens are enough to show the internal failures. Moreover, C1 and C2 are the same; therefore, only C1 is presented as the in-plane direction. At 45°, C1, the failure will begin in the diagonal direction. As a result, the applied force increases at a smooth pace, and since the lines have a 45° angle with the load direction, the value of force is less than 90°. On the other hand, at 90°, the failure happens in a row of cells perpendicular to the loading direction. Hence, there are oscillations along force-displacement curves. It means that the lines bear until a certain amount of load, and it raises the force. When the lines of one layer break, the force immediately reduces. This happens for each layer until the full compression. In C3, the resistance is higher, but after the deformation, like barreling. This may start from the top, bottom, or middle row and graduate to the adjacent row till complete compression.

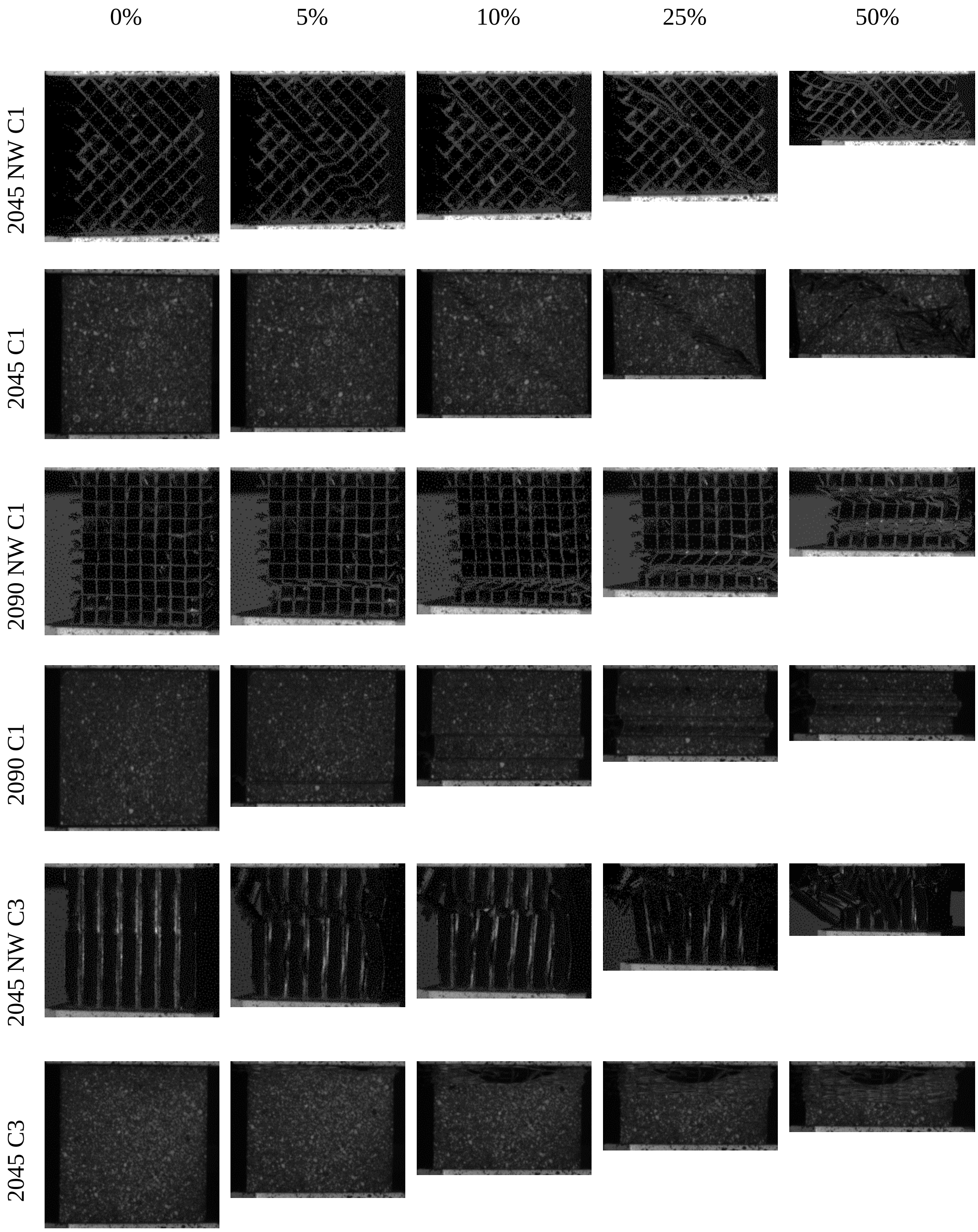

Figure 2.14 Failure modes of the specimens in gradual increments.

2.6 Conclusions

The key findings of the conducted experimental study are summarized as follows:

1. The relationship between elastic moduli (E3, E2, and E1) varies with infill ratio and raster angles. The results demonstrate that stiffness trends are significantly affected by the interaction between infill ratio and orientation.
2. In grid infills, the build-up direction stiffness (E3) remains relatively independent of raster orientation. However, in in-plane directions, stiffness (E1 and E2), a 45° raster angle results in lower stiffness, whereas a 90° raster angle increases stiffness. In real-world applications with complex loading conditions, the effective stiffness will typically fall between these two extremes.
3. The failure evaluation was multi-directional. Force-displacement curves showed that the difference in lower densities is greater than in higher densities.

Chapter 3

Infill structures: Numerical methods

3.1 Introduction

Prior research has emphasized the importance of predictive modeling, but discrepancies between experimental and computational results persist. Homogenization and RVE-based methods have greatly advanced the prediction and optimization of 3D-printed cellular structures. However, current models struggle with process-induced anisotropy, microstructural variability, and defect sensitivity. Challenges remain in accurately capturing localized filament defects, voids, and loading conditions on mechanical properties. At first, the nominal model (dimensions defined for the slicer to generate the model) and real geometry (refined model according to the microscopic images taken from the 3D printed specimens) are modeled, and by defining isotropic properties, it is shown how close the simulation and experimental results can get. In the following, it has been made to bridge the gap between micro-scale void analysis and mesoscale structural behavior, ensuring a more robust understanding of 3D-printed infill structures. This way, the extent of anisotropy of the infill structure is illustrated.

3.2 Real geometry simulation

Finite element simulations of the compression tests were performed in ABAQUS 2022 (Dassault Systèmes). Three modeling approaches were evaluated:

1. A shell model (SHL) (Figure 3.1b–c), in which internal and external walls were represented by shell elements.
2. A solid model (SLD) (Figure 3.1d–e) with a nominal wall thickness of 0.4 mm (nominal geometry applied).
3. A non-uniform section model (NUS) (Figure 3.1 f–g), in which wall and strut dimensions were obtained from microscope images with 10 µm accuracy. The microscopic images are shown later in Figure 3.7.

To reduce computational cost, 1/8 of each specimen was modeled by enforcing symmetry boundary conditions on three orthogonal planes (Figure 3.1a). C3D8R elements (8-node linear brick, reduced integration) were used for solids, and S4R elements (4-node shell, reduced integration) were used for shells. The resulting model size was 20 × 20 × 20 mm³, with inner and outer wall thicknesses of 0.4 mm. Under the symmetry constraint, a prescribed displacement of 0.2 mm (≈1% of the model length) was applied to the external walls along X or Z (X and Y being equivalent by symmetry in the X–Y plane).

Linear, isotropic, homogeneous elastic behavior was assumed, with material properties taken from the tensile tests presented in section 2.3. Mesh-size effects were evaluated to ensure accuracy. For shell models, convergence was achieved with an element size of 2 mm. For solid models, a mesh size of at least 0.2 mm—i.e., two elements across the 0.4 mm wall thickness—was recommended to obtain stable estimates of the cube's Young's modulus.

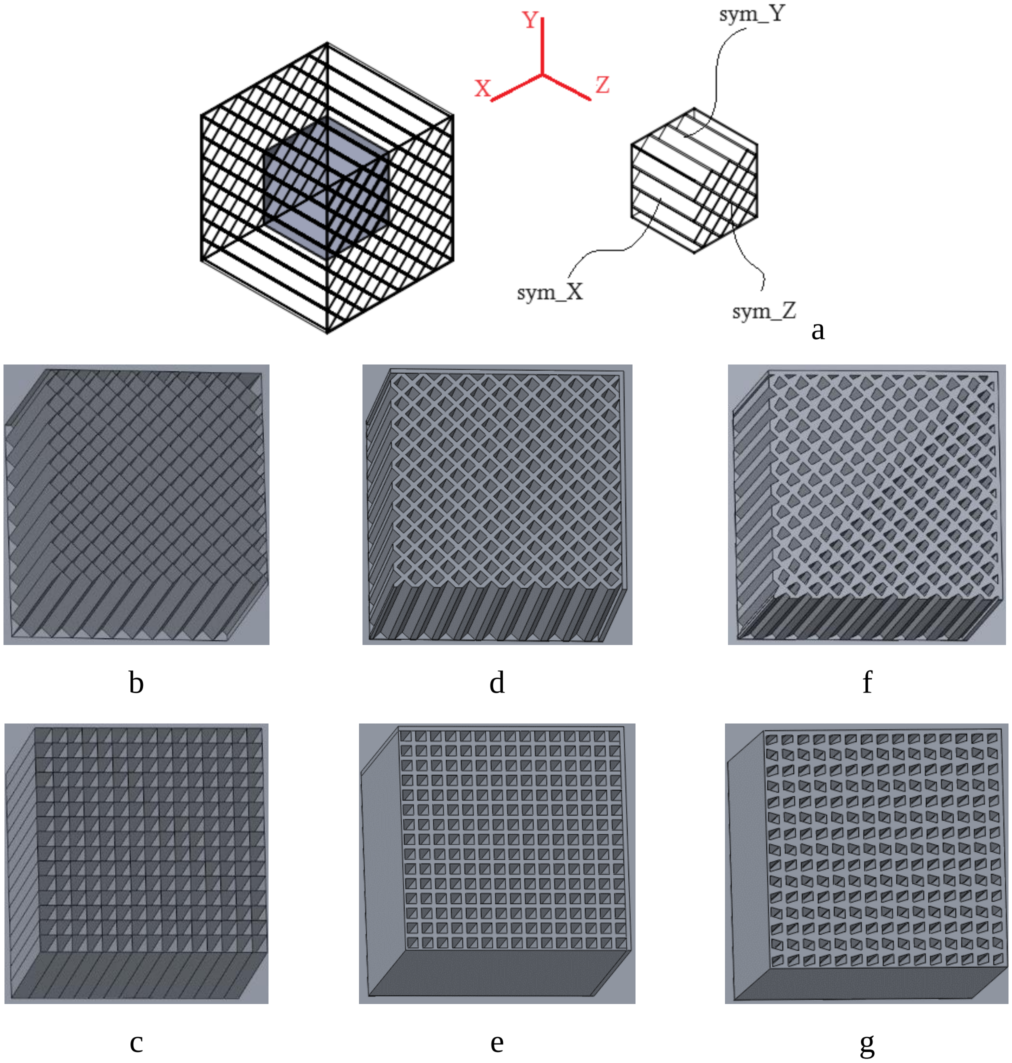

Figure 3.1 Boundary conditions for showing 1/8 model (a) with shell (b, c), solid nominal dimensions (d, e), and real geometry (f, g) models.

3.2.1 Results of real geometry simulation

The conventional and routine analysis was made to see how close it is to the experimental results. First, the differences between solid and shell discretization were examined; then, the effect of using a geometry closer to the printed morphology was assessed. In the SLD and SHL models, E1 and E2 were obtained as equal because a uniform wall thickness was assigned to all cell walls. Differences were observed between experiments and simulations, and among the three modeling approaches. Shell (2D) models yielded larger stiffness values than solid (3D) models. Shell elements work best when the walls are thin. A common way to check if a shell model is a perfect choice for FEM is the thickness-to-length ratio, t/L. For thin-walled parts, typical values are about 1/60–1/30 for tubes and 1/20–1/10 for box shapes [75, 76]. In our case, the ratios are about 1/10, 1/5, and 1/3 for 20%, 40%, and 60% infill, so the walls are much thicker than the usual range. This likely explains why the solid model and the shell model do not give the same results. At the end, Trends in each loading direction were compared with the corresponding experiments in Figure 3.2.

For E3, experimental values were consistently lower than the numerical predictions, with the smallest gap at 60% infill. The non-uniform section model becomes more noticeable at higher density, leading to closer prediction. For E1 and E2, simulated values were close to the experimental results and were slightly lower at 60% infill, likely for E2, the same reason noted for E3. To compare E1 and E2 across raster angles, the α = 0°/90° and α = 45°/-45° cases were observed separately. In grid infills, in each layer, fabricated lines crossed each other. This way, some lines are firstly deposited by the nozzle (primary), and the secondary lines pass the section that is already occupied by the primary lines. As a result, the filament shape is not uniform, and the line thickness varies through each cell. In α = 0°/90°, the secondary lines along direction 1 (defining E1), and the primary lines define E2. As reported previously, the average filament thickness along direction 1 is larger. Accordingly, E2, from simulations (which assume non-uniform thickness), follows the experimental trend closely, whereas E1 exhibits a higher trend (Figure 3.2d). In α = 45°/-45°, loading is applied to the printed lines, which complicates the response. At low infill densities, E1 and E2 behave similarly (Figure 3.2c), while at higher densities, thicker lines induce anisotropy and separate the trends. The lower of the two experimental trends remains close to the simulation based on nominal geometry.

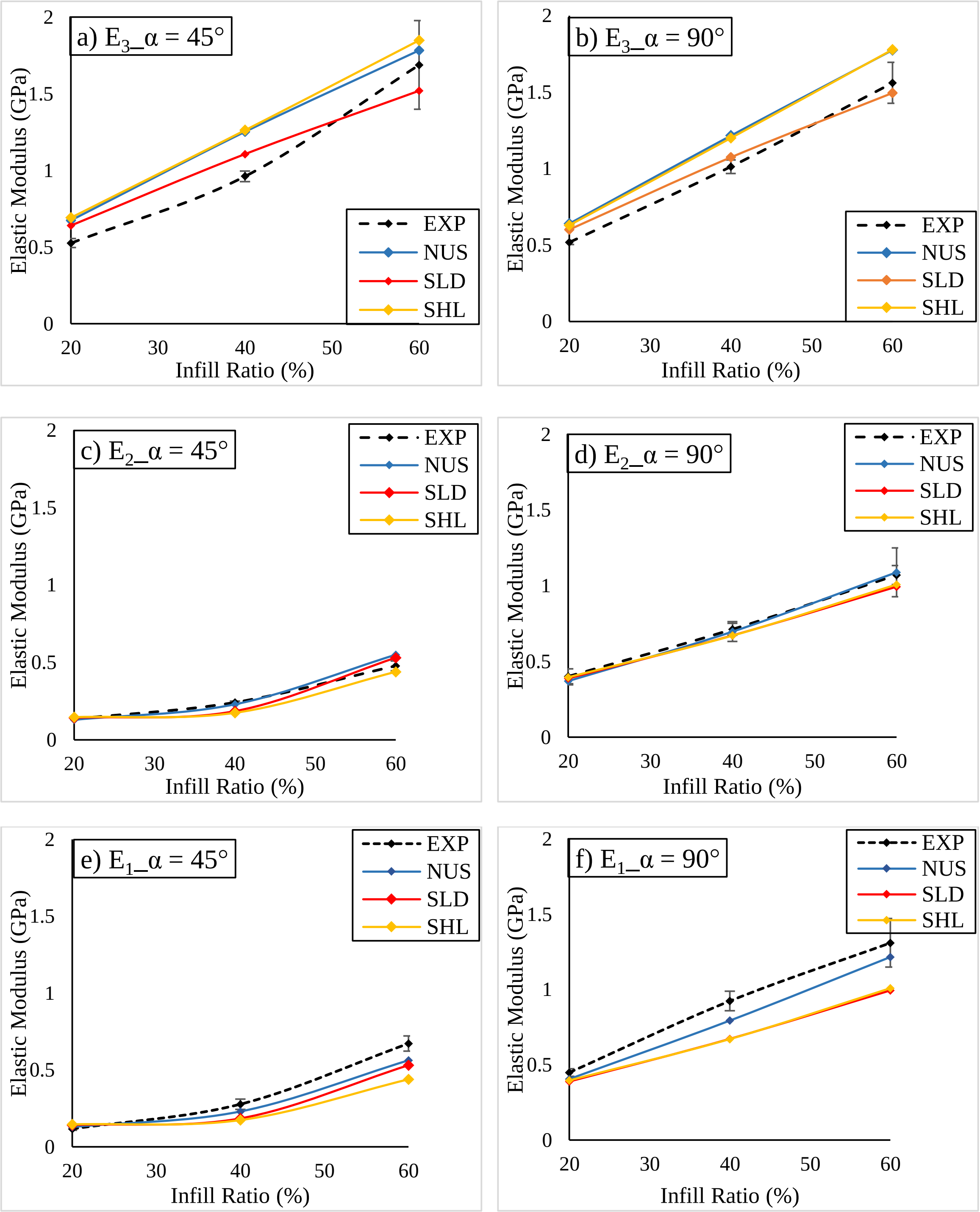

Figure 3.2 Trend of E in different densities for 45° and 90° deposition (experiment and FEM).

Through the three modeling strategies, the NUS approach provided the closest agreement with experiments, especially for E1 and E2. An average volume excess of about 3% over nominal was identified and incorporated into the non-uniform model. Mean absolute differences with experiments were approximately 19% for SHL, 15% for SLD, and 13% for NUS. In this method, although the thickness variation was taken into account to find a better prediction, the innate anisotropy that is the result of layer-wise fabrication is not considered. In section 3.3, a more detailed model is investigated to reveal the microfabrication more precisely.

In Figure 3.3, the stress distribution for the solid model with nominal dimensions at a representative density is shown. Distributions for the other models were similar. Although stress magnitude was not the main objective, these plots help clarify how printed layers interact with the loading directions. When the load and the deposited layers are aligned, higher local stresses are observed along those layers, and the apparent stiffness increases.

In Figure 3.3 (a, b), most layers are aligned with the load; therefore, E3 shows high stress, and the full cross-section contributes to stiffness. For E1 and E2 at 0°/90° shown in Figure 3.3 (c, e), approximately half of the layers carry load, so the effective modulus is typically about one-half of E3. In Figure 3.3 (d, f), for E1 and E2 at minus -45°/45°, the infill resists the load less in the loading direction, and most of the load is transferred to the external walls, which leads to lower stiffness and the smallest elastic response. Overall, stiffness was found to increase with the number of layers oriented along the loading direction.

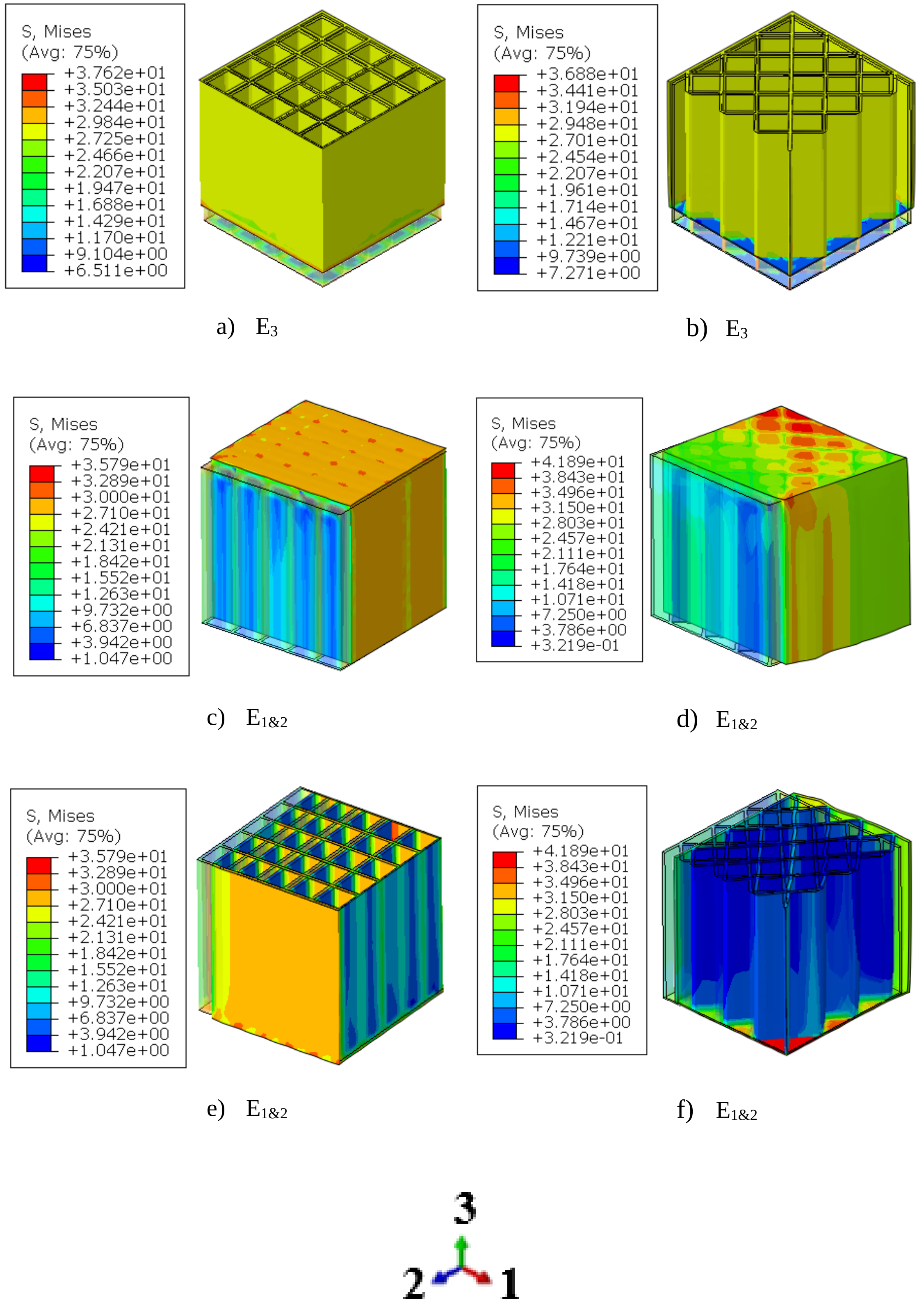

a) E_3

b) E_3

c) $E_{1\&2}$

d) $E_{1\&2}$

e) $E_{1\&2}$

f) $E_{1\&2}$

Figure 3.3 Stress distribution for solid model (uniform walls) in 20% and three load directions.

3.3 Multi-scale modeling

In this study, the problem has been broken down into several steps, which helps to have a vivid perspective on the microstructure of FDM products. In addition, the analysis becomes more controlled and manageable conveniently. As illustrated in Figure 3.4, experimental tests and numerical methods have an interconnected relationship. Simulation results are validated with corresponding experimental tests. Although the target is to predict the homogenized properties of cubes, the tensile tests were used to have a reference material property for simulation, considering a parallel filament deposition or unidirectional fabrication. These properties were used to simulate the UC_micro_100%, which is justified by the results of the ASTM D695 compression test. To have the mechanical properties of infills in different ratios, UC_meso was modeled using the properties of UC_micro_100% as input. In the end, a macro-scale simulation to model the cubic specimens with infill and solid walls (in the following simply "cubes") is defined. By comparison of the equivalent elastic properties from simulation to experimental results, the evaluation loop is closed.

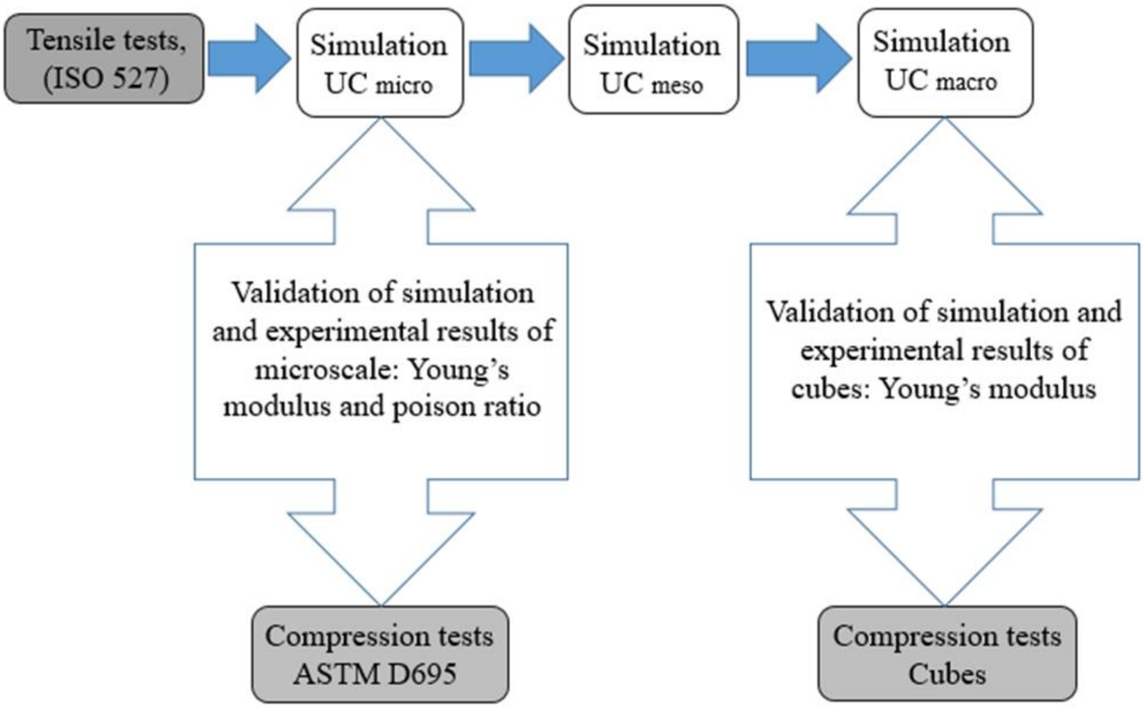

Figure 3.4 Overview of the multi-scale simulation methodology, illustrating experimental validation and the hierarchical modeling approach from micro- to macro-scale.

This section aims to explain why multi-scale methods are suitable for predicting the mechanical behavior of infill structures and how to perform them. The objective is to obtain homogenized mechanical properties that accurately represent infill structures through varying densities, allowing their behavior to be approximated as a bulk material. Achieving this requires a detailed analysis of the micro-scale geometry of the printed structures. Microscopic images revealed various geometric phenomena affecting deposition quality. Usually, researchers consider a symmetric oval-shaped filament as shown in Figure 3.5. However, this study for modeling replicates what was observed from the microscopic images without any simplification to reflect the anisotropic aspect of the problem as much as possible.

One positive advantage of this study is to avoid the simplification of geometric observation. All the curvature and asymmetric dimensions of the tensile sample (TS) and compression sample (100% infill) are considered in the modeling. The critical factor is the non-uniformity of deposited layers due to the filament shape, which causes voids as shown in Figure 3.6 and line intersections in each layer, which results in variability in cell geometries, Figure 3.7. The non-uniformity in line intersection is because of crossing lines at one level of height, which creates mass reduction or mass accumulation. The shape and scale of voids and unit cells (UC) are different in three axes of the global system, leading to direction-dependent mechanical behavior. The modeling approach, therefore, involved separating the effect of voids and layer deposition path into different computational models. The first scale focused on void modeling (UCmicro), the second on the effect of the layer deposition path (UCmeso), and the third on full-scale bulk (homogenized) modeling of the cubes with infill structures. The average dimensions of voids and cells were taken for modeling, as described in the following.

In FDM technology, the first step is to define the raster path with a slicer software. When the infill is included, depending on the infill type and the shape of each layer, the slicer optimizes the path to move the raster in the fastest possible way. There is a tricky difference between 45º and 90º raster angles. If the variation of lines’ thickness is the focus, both cases have the same dimensions. However, the internal fabrication of each cell is different for each raster angle, which is evident at higher infill ratios. This path determines the thickness variation and the arrangement of the cells next to each other. For 45° raster angles, UCs are classified as equal-directed lines (EL); instead, counter-directed lines (CL) are fabricated for 90° raster angles (see Figure 3.8).

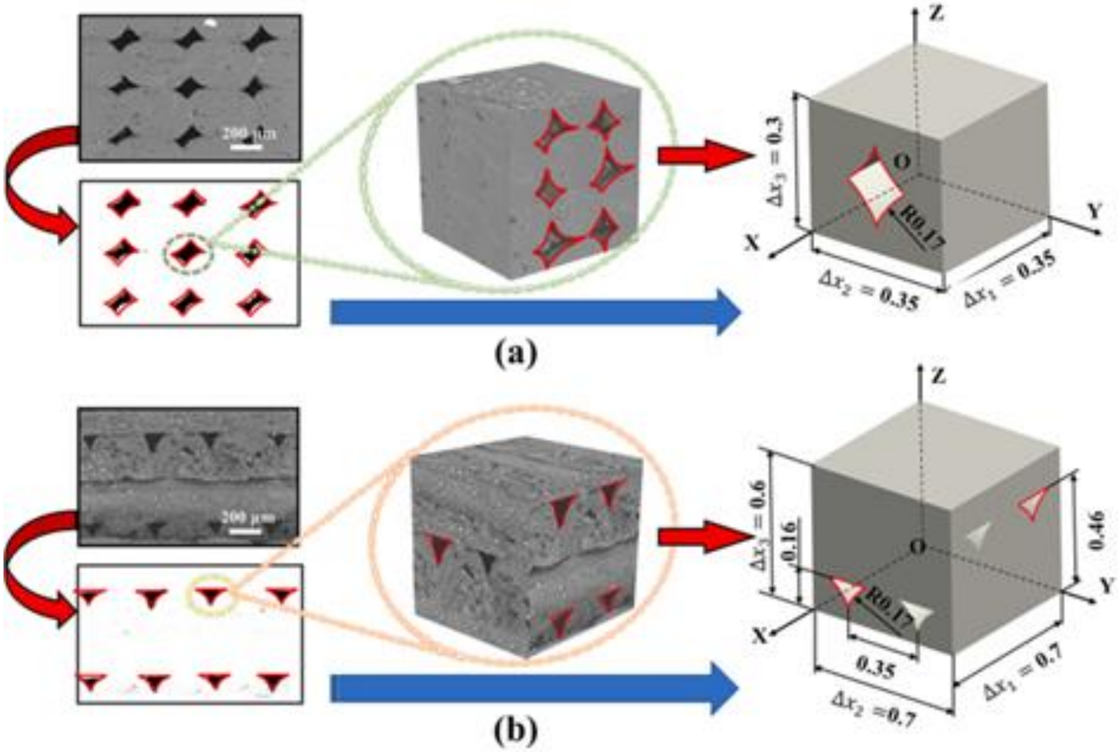

Figure 3.5 Definition of RVE with simplification [77].

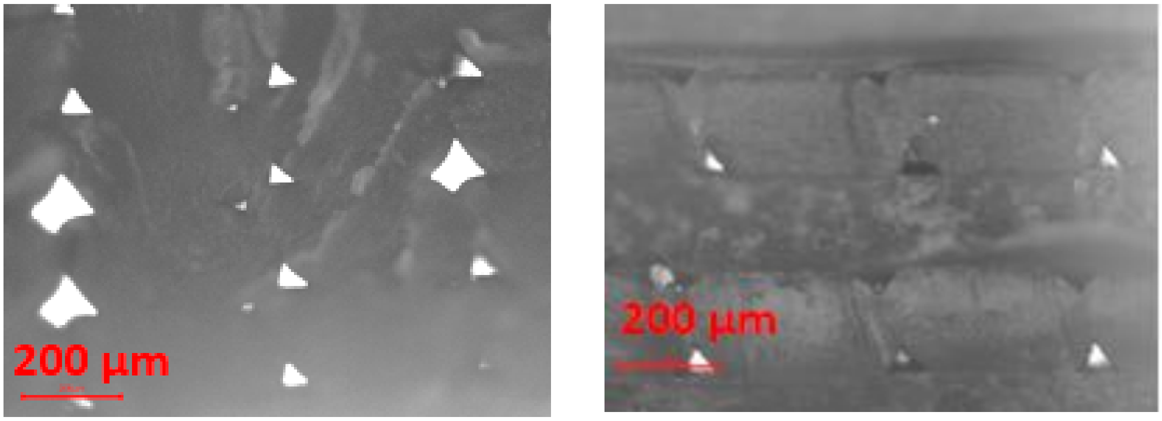

TS

100% infill

Figure 3.6 Microscopic images from tensile test (left), and 100% infill (right) specimens.

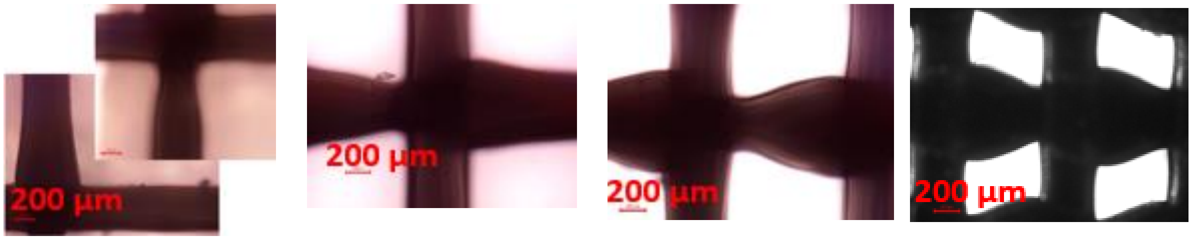

20%_90º 40%_90º 60%_90º 80%_90º

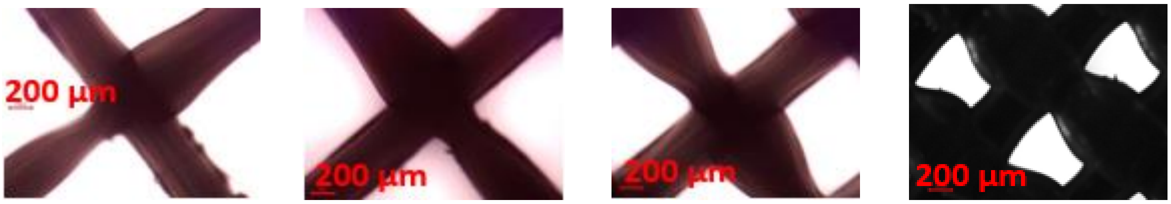

20%_45º 40%_45º 60%_45º 80%_45º

Figure 3.7 Top view sections of different infill ratios and raster angles.

3.3.1 Infill fabrication and unit cells

The cells have different properties in three directions; thus, in the modeling, this point should be considered. In Figure 3.8, the cell occupation in each layer is shown. The cube is made by the walls and the infill section. The walls are always printed with parallel filaments; therefore, their homogenized mechanical properties can be thought of as coming from a unit cell representing the mechanical behavior of the tensile specimens (UCmicro_TS). The geometry of the grid infill is created by overlapping layers with perpendicular lines. To model the influence of this bidirectional behavior in each layer, a UCmeso is generated with the microscopic geometry of the infill and the homogenized mechanical properties coming from a 100% cube (UC_micro_100%). This way, the effect of voids created in the deposition of crossing filaments is reflected.

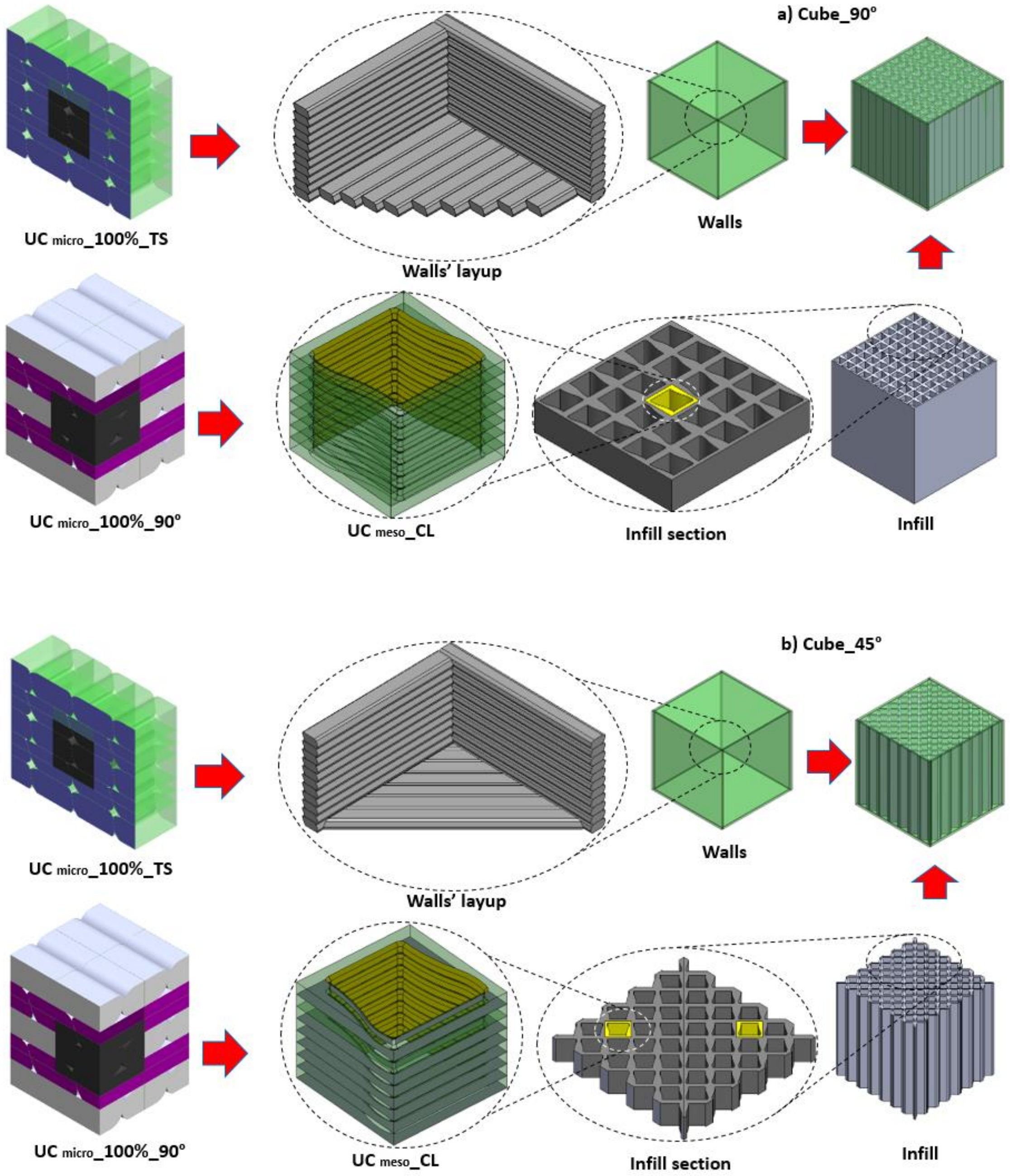

Figure 3.8 Hierarchical modeling from macro-scale (cube) to micro-scale (unit cells), indicating layups for the 90° (a) and 45°(b) cubes.

3.3.2 Periodic boundary condition (PBC)

The method for analyzing the mechanical behavior of a cell that is surrounded by adjacent cells is called the PBC. This formulation imposes constraints on every coupled node located on opposing faces of the cubic elements. This way, although one cell inside the whole body is extracted, the effect and interaction of adjacent cells will be applied to the selected cell. The geometric models developed in SolidWorks and the finite element simulations were conducted using ABAQUS 2022. The analysis is conducted under six different conditions. In the first three scenarios, a normal displacement is applied to one face, while the opposite face is constrained (computing Ei and νij), and the remaining four faces are subjected to periodic deformation, ensuring consistency in their displacement behavior. In the other three for calculating the shear moduli Gij, opposite faces are constrained to exhibit identical displacements, ensuring continuity in deformation. The arrows indicate an applied normal displacement, while the remaining faces follow periodic deformation constraints (see Figure 3.9).

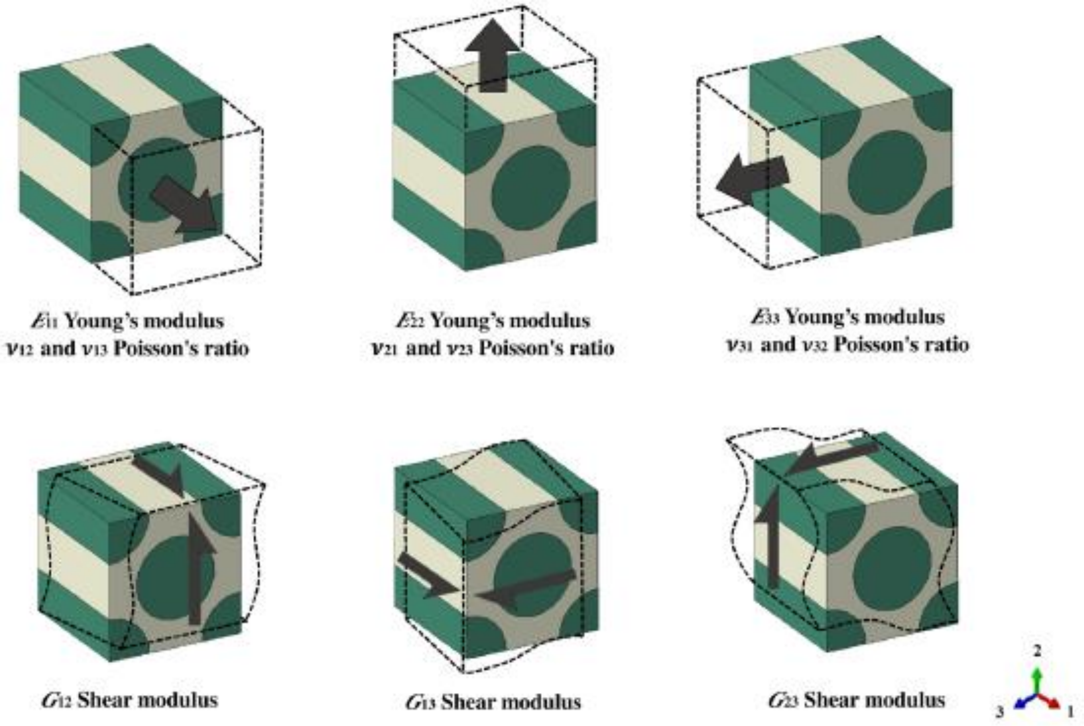

Figure 3.9 General boundary conditions and loads for RVEs [78].

3.3.3 RVU microscale

The unit cell for unidirectional and bidirectional fabrication has been generated, including a realistic volume of void. As shown in Figure 3.10, when the layers are deposited in a parallel direction (unidirectional), the voids are created differently from the perpendicular interlayer deposition (bidirectional). For microscale simulation, this phenomenon should be taken into account.

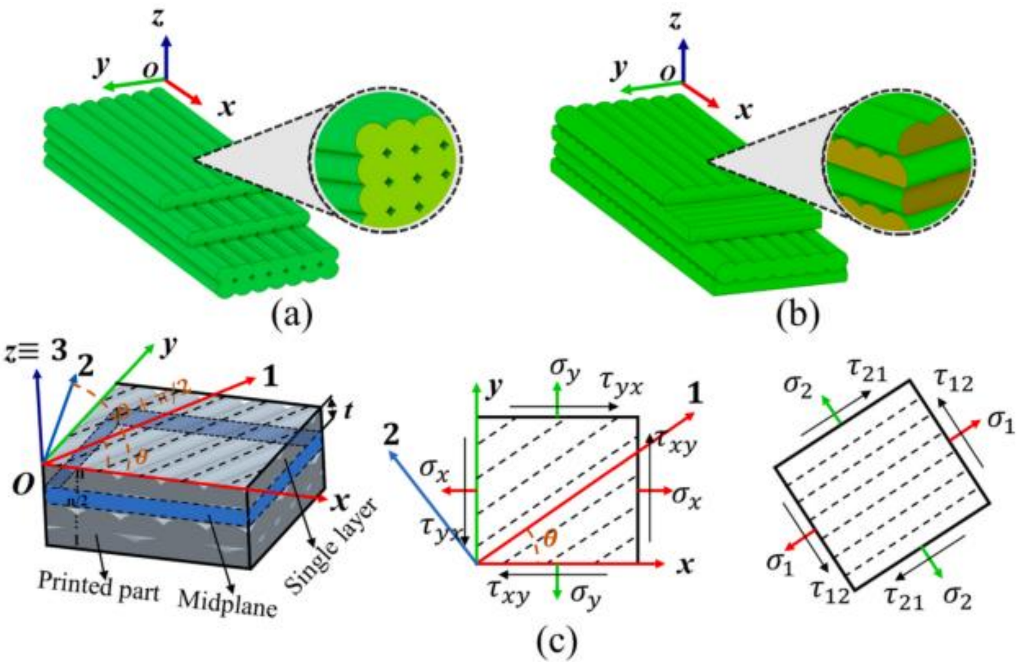

Figure 3.10 Filament orientation in the two typical deposition configurations: (a) unidirectional deposition and (b) bidirectional deposition, (c) the global coordinate system [77].

The deposited filament in this study has a 0.4mm width and 0.2 mm height. The unit cell for this step includes two half-layers in width and height; there is one layer in the middle and two half-layers on top and bottom. Therefore, a 0.4 × 0.4 × 0.4 mm³ cube containing voids was selected as the RVU for the simulation. The geometric parameter indicated in Figure 3.11 is presented in Table 3.1, considering h is 200µm, w is 400µm, and q is 70º for all cases. Measurements indicated that voids occupied approximately 3% of the cross-sectional area of the tensile specimens. Adjusting for voids in the calculation of elastic modulus increased E from 2.84 GPa to 2.93 GPa, while Poisson’s ratio remained constant at $\nu = 0.37$, as it is dependent on strain.

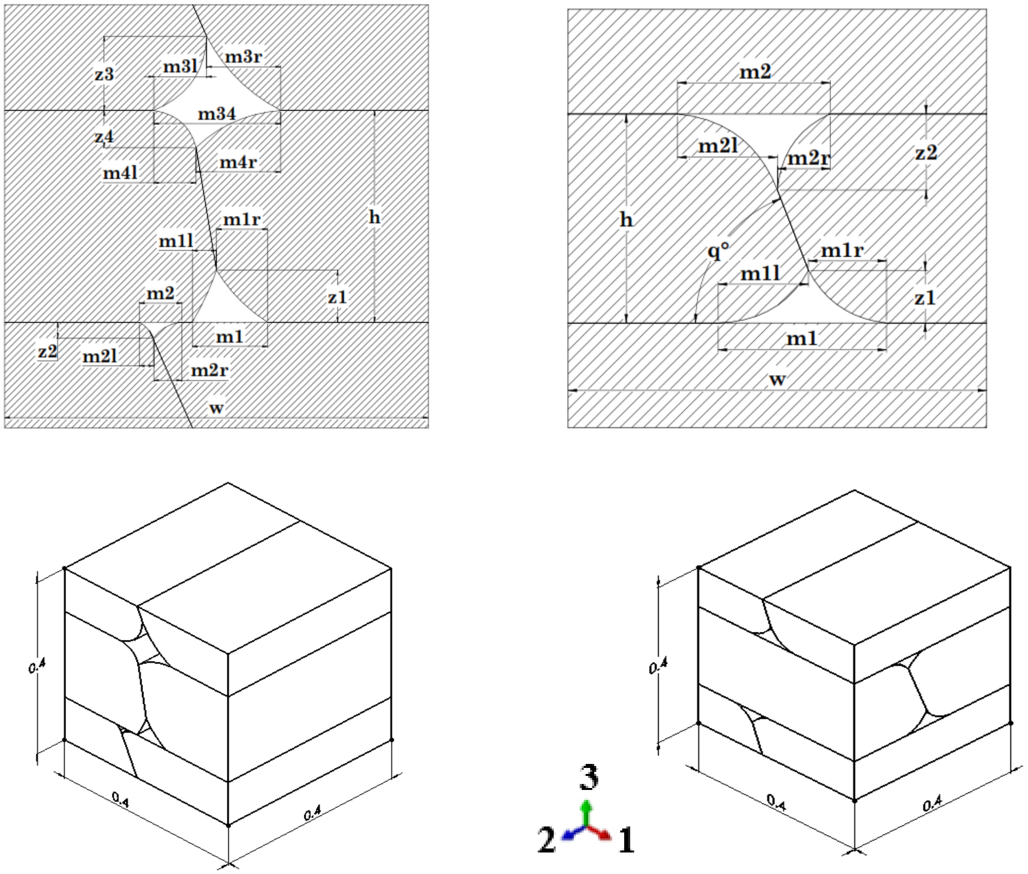

100%_ TS 100%_ 90°

Figure 3.11 Micro-scale unit cells for tensile (left) and 100% infill specimens (right).

Table 3.1 Dimensions in (µm) for modeling voids of RVU microscale

	z_1	z_2	m_1	m_{1l}	m_{1r}	m_2	m_{2l}	m_{2r}
100%_90º	60	40	100	40	60	90	40	50
	z_1	z_2	m_1	m_{1l}	m_{1r}	m_2	m_{2l}	m_{2r}
100%_TS	50	20	60	20	40	30	20	10
	z_3	z_4	m_3	m_{3l}	m_{3r}	m_4	m_{4l}	m_{4r}
	60	30	100	40	60	100	40	60

3.3.4 RVU mesoscale

A unit cell is the smallest repeatable structural element in the infill pattern. According to microscopic images (Figure 3.7) and cells' position and orientation (Figure 3.8), the unit cell properties could be calculated separately. As mentioned in section 3.3.1, in the 3D printing deposition process, from top view observation, the primary lines create a uniform shape wall, and secondary lines generate non-uniform wall thickness. In Figure 3.13 and Table 3.2, the geometric parameters for the cells are demonstrated.

Table 3.2 Dimensions in (μm) for modeling RVU mesoscale

	z	w_1	w_2	m_1	m_2	h_1	h_2	h_m
20%	400	380	700	320	500	860	1000	200
40%	400	400	720	320	520	720	120	200
60%	420	420	760	440	780	120	100	
80%	440	480	800	600	800	150	150	

The reason for having two types of lines is the timing or priority of pathing lines. In the intersection spot of each level, the first passed lines are uniform, and the secondary line is non-uniform. The external dimensions for different infill densities were 4 mm, 2 mm, 1.33 mm, and 1 mm for 20%, 40%, 60%, and 80% infill, respectively.

The simulation model ensured that each infill ratio maintained the same volume fraction of solid material. The engineering constants (EC) derived from the 100% infill (90°) case were applied across all models. Given the orthotropic nature of the structures, a coordinate system was defined for the model to properly assign material properties.

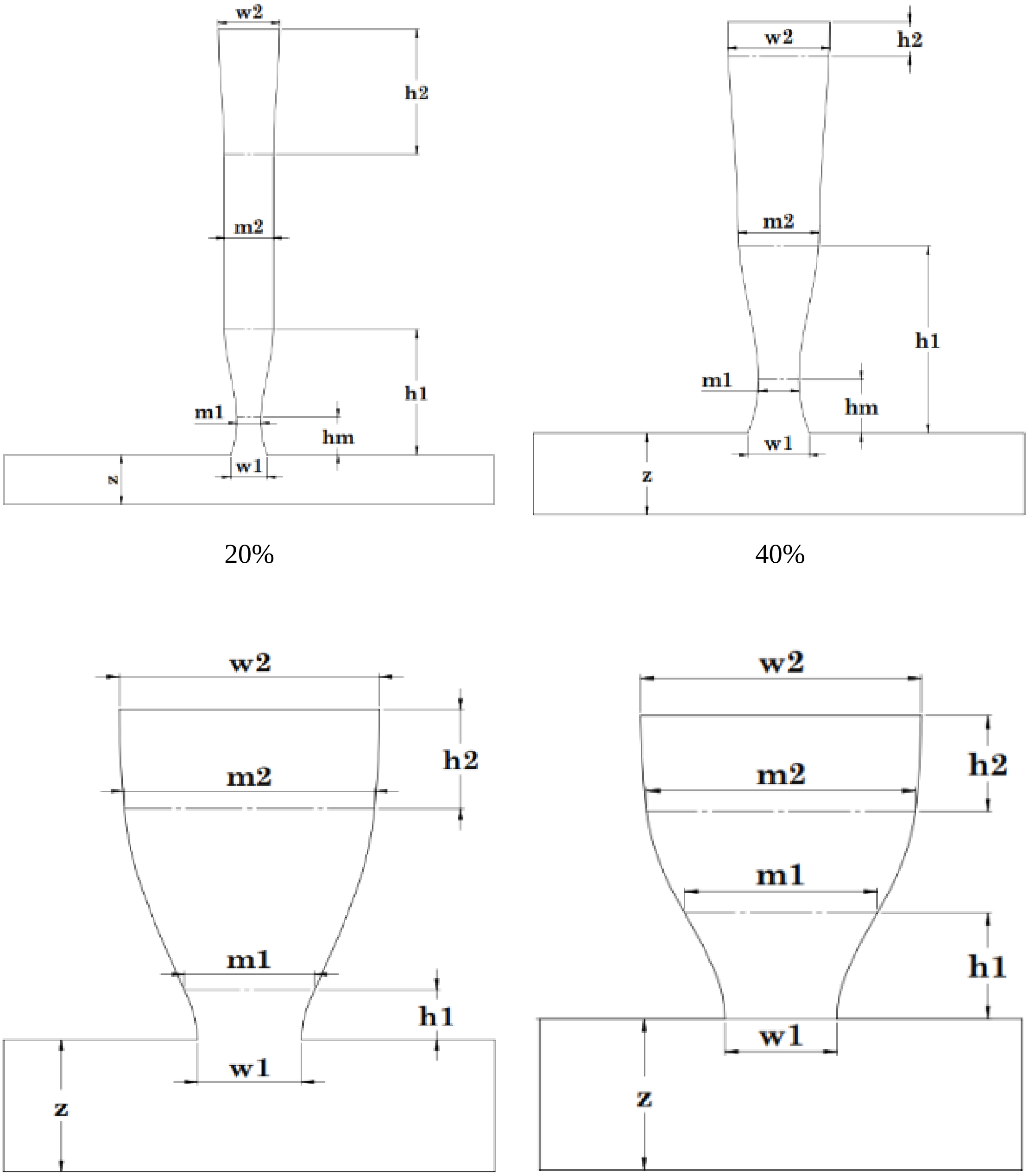

20%

40%

60%

80%

Figure 3.12 Geometric parameters of the cell layers according to the microscopic images.

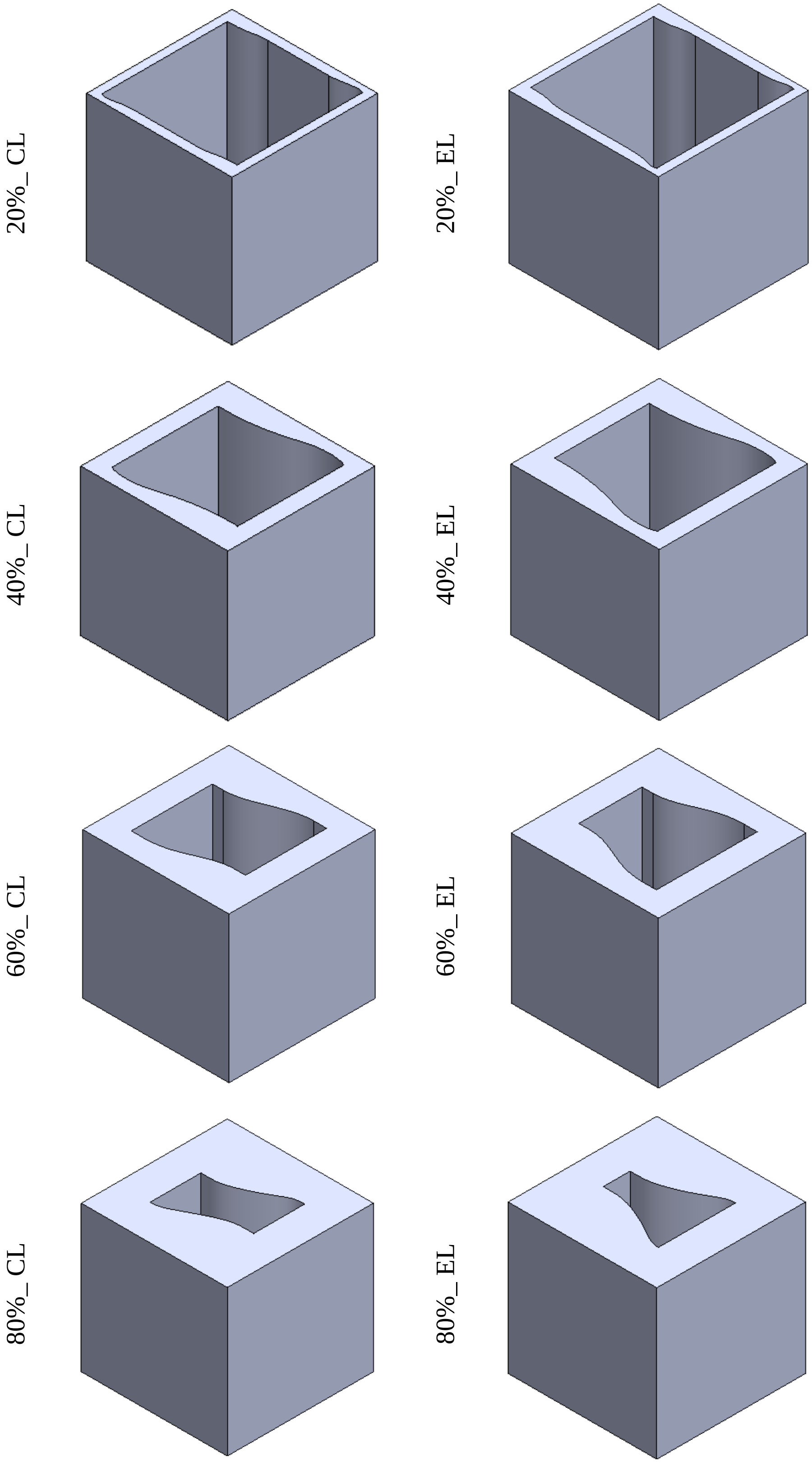

Figure 3.13 Computational models for eight UC categories at different infill densities.

3.3.5 RVU macroscale

The final simulation scale involved modeling full-scale cubic specimens (40 mm per side) and replicating the experimental setup. The arrangement of fabricated filaments determines their mechanical response in multi-axial load analysis. As indicated in Figure 3.8, the walls (unidirectional deposition) and infill (bidirectional deposition) possess various filament arrangements and, consequently, different mechanical behaviors.

The external walls were modeled separately to assign material properties based on filament deposition characteristics (unidirectional deposition), as shown in Figure 3.14. The unit cells shown in Figure 3.13 were analyzed under six boundary conditions described in Section 3.3.2, and the engineering constants were calculated for each unit cell. The infill was modeled as a bulk geometry to define the homogenized properties derived from the UC mesoscale. For 100% density, line patterns were applied for printing pass, while other densities were grid infills. The grid infills for densities 20% to 80% were modeled, instead of 100% infills; both raster angles had the same bulk model, only with a 45° difference in the definition of material properties.

For 90° raster angles, the internal infill was represented as a single cube, while for 45° raster angles, the infill was modeled as two intersecting triangular volumes due to the diagonal nature of the deposition (see Figure 3.14). The walls were assigned ECs from the tensile test RVE simulations, while the internal bulk properties were obtained from UC models corresponding to each infill ratio. The boundary conditions mirrored those of the experimental compression tests: one face was constrained in three directions, while a displacement load (1% of cube length, 0.4 mm) was applied to the opposite face.

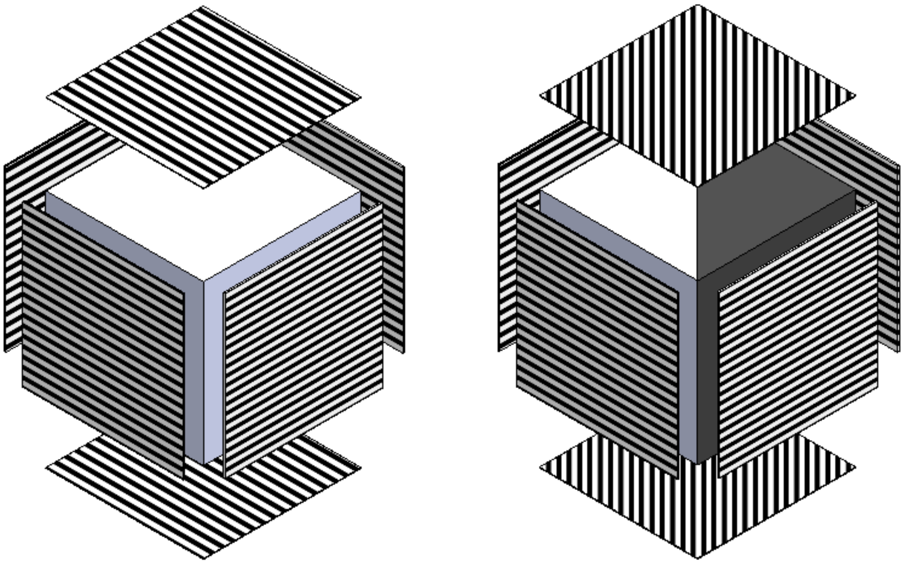

Figure 3.14 Schematic representation of cube sections highlighting different material property definitions, distinguishing between external walls and internal infill regions (left RA:90º and right RA:45º).

3.3.6 Advantages of the RVU method

Two advantages of this methodology are reducing the modeling time and computational efforts. In the macro-scale, only once the geometry is prepared and for each ratio, the input properties will change. In addition, dividing the geometric complexity into three steps of simulation led to the achievement of a suitable mesh and reduced the mesh sensitivity. The mesh sensitivity analysis confirmed low sensitivity for quasi-static loading conditions, leading to a mesh size of 0.01 mm, 0.05 mm, and 1 mm for UC micro, UC meso, and UC macro, respectively (see Figure 3.15 (a)). This method is smart in comparison to free mesh, which is mandatory if all geometrical complexities are in one model (Figure 3.15 (b)). As mentioned, for the periodic boundary condition method, the opposite faces should have completely the same meshing to be able to connect opposite nodes. Therefore, the model and meshing shown in Figure 3.15(b) are not only ineffective but it’s not applicable for the PBC method.

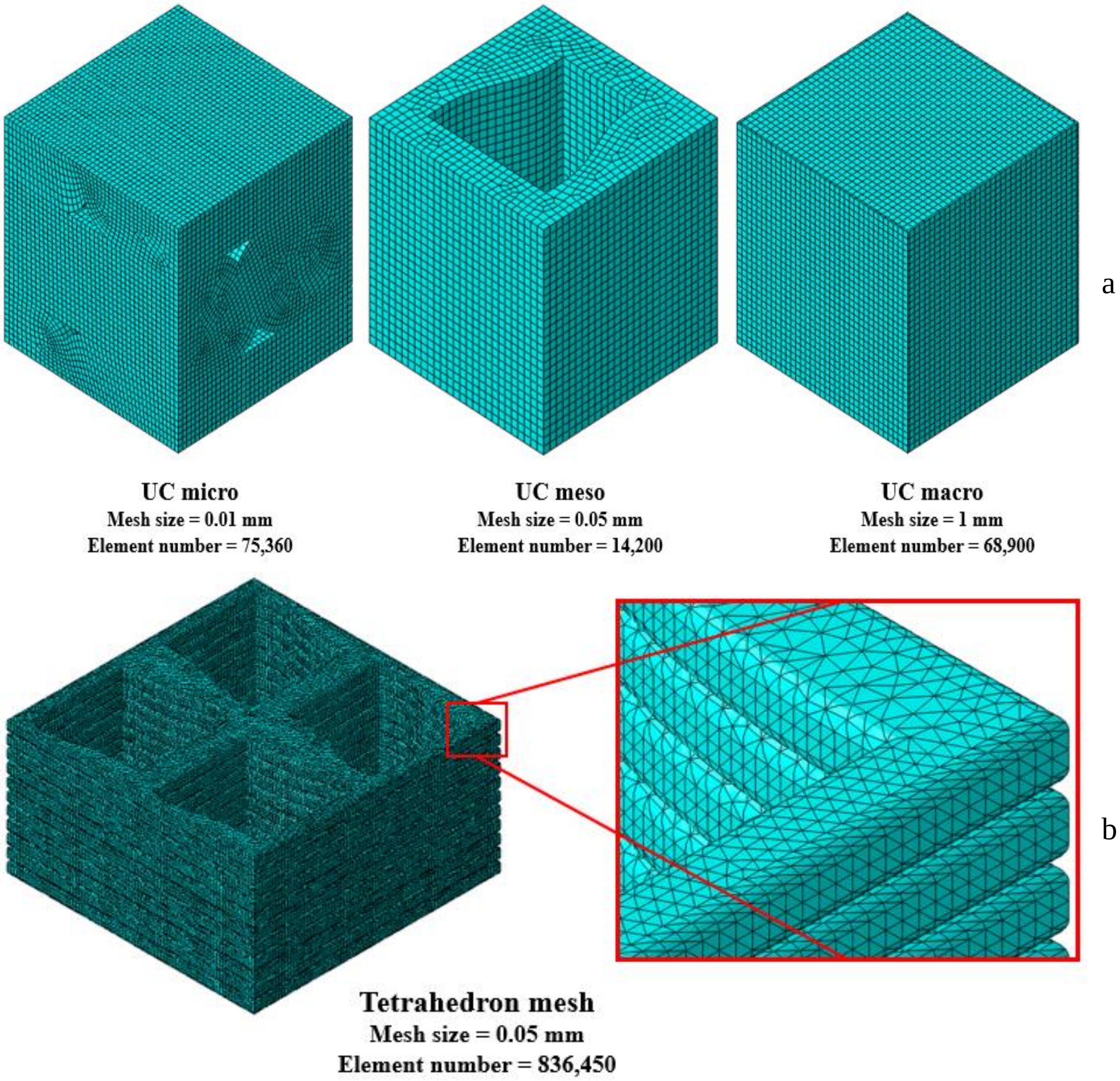

Figure 3.15 Comparison between multi-level smart mesh (a) and tetrahedron free mesh (b).

3.4 Results and discussion

The proposed methodology could be utilized to predict the homogenized mechanical behavior of FDM products containing infills. Using the PBC method, the material properties for the large-scale analysis are measurable. The coordinate system in the simulations was maintained consistent with experimental orientations (E1, E2 for in-plane, E3 for build-up direction). In the following, the results of each scale are described.

3.4.1 Micro-scale results

The main purpose of micro-scale analysis is to differentiate unidirectional and bidirectional deposition. In Figure 3.16, the deformed geometries of UCmicro are illustrated. As mentioned in the previous section 3.1, the results of TS are used as input properties for the bulk model of walls, and the output of infill 100%_90º is taken as input properties of mesoscale unit cells. Table 3.3 presents the engineering constants (ECs) for the two deposition directions, and they are validated by the experimental results. For unidirectional deposition, E2 = 2.84 GPa is equal to the equivalent elastic modulus achieved from the tensile test. For bidirectional deposition, the reference is the compression tests that were conducted on the standard specimens mentioned in Section 2.4.3. Experimental validation of 100% infill (90°) specimens by ASTM D695 confirmed strong agreement between simulated and experimental results.

Key trends from the simulations include:

- In 100%_ TS, E3 ≤ E1 < E2 in which E2 is the deposition direction.
- In 100%_ 90°, E3 < E1 = E2 in which E1 and E3 are both deposition directions.
- In 100%_ TS, (ν13 = ν31), (ν12 = ν32), (ν21 = ν23).
- In 100%_ 90°, (ν13 = ν23 = ν12 = ν21), (ν31 = ν32).
- In 100%_ TS, G13 ≤ G32 ≤ G12, the shear modulus in three directions is close but horizontally larger.
- In 100%_ 90° G13 = G32 < G12, which says the horizontal shear modulus is larger than the vertical.

Table 3.3 Engineering constant of UCmicro simulation and compared with equivalent experimental results.

(GPa)	**E_1**	**E_2**	**E_3**	**ν_{13}**	**ν_{12}**	**ν_{32}**	**G_{13}**	**G_{12}**	**G_{32}**
100%_ TS	2.59	2.84	2.57	0.35	0.33	0.37	0.97	0.99	0.98
100%_ 90°	2.76	2.76	2.18	0.36	0.36	0.29	0.9	1	0.9
ASTM _ 90°	2.82	2.77	2.26	0.36	0.41	0.33			

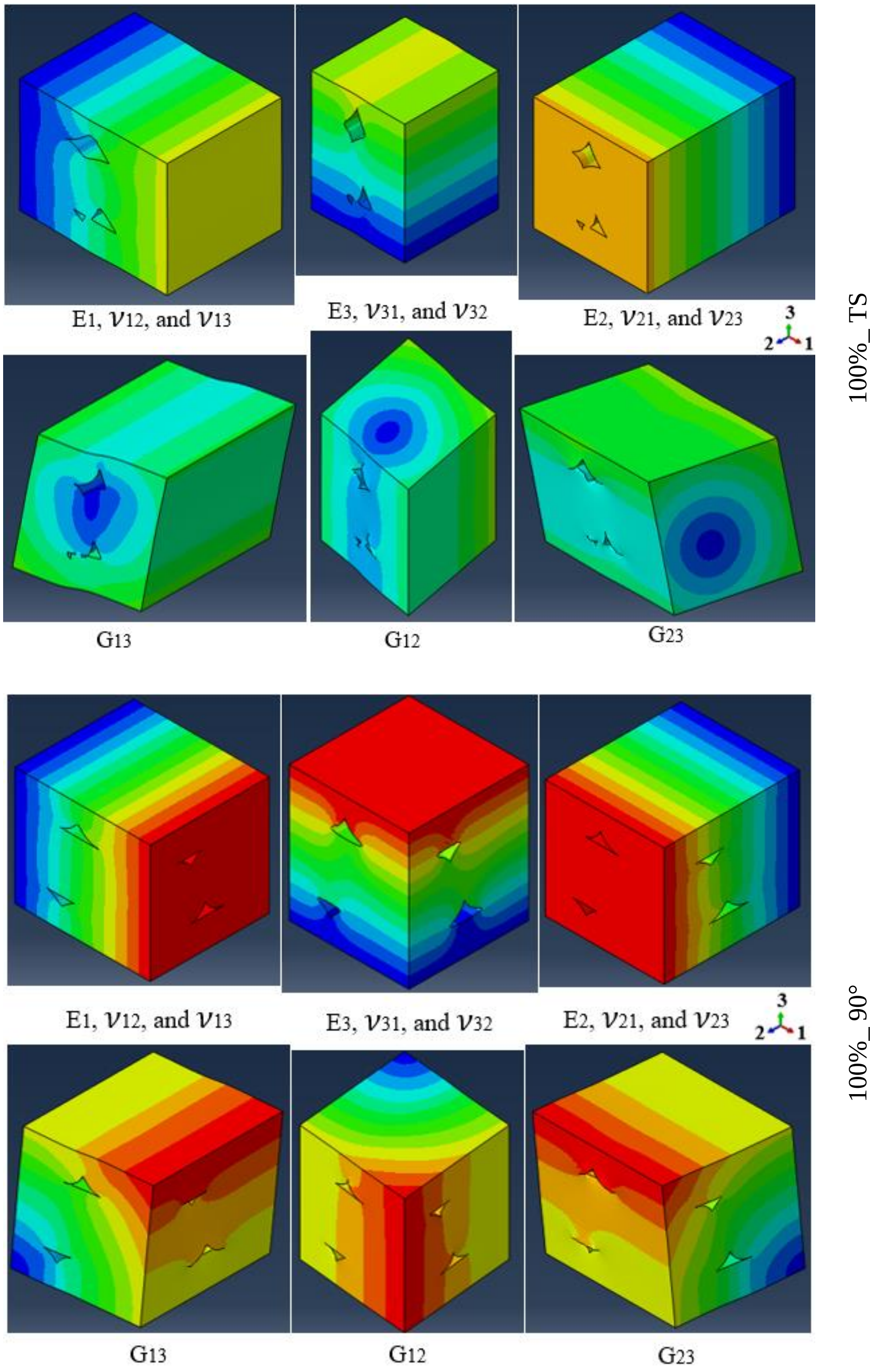

Figure 3.16 Schematic views for six loading conditions and their demonstrative results (UCmicro)

3.4.2 Meso-scale results

This section is a bridge between the effect of voids on mechanical properties and the final geometry. The deformed geometries of UCmeso are illustrated in Figure 3.17, while Table 3.4 describes output ECs. In addition, looking at the output results of the mechanical behavior of the grid infill, the following results will be concluded:

- In UC, E2 ≤ E1 < E3 in which E1 and E2 are the deposition directions.
- In UC, (ν13 = ν23), (ν12 = ν21), (ν32 = ν31).
- In UC, G12 < G32 < G13, which says the shear modulus in three directions is close but horizontally larger.

Table 3.4 Engineering constant of different categories of infill obtained with UCmeso.

(GPa)	**E_1**	**E_2**	**E_3**	**ν_{13}**	**ν_{12}**	**ν_{32}**	**G_{13}**	**G_{12}**	**G_{32}**
20%_ CL	0.291	0.298	0.438	0.193	0.009	0.291	0.102	0.002	0.094
20%_ EL	0.303	0.298	0.438	0.201	0.003	0.291	0.096	0.002	0.094
40%_ CL	0.686	0.613	0.874	0.229	0.076	0.292	0.235	0.023	0.198
40%_ EL	0.707	0.613	0.874	0.236	0.068	0.292	0.23	0.02	0.2
60%_ CL	1.096	0.998	1.311	0.244	0.156	0.291	0.378	0.123	0.339
60%_ EL	1.101	0.997	1.307	0.245	0.132	0.291	0.370	0.121	0.340
80%_ CL	1.667	1.456	1.741	0.279	0.247	0.291	0.591	0.377	0.513
80%_ EL	1.657	1.457	1.741	0.277	0.229	0.291	0.577	0.389	0.515

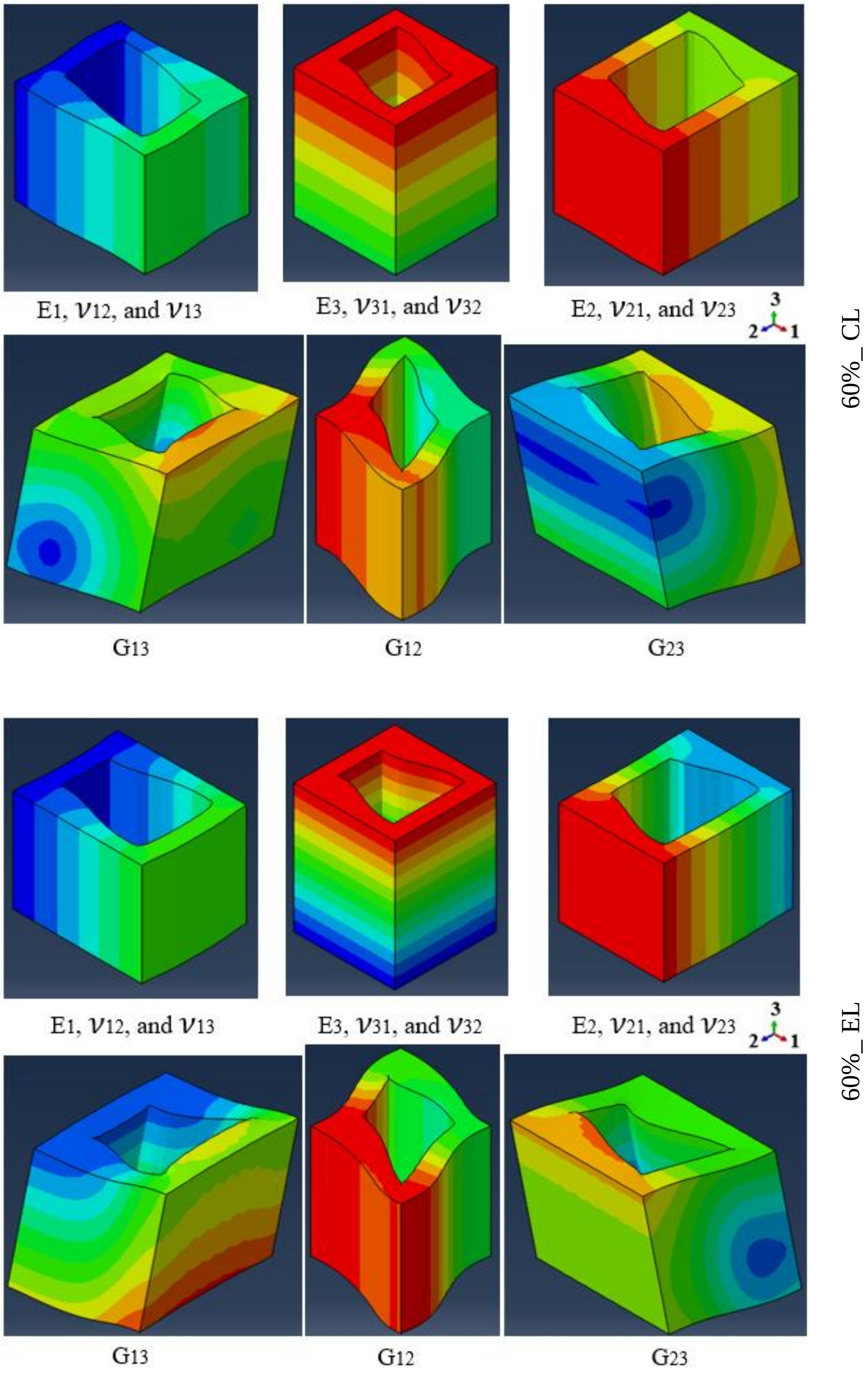

Figure 3.17 Schematic views for six loading conditions and their demonstrative results (UCmeso).

3.4.3 Macro-scale results

In this step, the scale of evaluation is to consider the surrounding walls of the FDM printed part as a homogenized material, paying attention to the deposition direction. On the other hand, having homogenized properties of infill in different densities, this kind of geometry could be simplified in modeling by using the bulk geometry, while the assigned properties should be defined from the directional analysis of the unit cell. Now, the target geometry under application load could be simulated by putting together the homogenized data of walls and infill to perform simulations. In this section, the homogenized properties of cubic specimens, obtained from both experimental tests and numerical simulations, are compared. In the simulation, likewise the experiment, the cubes were compressed in three directions (see Figure 3.18).

The primary objective of this study was to investigate the multi-directional mechanical behavior of grid infill structures and develop a methodology for efficiently predicting these homogenized properties. The findings indicate that as the infill ratio (IR) increases, these properties exhibit both linear and nonlinear variations depending on the loading direction. The comparison illustrated in Figure 3.19 demonstrates that the simulation approach can effectively predict the mechanical behavior of structures internally fabricated with grid infills, with an average deviation of approximately 8% between experimental and simulated results. Figure 3.19 presents the trend of elastic modulus variations at different densities for 45° and 90° deposition orientations, based on both experimental and simulation data. These results provide insight into the mechanical performance of grid infills under varying deposition angles.

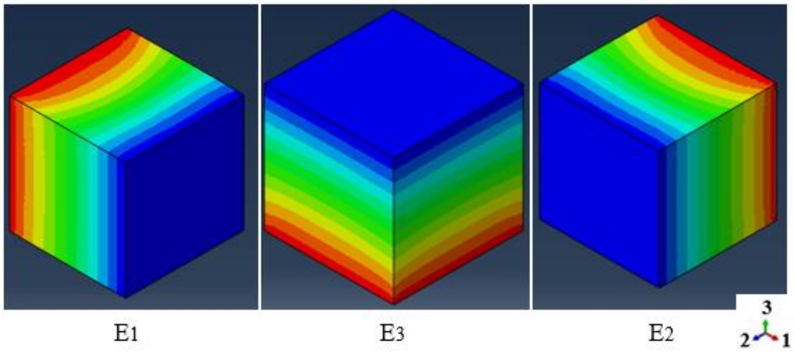

Figure 3.18 Deformation contour for cubic specimens under compression.

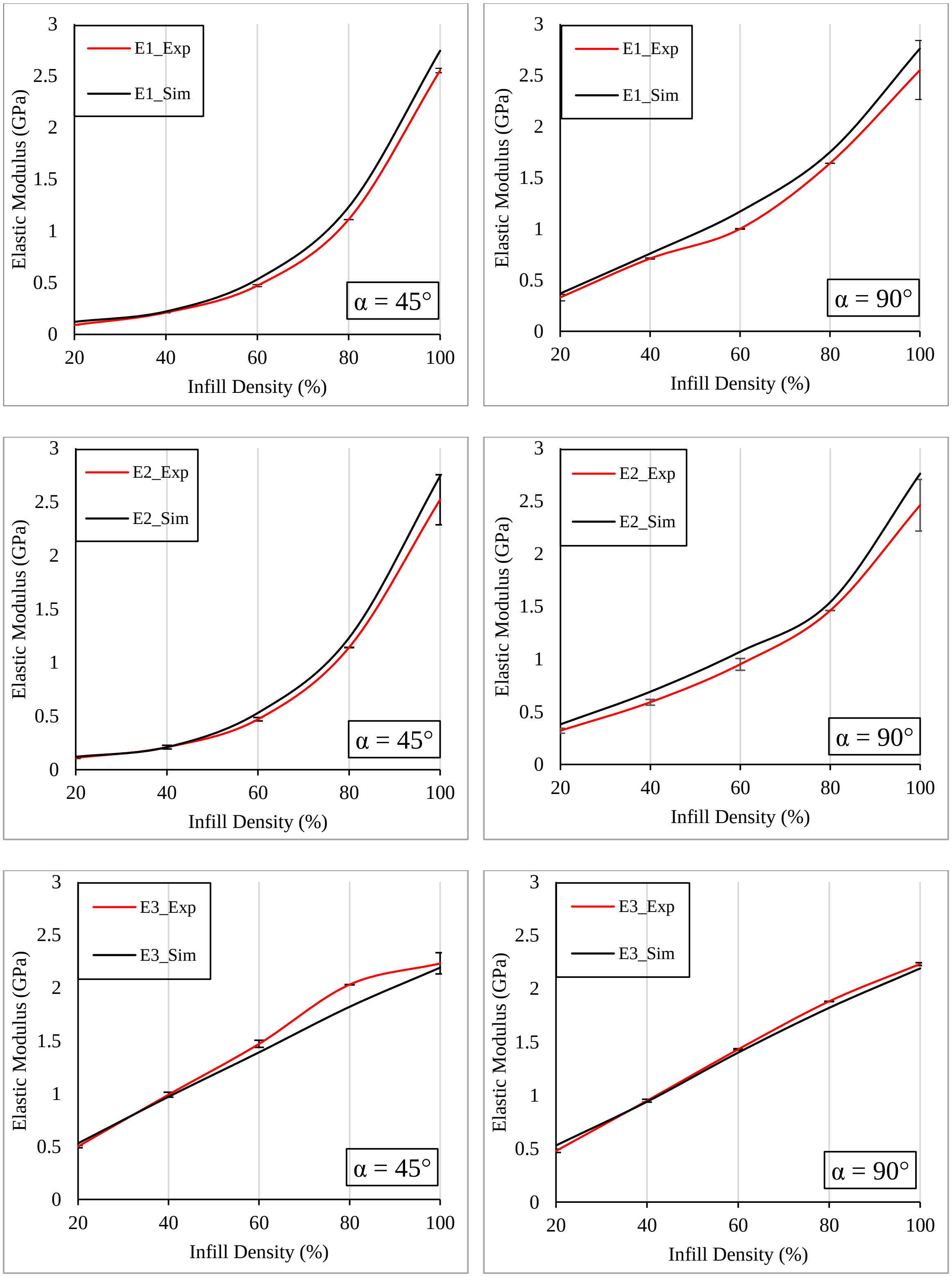

Figure 3.19 Comparison of experimental and simulation-based predictions of elastic modulus for (left) 45° and (right) 90° raster angle across varying infill densities.

3.5 Conclusions

A nominal and real geometry model with isotropic properties can predict the structural behavior with a difference from experiment of 19%. This method is helpful but with less accuracy to show the anisotropic essences.

Multi-scale microstructural evaluation improves accuracy. A hierarchical modeling approach incorporating void analysis, unit cell characterization, and bulk material homogenization enhances the accuracy (8% difference from experimental results) of mechanical property predictions. This multi-scale method is recommended for future design optimization. These findings contribute to the optimization of 3D-printed grid structures by providing quantitative insights into their mechanical behavior. Performing the simulation this way helps the designers be careful in design modification and aware of the effect of geometric parameters defined in the slicer software.

Chapter 4

Cylindrical lattice structures under internal pressure

4.1 Introduction

In this chapter, two different areas of study are combined: design and manufacturing lattice structures, and applying internal pressure. Internal pressure is a classic load case that defines whether a cylinder can withstand a certain circumferential load. The thin-/thick-wall formulas are summarized neatly in reviews of simple hoop-stress rules and their ranges of validity [79]. The study of internal pressure has a vast extent from huge and thick concrete vessels, metallic, and composite samples to small and thin membranes [80-83]. As indicated in Figure 4.1, imposing internal pressure is commonly applied by fluids.

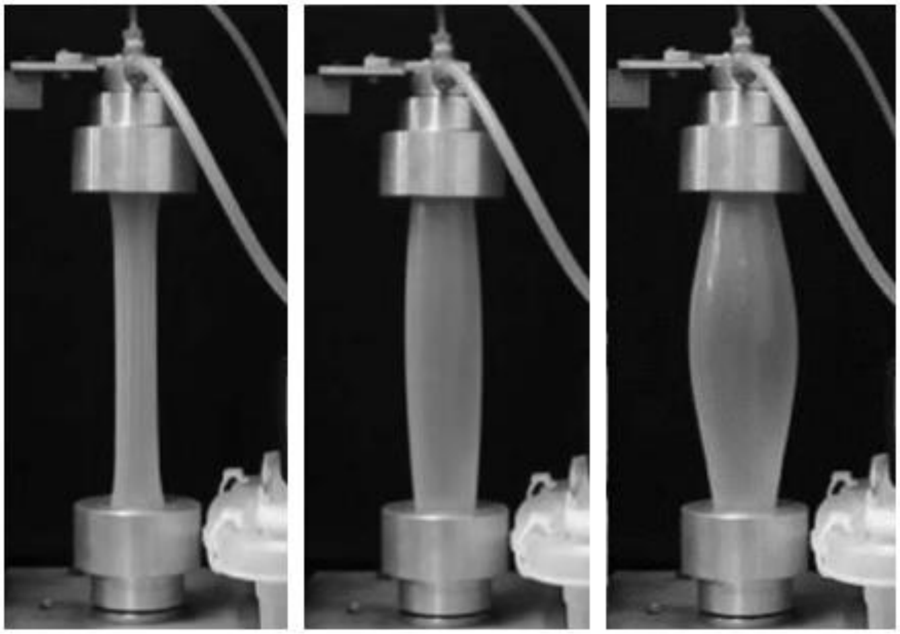

Figure 4.1 Stretched membrane under internal pressure [80]

In biomedical applications, one interesting and practical structures are Balloon-expandable stents. These biomedical lattices are periodic cylindrical structures made of crowns and bridges. Analytical models that exploit cyclic periodicity capture the apparent elasto-plastic response under balloon pressure and collapse the nonlinear behavior into master curves across geometries [84]. Despite biomedical and mechanical research on these structures, what is intriguing is the same application they used to evaluate the lattice structures shown in Figure 4.2, close to the presented structures in this thesis.

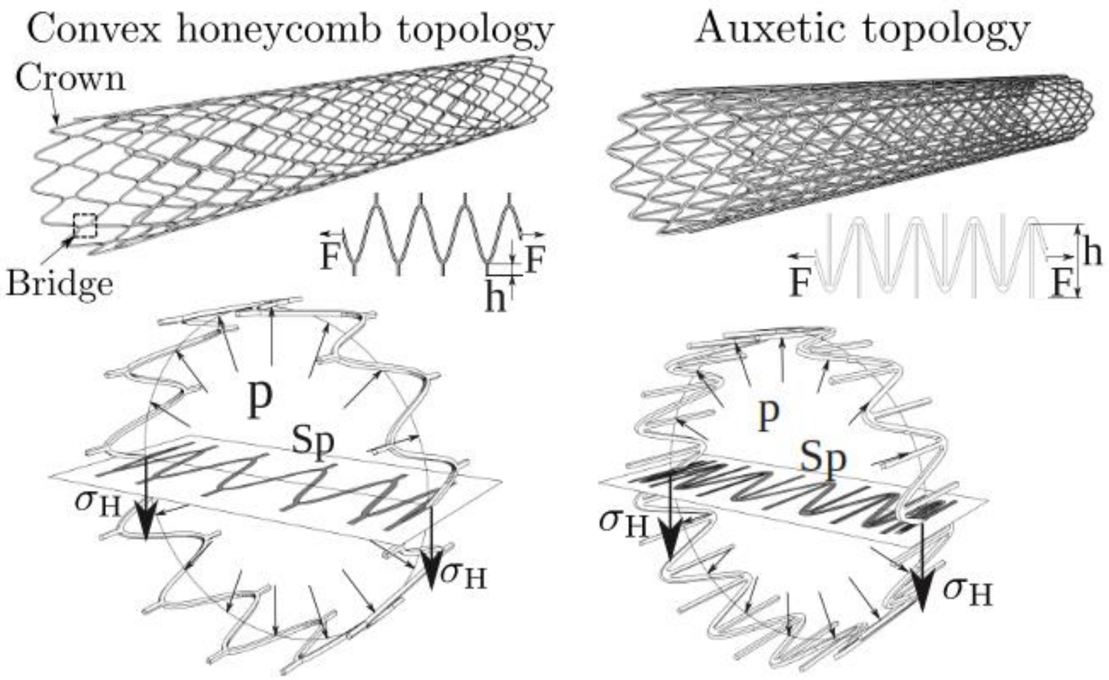

Figure 4.2 Cylindrical structures expanded by balloon radially but contract along their length [84]

Filtering and purification are essential in the food industry, chemical industry, and medical science. In the separation of different mixture materials, a common way is to cross them through a screen or sieve. Depending on the process in the industry, it could be a dry or wet volume. In this study, the idea is to evaluate the stiffness and strength of lattice structures subjected to internal pressure. These structures should have a controlling perforation and be strong enough. To control the perforation, the design has geometric parameters free to be modified. To ensure the safety of the structure, stiffeners are added that create a hybrid lattice.

In the next step, the designed bodies are 3D printed with stainless steel 316 using SLM technology. Subsequently, the experimental test on 3D printed specimens was conducted, and finally, the FEM simulation was applied to the model to illustrate more information. The evaluation of conditions for design requires being aware of SLM and critical dimensions.

4.2 Geometry and Specimens

One of the advantages of 3D printing is producing complex geometries with more freedom. Lattice structures are highly engineered 3D networks of repeating cells, and their design is intricated because not only does the cell geometry selection matter, but also how that geometry changes in space—cell size, orientation, and grading—to meet specific targets like stiffness, strength, or permeability. A particular type of lattice is honeycomb—2D cellular core extruded through thickness—that is the focus of this chapter. The target cell in this study is an extruded diamond-shaped net with the selected geometrical parameters (cell thickness (CT), cell width (CW), and cell depth (CD)) in Table 4.1. The geometric optimization started by selecting two types of cells (rough and fine). In addition to size the the relative dimensions are different (CT/CW = 67%) for fine cell and (CT/CW = 44%) for rough cell.

The selected cells need to occupy the circular space and make a cylinder in which the cell depth is the cylinder thickness. Another aspect of engineering is to have decent integrity in structures. Therefore, to be sure about the strength of the components, one method is to add stiffeners. Here, the stiffeners have a wider net, with a longer depth. This way, a hybrid cylindrical structure is under internal load to investigate its mechanical responses.

Table 4.1 Dimensions of unit cells and stiffeners for fine and rough cells.

(mm)	**CT**	**CW**	**CD**	**SW**	**SD**
Fine	0.2	0.3	0.5	2.5 and 5	3.5 and 7
Rough	0.4	0.9	0.5	4 and 8	3.5 and 7

To have a precise design with high quality, the limitations of the selected printing technology should be considered. In SLM technology, to have a suitable surface quality and a convenient printing job, the design should have an overhang angle of more than 45º. To ensure the 3D printing efficiency in this study, a 60º overhang angle is considered. In Figure 4.3, the cell parameters and the relative position of the stiffeners are indicated.

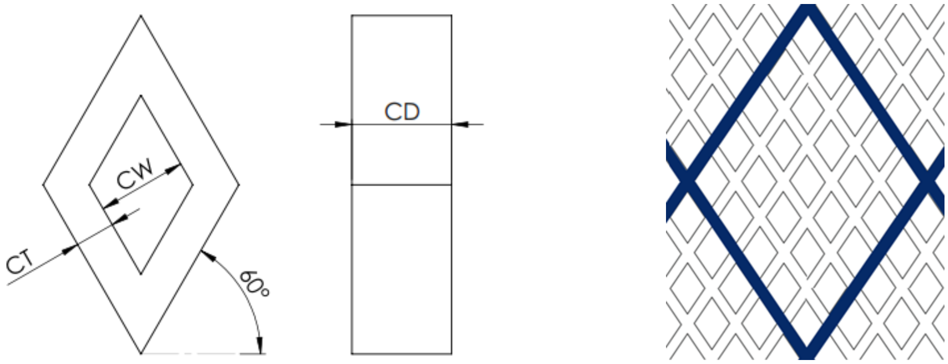

Figure 4.3 Unit cells geometric parameters.

4.2.1 Modeling in nTop

The nTop software has been used in recent studies as an implicit, field-driven platform to create and evaluate lattices for both fluid and structural performance. Geometry is represented by mathematical fields (not B-reps/meshes), so booleans, offsets, blends, and very large lattices are robust and fast—ideal for TPMS/beam lattices and graded porosity. Unit-cell type, size, and strut thickness can be varied by simulation fields (e.g., stress, temperature, distance) or analytic formulas to evaluate stiffness, density, or permeability. This capability is widely applied in aerospace heat exchangers, lightweighting, and medical implants.

In the previous studies, sheet-based TPMS variants (Gyroid, Diamond, Lidinoid, etc.) were generated and parametrically varied in porosity, unit-cell size, and strut thickness. In one research, a hybrid hierarchical lattices were built by embedding a small-scale TPMS within a sheet-network scaffold while holding overall relative density fixed via iso-value control, then assessed via unit-cell homogenization, yield, and energy absorption. Another study modeled and analyzed strut-based lattices (re-entrant, truncated-octahedron, Kelvin cell, octet) directly in nTop with static finite-element simulations under bending, enabling comparisons of displacement, stress, failure mechanisms, and stiffness across cell type and material. The examples of literature using nTop show that this software can help engineers to (i) generate complex lattices with implicit modeling, (ii) tune properties through field/density control, and (iii) link geometry to testing and FEA to explain how topology and material choices drive flow and mechanical responses [85-87].

In general, nTop is an advanced and new tool for optimization-oriented complex lattices, dealing with comparing geometric parameter options for easy design and modification. Here, a short description of the options used for the present model of this chapter is given. A shell cylinder is imported into the software (Figure 4.4a). Then the unit cell (UC) is selected square honeycomb rotated (Figure 4.4b). Afterward, the face is mapped by cells (Figure 4.4c, d). The number of cells is defined to reach the considered geometry. In consequence, UC is placed on the cells, and a periodic lattice structure is generated (Figure 4.4e). For creating the stiffeners, two modifications are required: reducing the number of cells and increasing the depth of cells (Figure 4.4f).

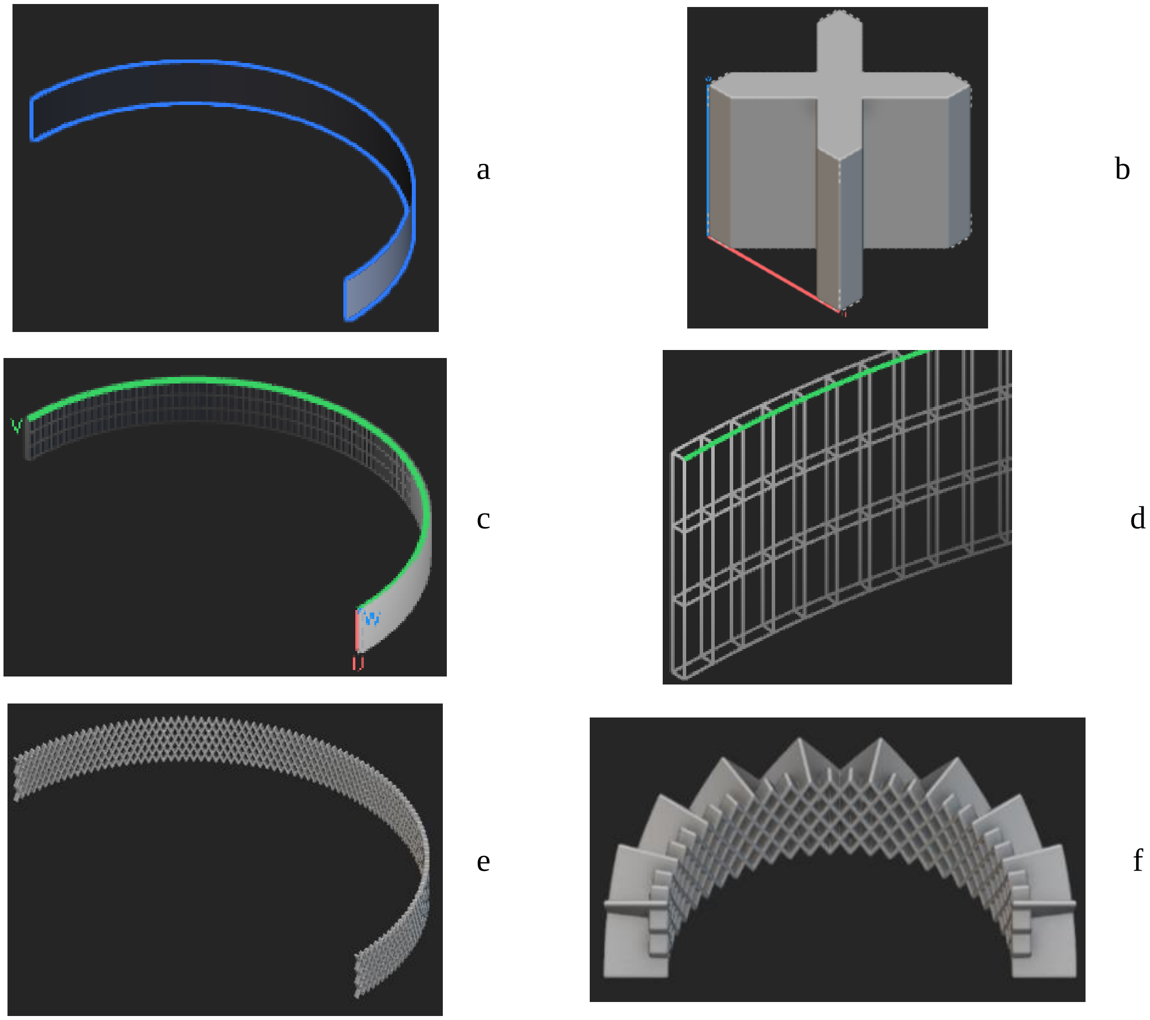

Figure 4.4 Generating the model in nTop.

4.2.2 Specimens manufacturing

This study aims to investigate of geometrical parameters of a hybrid structure. A cylinder with an internal diameter of 25mm and a length of 100mm has been designed. For both fine and rough cells, there is a layer of dense cells (core) with 0.5mm depth and the stiffeners in the outer layer are connected to them. The target was to see the effect of the dense core and stiffeners separately. To isolate this effect, the core cells were held constant within each family (fine vs. rough), and four distinct stiffener variants per family were created by systematically varying width and depth while maintaining comparable mass. In Figure 4.5, the 8 types of lattice specimens are shown. The specimens are indicated by a letter R as rough cell and F as fine cell. The number after the letter represents the number of cells inside the stiffeners. The number after the dash shows the external diameter of the cylinder. By this design, core and stiffener influences were decoupled, the ability of thicker/wider stiffeners to compensate for a coarser core was assessed, and the translation of geometric increments into micrometer-scale reductions in diameter growth was mapped. In summary, the four types of stiffeners for each cell type were established to provide a controlled, apples-to-apples evaluation of the premise that sizing stiffeners yields the largest and most cost-effective gains in radial stiffness, independent of printing variability and boundary conditions.

In Figure 4.6, the geometric parameters for this modeling are shown. Some of the dimensions, such as ID (25 mm) and CD (0.5 mm), are the same for all specimens. The other two dimensions differentiate fine cell (CT = 0.2 mm, CW = 0.3 mm) and rough cell (CT = 0.4 mm, CW = 0.9 mm). In Table 4.2, the dimensions for the 8 considered configurations are shown. For the models with an odd number of cells in a circle (NCC), the half circle is modeled.

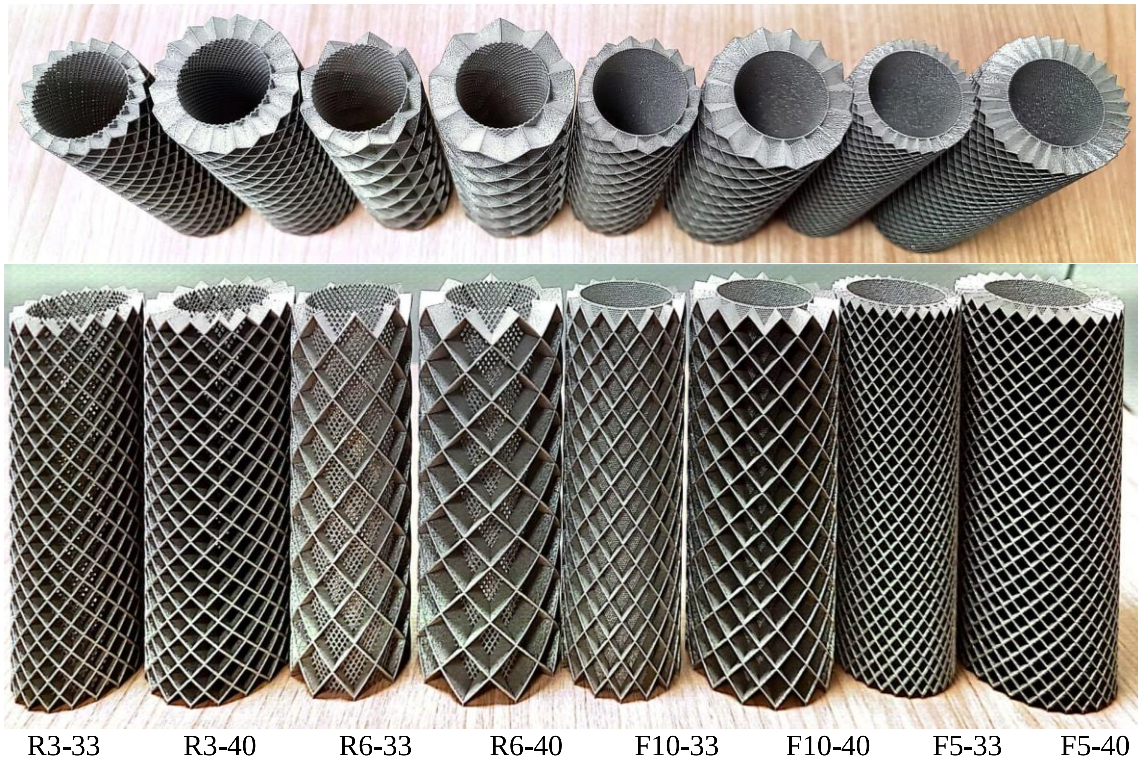

Figure 4.5 The eight 3D printed cylindrical lattice specimens.

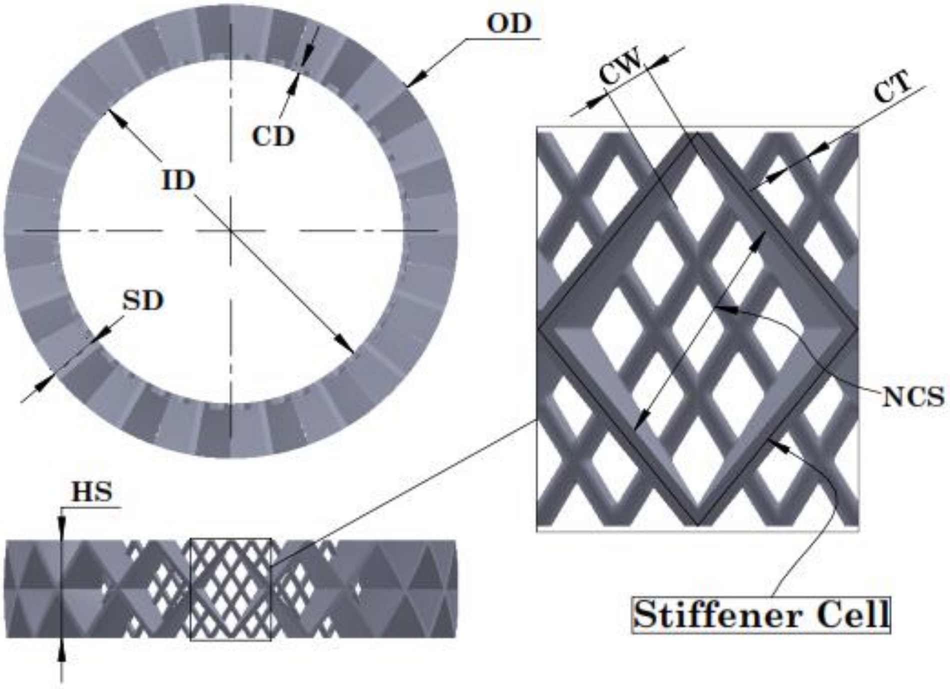

Figure 4.6 Geometric parameter (all in mm) of the 8 cylindrical specimens.

Table 4.2 Dimensions of geometric parameter (all in mm) of the 8 cylindrical specimens.

	Core cell	**SD**	**OD**	**NCS**	**HS**	**NCC**	**Model**
R3_33	Rough	3.5	33	3	7.15	18	Quarter
R3_40	Rough	7	40	3	7.15	18	Quarter
R6_33	Rough	3.5	33	6	14.3	9	Half
R6_40	Rough	7	40	6	14.3	9	Half
F5_33	Fine	3.5	33	5	5	30	Quarter
F5_40	Fine	7	40	5	5	30	Quarter
F10_33	Fine	3.5	33	10	10	15	Half
F10_40	Fine	7	40	10	10	15	Half

4.3 Experiment method

The experimental test for this research has two parts. First, performing internal pressure on cylindrical lattices. The target was to observe the behavior of the designed structure under application load. To make the test, a test rig is needed to ensure the load is perfectly imposed on the structure. Second, rectangular cubes were designed and manufactured to find the anisotropic behavior of the lattice structures (core cells). This test was a common compression test to evaluate the stiffness and strength of the fine and rough cells.

4.3.1 Test rig for internal pressure

The structure contains hollows that cannot be pressurized without an intermediate part. Therefore, the first step was to make a setup that is sealed and can apply controllable pressure on the internal face of the structure. In Figure 4.7, the tube and sealing components are shown. On one side, the tube is closed, and on the other side, air or water is introduced.

Figure 4.7 Setup of the tube carrying out pressure and the sealing components.

4.3.2 Pneumatic (air pressure) test

A deformable hose has been prepared to inflate the air into it and transmit the pressure to the lattice. The ideal conditions were considered on the fixture to increase the accuracy of the measurement. On both ends of the specimens, a thin metal with high surface quality has been placed to reduce the friction. To avoid tilting or sliding or any displacement despite expansion, the fixture and hose have been restricted in all degrees of freedom of the specimens, and the bottom of the specimens was fixed radially. The pressure is raised to 8 bar at the rate of 0.3 bar/second. A digital pressure gauge (ALMEMO) is in the loop and records the pressure every 0.1 second. Meanwhile, the radial expansion is recorded via DIC using two cameras and analyzing the data with Alpha software (see Figure 4.8). In increasing the air pressure, the control valve helps to raise the pressure smoothly and linearly (see Figure 4.9).

Figure 4.8 Digital image correlation setup and digital pressure gauge

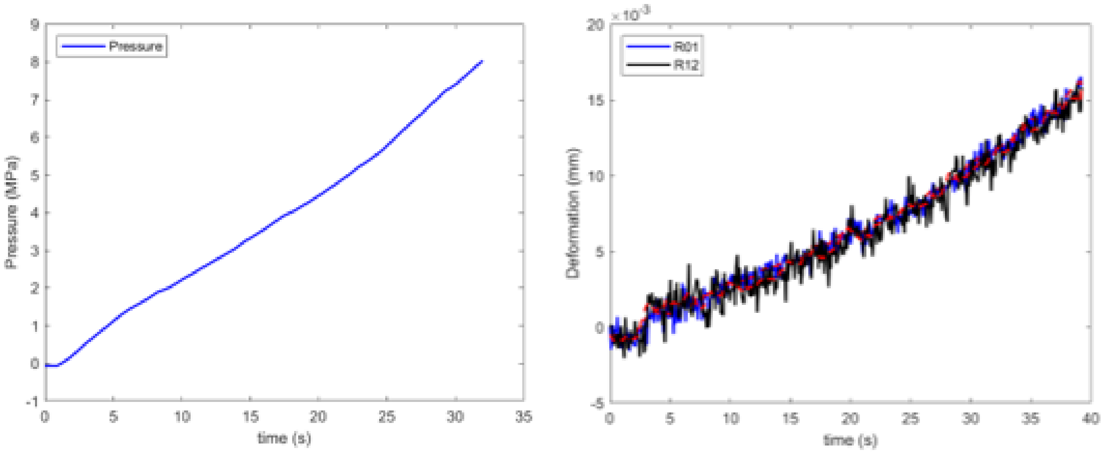

Figure 4.9 Pressure and expansion according the time for pneumatic test.

4.3.3 Hydrostatic (water pressure) test

The specimens’ strength was above 8 bar, and the air pressure equipment has reached the limit. Therefore, a water pressure setup has been prepared to apply the pressure to 20 bar at the rate of 1.2 bar/second effectively. This way, there was a comparison between the two test setups, and with higher expansion (see Figure 4.10). In increasing the water pressure, the handle raises the pressure step by step and not continually. Therefore, the pressure curve and consequently expansion are not linear (see Figure 4.11).

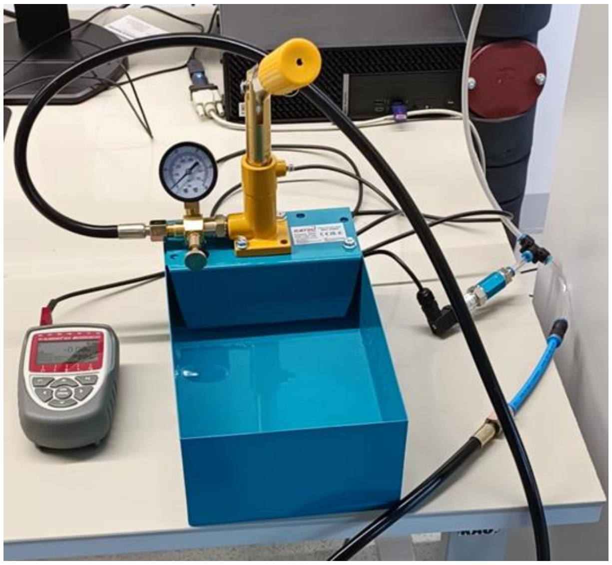

Figure 4.10 Hydrostatic pressure actuator setup.

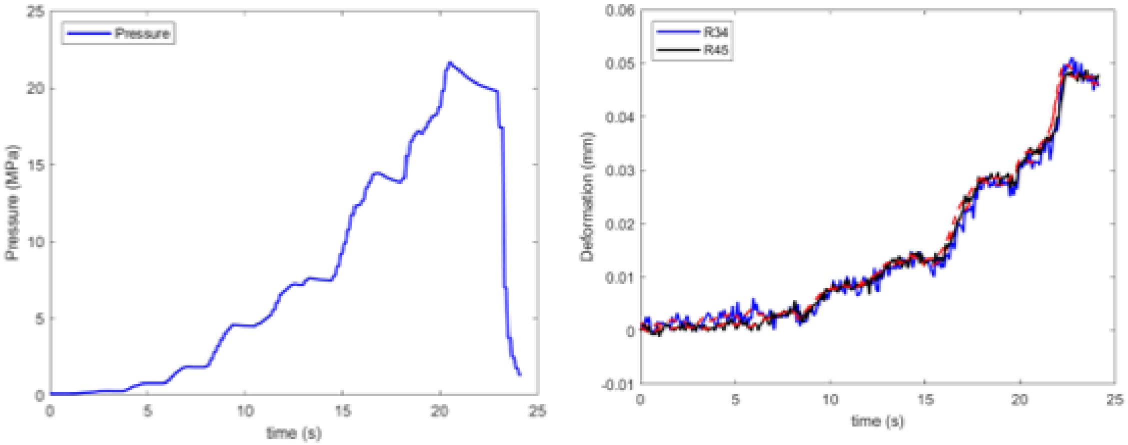

Figure 4.11 Pressure and expansion according the time for the hydrostatic test.

4.3.4 Evaluation of the deformation

As shown the Figure 4.12 (a), with a large-scale vision, the diameter of the cylinder will expand and the length will reduce. According to the position of cameras shown in Figure 4.12 (b), the displacement of the external sections of the lattice every 0.1 second is tracked in the Cartesian system. The scale of deformation is low (less than 50 micrometers). In this scale, the small rigid body motion will affect the test accuracy. The axial displacement (here Y direction) was measured and it is negligible compare to radial deformation. To avoid this phenomenon, the relative displacement between two points was measured to calculate the expansion, Figure 4.12 (c). For each specimen, three set points at different heights are selected to record the displacement shown in Figure 4.12 (d). Afterward, the deformation is converted to the polar system according to Equations (4.1) and (4.2). In these equations, Li represents the distance between a pair of points calculated by Equation (4.1), and the external radius before (r_1) and after (r_2) deformation is calculated by getting the relative length.

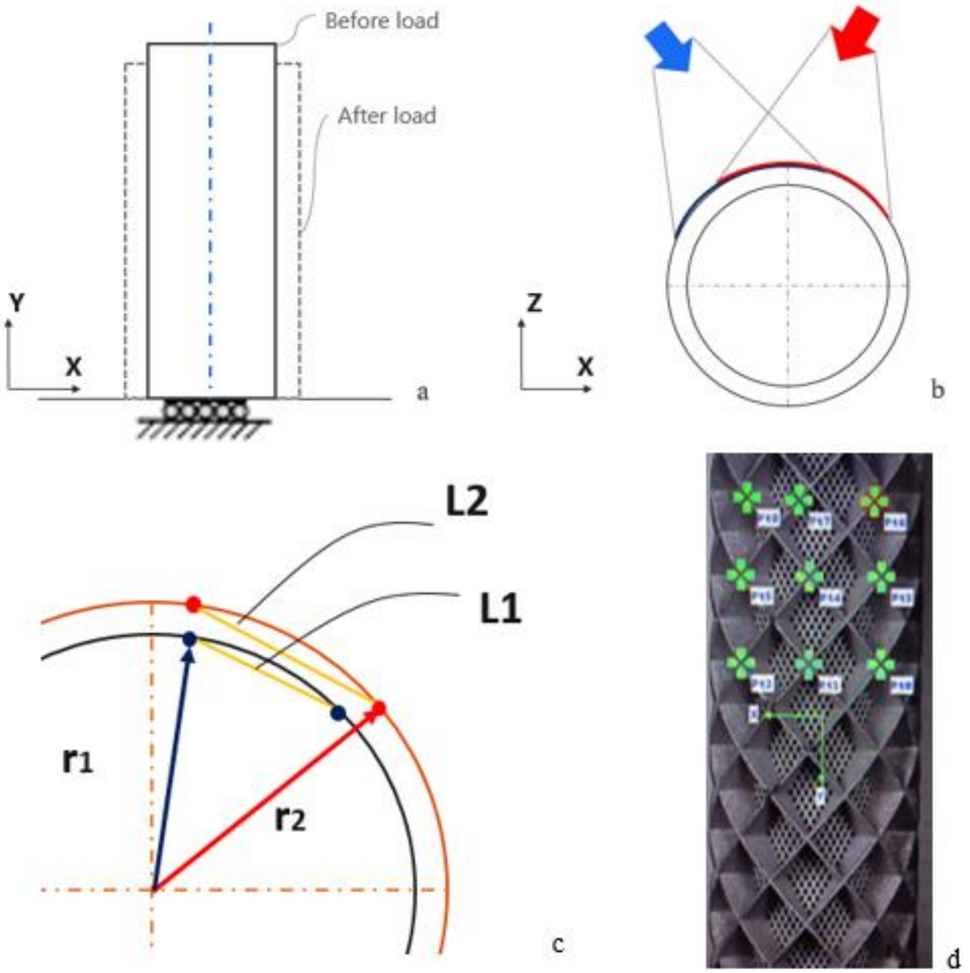

Figure 4.12 Schematic view of the deformation calculation.

$$Li = \sqrt{Xi^2 + Zi^2} \tag{4.1}$$

$$r_2 = r_1 \frac{L_2}{L_1} \tag{4.2}$$

4.3.5 Expansion results

Across all designs, core cell fineness governs radial compliance. According to the measured expansions indicated in Figure 4.13, fine-cell cylinders remain in the single-digit-micrometer range at 8–20 bar (≈3–4 µm at 8 bar; ≈6–8 µm at 20 bar), whereas rough-cell cylinders expand by an order-of-magnitude more at 20 bar (≈30–44 µm), with consistent separation already visible at 8 bar (≈12–15 µm). Within each core family, stiffener variations introduce only second-order shifts—thicker/wider stiffeners and the smaller outer diameter reduce expansion modestly but never overturn the effect of the core.

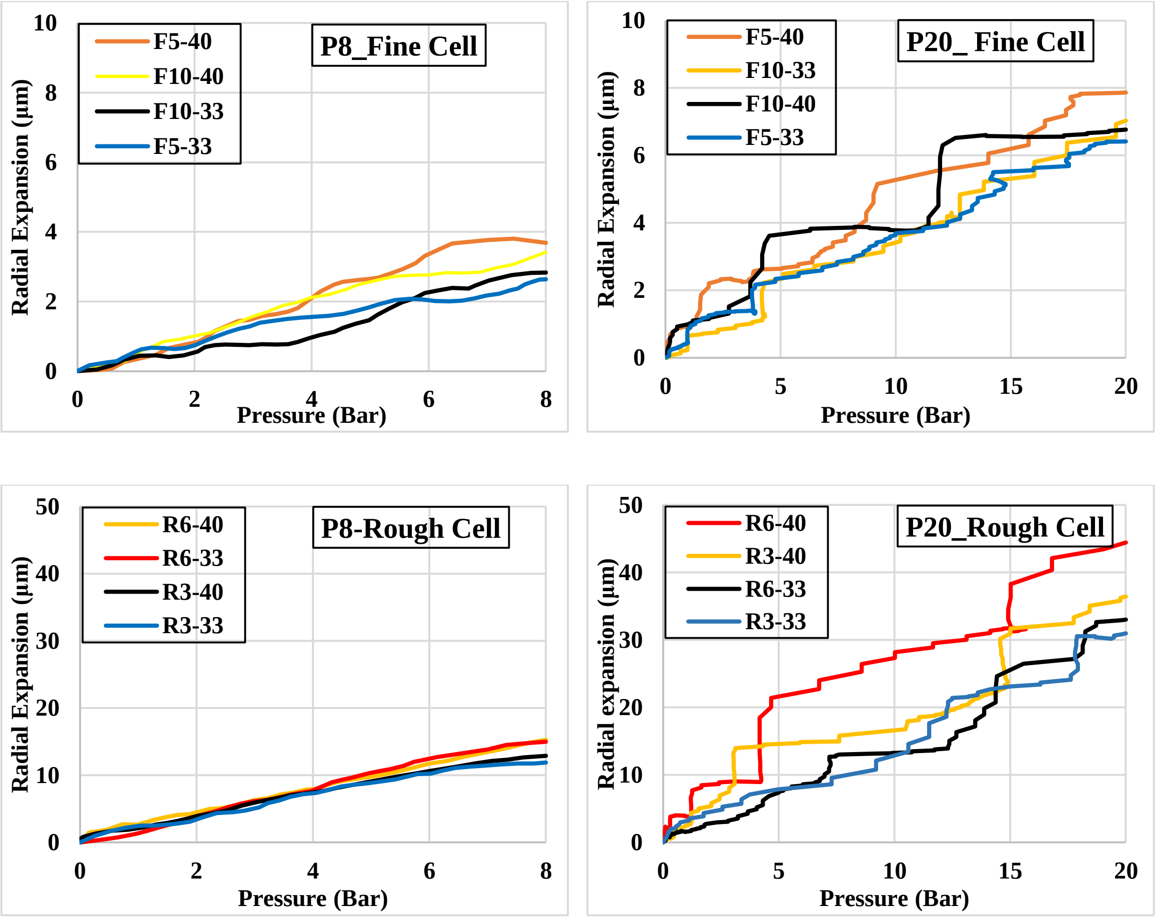

Figure 4.13 Radial expansion according to the applied pressure for all experimental cases.

4.3.6 Compression test of cubes

The structure has a non-homogeneous behavior in three directions. To find out the exact value of directional stiffness and strength, the two target cell nets have been manufactured in the same coordinate system. The compression test specimens have been selected according to ISO_13314 [88], with dimensions of 13 x 13 x 25 mm. The test plan is to apply the load in three directions with 6 specimen repetitions (see Table 4.3). The compression load has been applied with a speed of 0.01 mm/s. The MTS 810 machine with a 250 kN load cell, shown in Figure 4.14, applied the displacement to 5 mm (≈20% global strain) at a crosshead speed of 0.005 mm/s. The DIC system recorded the deformation every 3 s using a Dantec Dynamics Q400 3D DIC system with two 2 MP cameras.

Table 4.3 Experimental test table illustrating the number of tested specimens by cell types and load directions.

Cells	**Fine**			**Rough**		
Direction	1	2	3	1	2	3
Rectangular Cubes	6	6	6	6	6	6

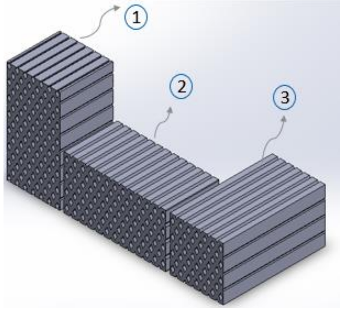

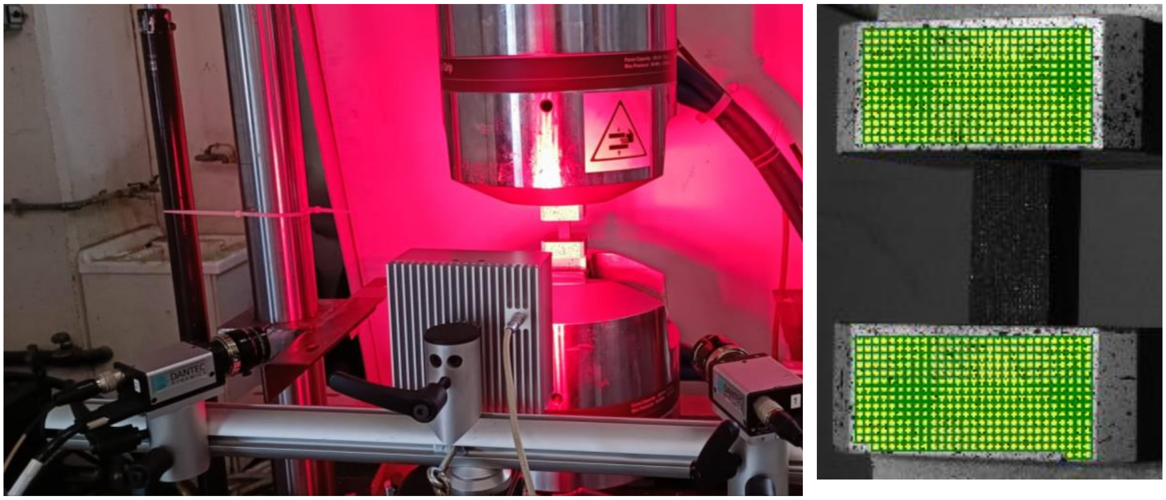

Figure 4.14 Compression test setup for rectangular cube specimens.

4.3.7 Results of compression test on rectangular cube specimens

The target results of these compression tests are the equivalent Young's modulus (Eeq) and yield stress. The equivalent stress (σeq) was determined by dividing the recorded force (F) by the initial cross-sectional area of each specimen. The longitudinal strain (εy) was obtained by dividing the displacement of the loading plate by the initial plate distance. Young's modulus (Eeq) was derived from the stress-strain curve as the slope of the curve in the initial linear elastic region. In Figure 4.15, the 5 mm deformed specimens are shown. In Figure 4.16, the stress-strain curve of the specimens is shown.

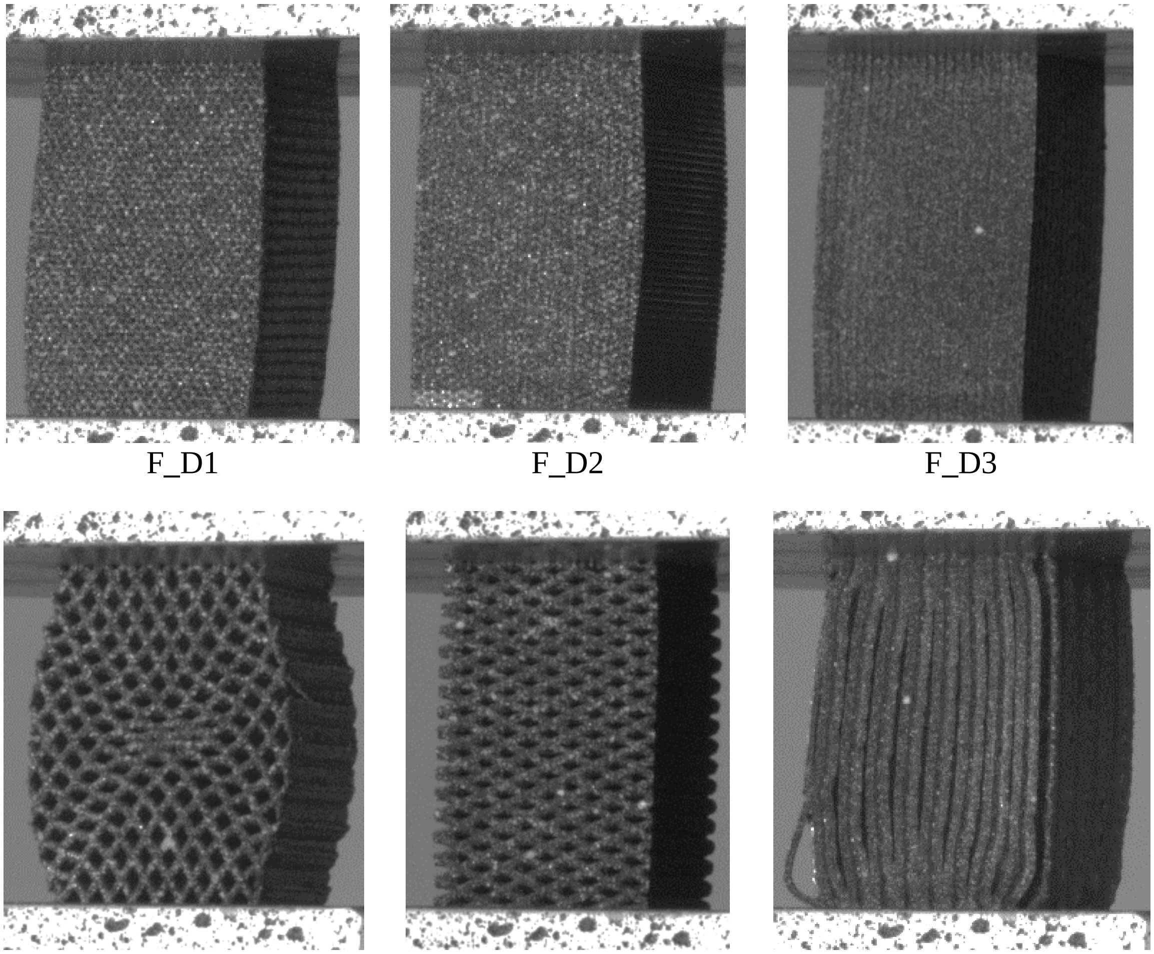

F_D1 F_D2 F_D3

R_D1 R_D2 R_D3

Figure 4.15 Specimens under compression load in 5 mm deformation.

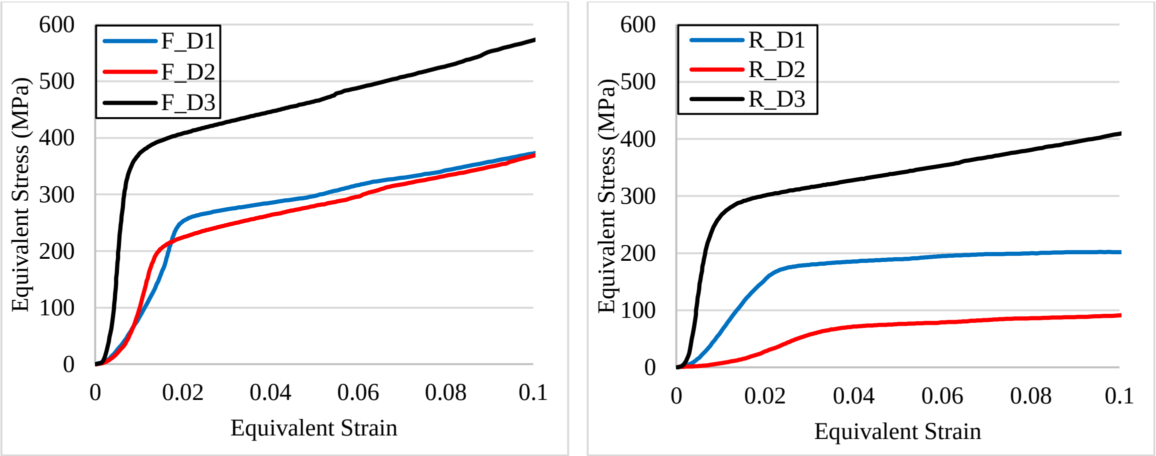

Figure 4.16 Stress-strain curve for rough and fine cell rectangular cubes.

4.4 Numerical method

At the first step, the mechanical properties of SLM-printed 316L stainless steel were required. This material has orthotropic behavior. Therefore, the load direction has been selected for two directions. The specimens were manufactured and tested according to standards DIN 50125 [89], with the neck section of 3 x 8 x 30 mm. The evaluated data were provided by the printing manufacturer (see Figure 4.17). In addition, yield stress, ultimate stress, and fraction strain have been reported as 437 MPa, 555 MPa, and 34% respectively.

The finite element simulations were conducted using ABAQUS 2022. The important results from this test are the elastic modulus in horizontally and vertically printed specimens, which are 169 GPa and 110 GPa, respectively. The Poisson’s ratio is considered 0.28, which is an average value of directional evaluation from experiments conducted in a research [57]. To have nine engineering constants, the shear moduli are calculated according to Equation (4.3). In Table 4.4, the elastic properties considered for simulation are indicated. In addition, the plastic behavior has been extracted from the stress-strain curves shown in Table 4.5.

$$G = \frac{\mathrm{E}}{2(\nu - 1)} \tag{4.3}$$

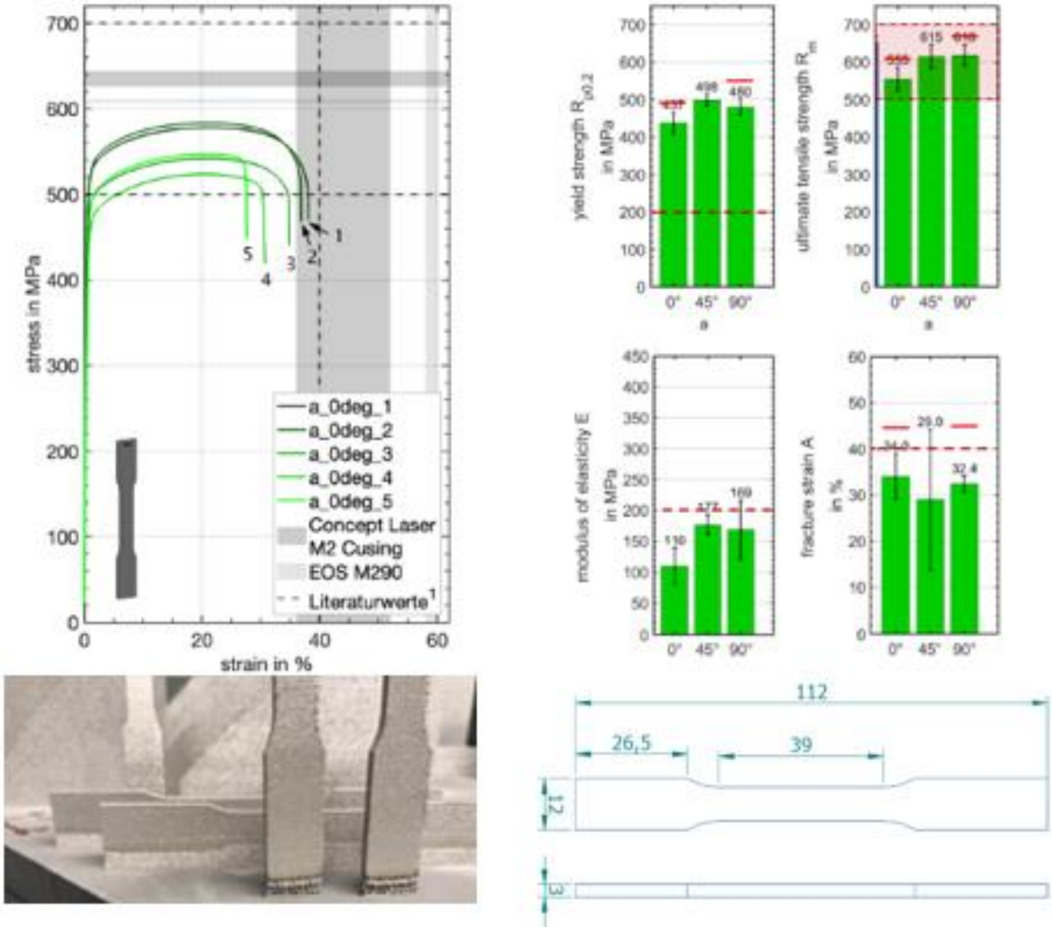

Figure 4.17 Tensile test of SLM printed 316L stainless steel specimens and results.

Table 4.4 Elastic_ orthotropic behavior of SLM printed 316L stainless steel.

Ex	**Ey**	**Ez**	**νxy**	**νyz**	**νxz**	**Gxy**	**Gyz**	**Gxz**
(GPa)	(GPa)	(GPa)				(GPa)	(GPa)	(GPa)
169	110	169	0.28	0.28	0.28	54.5	54.5	66

Table 4.5 Plastic properties for the vertically printed specimens

Strain	0	0.02	0.05	0.2	0.34
Stress (MPa)	437	540	550	580	555

4.4.1 Internal pressure load

The main objective of the simulation of the study is to validate the experimental expansion result and indicate additional aspects. The full-scale model is complex, and it is too big in terms of the number of elements to replicate. Therefore, a section of the cylinder has been modeled. For cases with smaller stiffeners, a quarter circle was modeled to run the simulation. The larger stiffeners had odd cell numbers at the circle; thus, a half model was analyzed. The orthotropic material properties were defined for this model according to Table 4.4 and Table 4.5.

In FEM, when a body from the real condition is removed to ease the analysis, its effect should be made by defining the condition of the surroundings. To have the condition of the complete cylinder, on the neighboring faces, boundary conditions were applied. The sides and lower faces have symmetry BC. For the top face, the reference point that is coupled to the face has restrictions in all DOF, just free to move in the normal direction, and the top face cannot rotate (see Figure 4.18 and Figure 4.19).

- **Left face:** symmetry in Z [U3=0, UR1, UR2=0].
- **Right face:** symmetry in X [U1=0, UR2, UR3=0].
- **Top face:** [UR1, UR2=0].
- **Bottom face:** symmetry in Y [U2=0, UR1, UR3=0].
- **Reference point (RP) :** U2=Free, U1, U3=0, UR1, UR2, UR3=0.
- **Internal face:** Uniform Pressure.

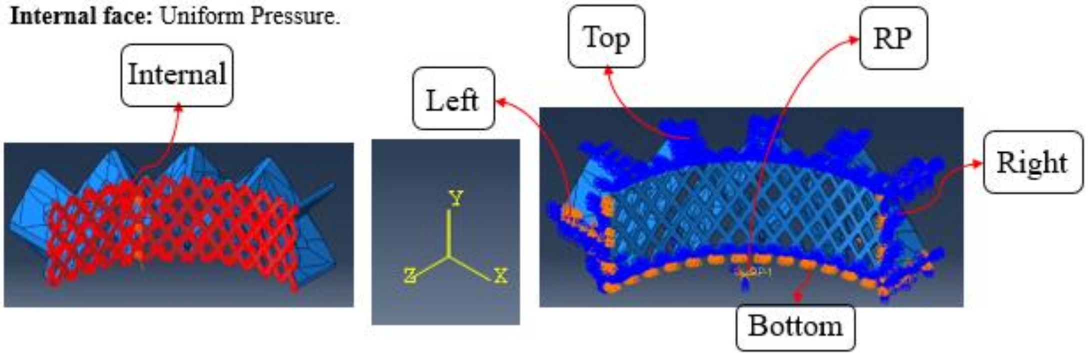

Figure 4.18 Boundary conditions for the quarter-circle section of cylindrical specimens.

- **Side face:** symmetry in Z [U3=0, UR1, UR2=0].
- **Top face:** [UR1, UR2=0].
- **Bottom face:** symmetry in Y [U2=0, UR1, UR3=0].
- **Reference point (RP) :** U2=Free, U1, U3=0, UR1, UR2, UR3=0.
- **Internal face:** Uniform Pressure.
- **One Node:** [U1=0].

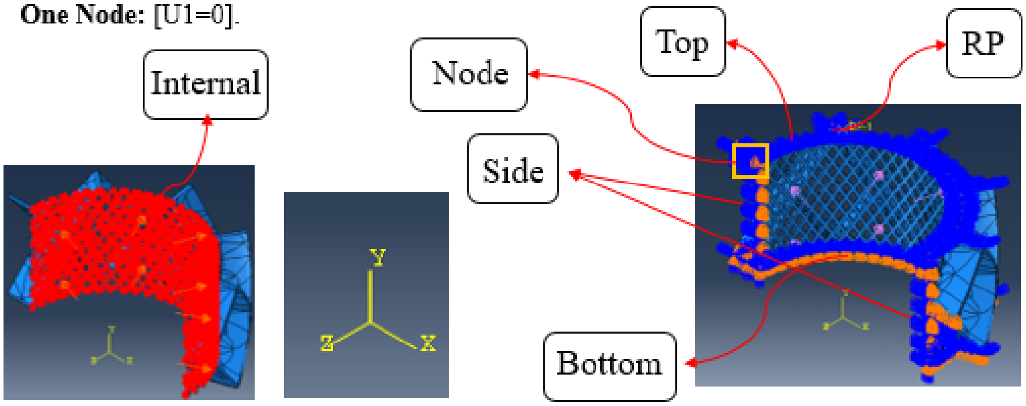

Figure 4.19 Boundary conditions for the half-circle section of cylindrical specimens.

4.4.2 Expansion results

In this section, the expansion of the numerical method is illustrated by presenting the deformation of under-pressured models. In Figure 4.20, a comparative deformation contour under pressure load for 8 cases is shown. The method of calculating the expansion should be clear. In Figure 4.21 (a), the quarter model of the selected section is shown with initial geometry and the large-scale deformed body with the coordinate system. The target is to find the radial expansion. The ring-like model is expanded through radius. Observing the deformation from the top view in the Cartesian system, it can be understood that the maximum deformation in either the x or z axis is equivalent to the radial expansion since these two axes are aligned with the radius (Figure 4.21 (b)). In Figure 4.22, the mean values of the experimental expansion for 8 and 20 bar pressure are shown by comparing with the simulation data for the nominal dimensions. According to this result, the fine and rough cells have a considerable stiffness difference. Moreover, in 20 bars, the mean expansion for rough cell is 36 µm for the experiment and 46 µm for the simulation (28 % higher). On the other hand, these numbers for fine cell are 7 µm for the experiment and 16 µm for the simulation (129 % higher).

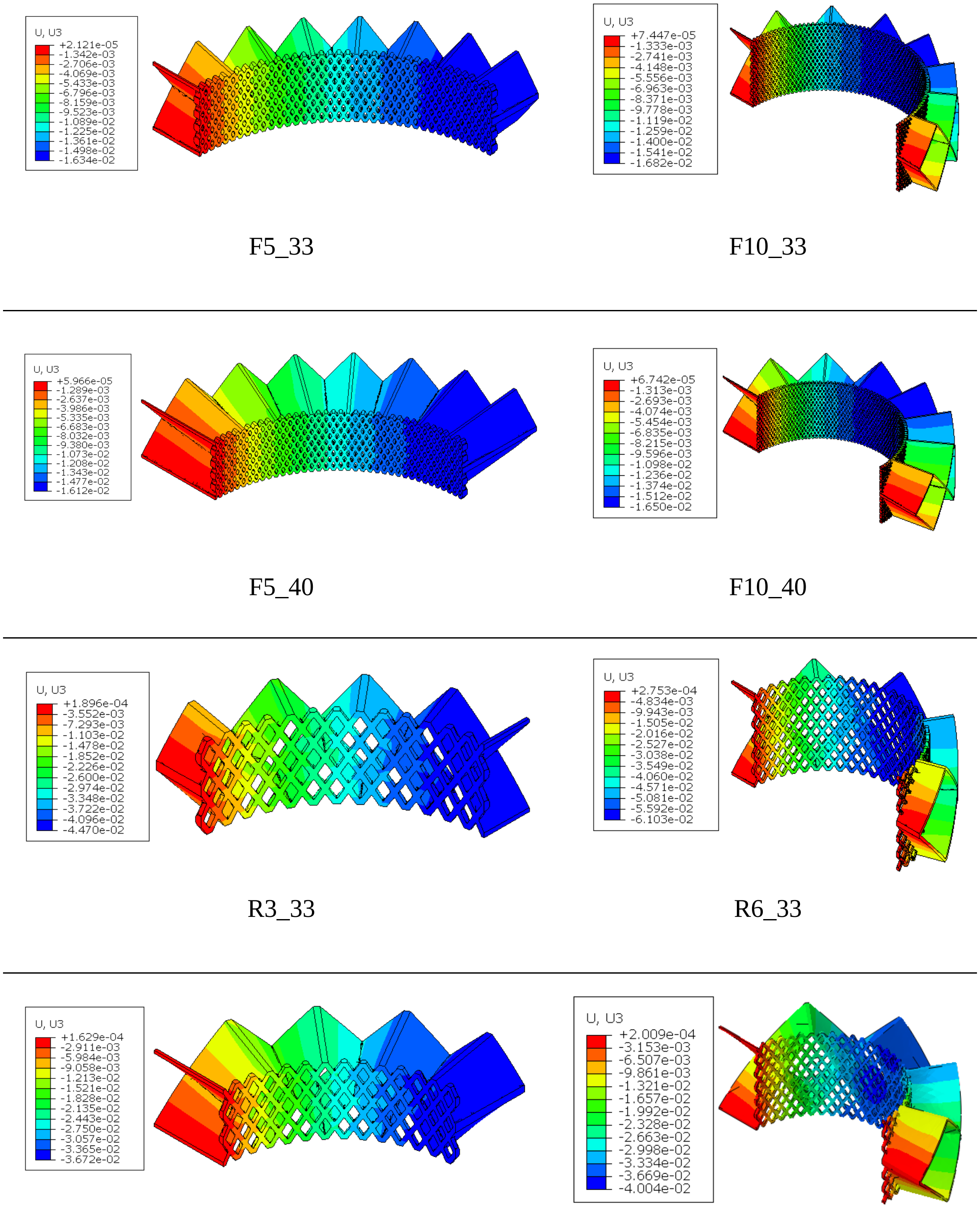

F5_33 F10_33

F5_40 F10_40

R3_33 R6_33

R3_40 R6_40

Figure 4.20 Contour of deformation indicating the radial expansion

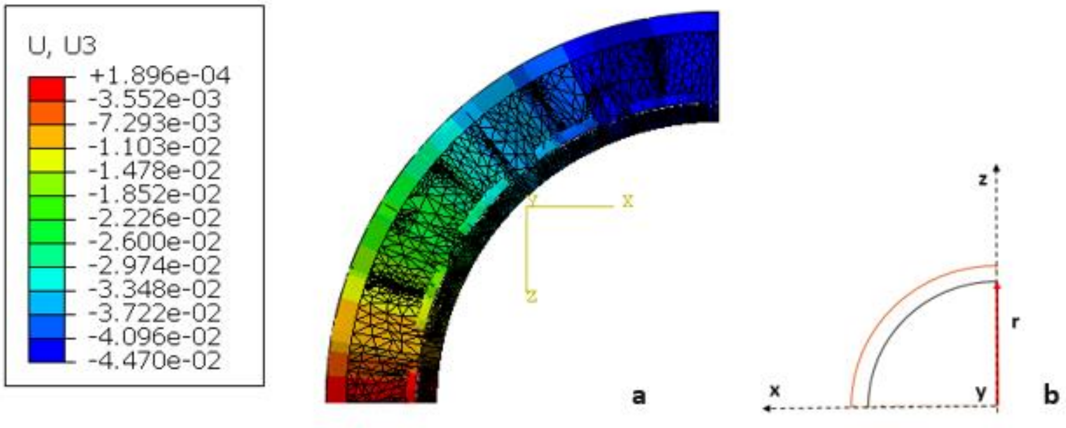

Figure 4.21 Contour of deformation with a large scale factor from the top view (a), and the coordinate system (b).

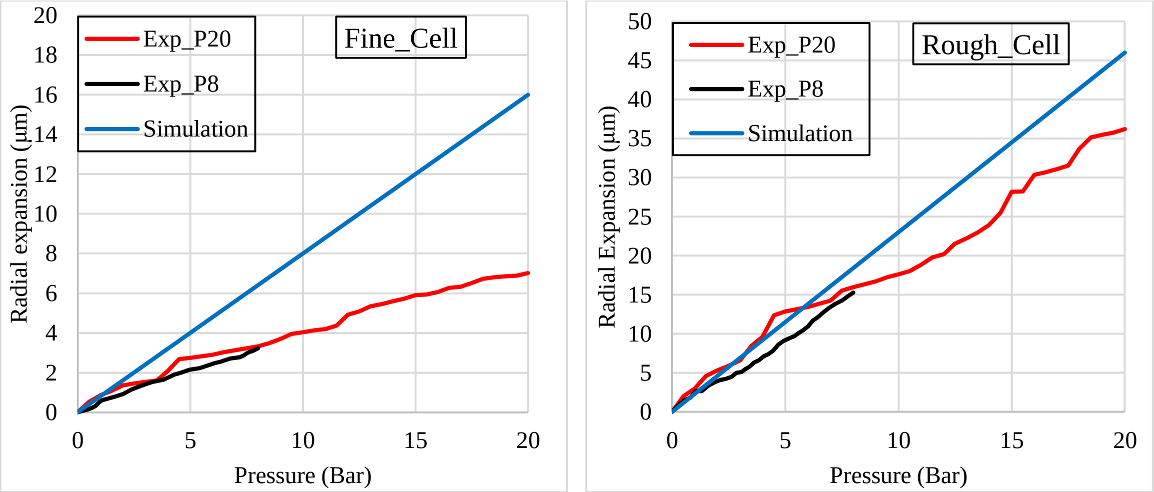

Figure 4.22 The average radial expansion according to the applied pressure for experiment and simulation.

4.4.3 Compression load

This section aims to show what happens internally in the design cells under compression loads in three orthogonal loading directions. The target results for validation are the equivalent Young’s modulus and yield stress of the structure. Performing this simulation, try to validate the experiment and get a correct vision of the structure. The dimensions exactly replicate the nominal geometry of the tested specimens. Isotropic material properties (Young’s modulus 110 GPa, and Poisson’s ratio 0.28) were considered for this simulation, taking the lower value from the tensile test results presented in Table 4.4. In the compression test, for the total model, B.C. is simple. Four surrounding faces are completely free. On one face, a displacement (here 1 mm, which is 4% contraction) is applied. The opposite face should hold the part to encounter the displacement; therefore, it is fixed in the direction that the displacement is applied (see Figure 4.23).

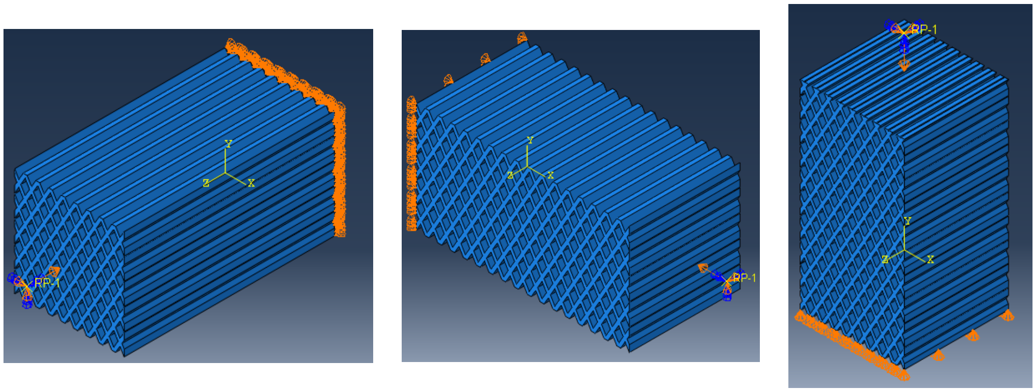

D3 D2 D1

Figure 4.23 Boundary conditions for cubic specimen.

4.4.4 Compression results

The compression test was performed to observe the stiffness and strength of the structure. Across the six test categories, the ordering is consistent in both experiment and simulation: fine cells are stiffer than rough cells, and the directional hierarchy is D3 > D1 > D2. This can be read directly from Figure 4.24, where the D3 curves exhibit the steepest elastic slopes, D1 is intermediate, and D2 is the softest. The FE curves reproduce the shapes up to 40% strain and are compared with the experiment, where in some cases the results are close, and in some cases the differences are too much.

Taken together, Figure 4.24 and Table 4.6 show that the FE model gets the trends right—topology (fine > rough) and direction (D3 > D1 > D2)—and is closest where response is dominated by well-aligned axial paths (R_D3). For other cases, clearly, the geometric imperfections and bending-dominated phenomenon reduce the right trend accuracy. Generally, from the Figure 4.24 and Table 4.6 data, the following points are concluded:

- In comparison to Young’s modulus, the yield stress is calculated with more acceptable results.
- At D1, there is an over-prediction of F_D1 (31%) and R_D1 (74%), which means the experiment gives lower stiffness. The highest under-prediction occurs in F_D2 (−65%), where the simulation has a trend that is closer to the estimated result. Although it is assumed that D1 should have higher stiffness, for fine cells, the experimental results are inverse.
- Looking at the topology of this kind of structure, the effective parameter on the mechanical property is the amount of mass in the section area where the load is applied. In other words, the structure is built of the integrated section areas that include space and mass. If the average value of mass along the structure increases has a direct relation to the stiffness.
- Therefore, the geometric imperfection should be measured to compare with the nominal dimensions used in simulation and real geometry.

Table 4.6 Comparison of experimental and numerical equivalent elastic modulus of the six different rectangular cubes.

		R_D1	**R_D2**	**R_D3**	**F_D1**	**F_D2**	**F_D3**
Experiment	**E (GPa)**	10.3	3.1	58.2	24.4	24.2	90.1
Simulation		17.9	3.3	57.6	35.3	8.5	70.7
Error (%)		74%	6%	-1%	31%	-65%	-22%
Experiment	**σy (MPa)**	159.2	62.8	364.6	263.4	215.4	369.2
Simulation		98.1	41.2	336.1	185.3	80.6	311.2
Error (%)		-38%	-34%	-8%	-30%	-63%	-16%

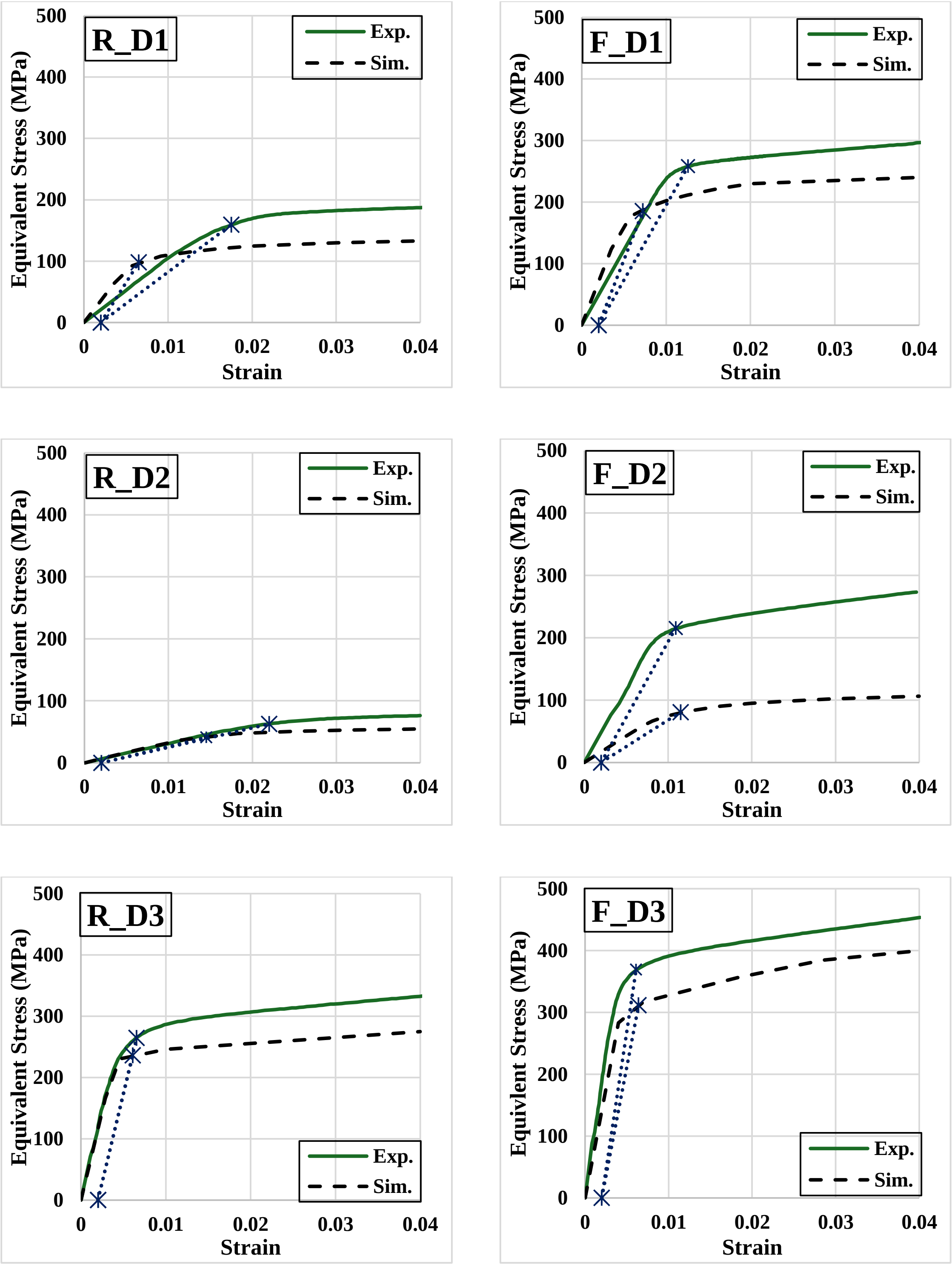

Figure 4.24 Stress – strain curves to compare experiment and simulation of rectangular cubes.

4.4.5 Microscopic images from the tested specimens

Observing the difference between experimental and numerical results, it was made to see that how much geometric imperfections exist in 3D printing. After taking the measurement, several reasons to justify the results of the simulation have been found. The tested rectangular cube specimens (RC) and cylindrical lattices were measured and reported the dimensions. A measurable quantity was the cell thickness, which, according to the data in Table 4.7, for fine cells, the real geometry is 40% to 60% thicker, and for the rough cells is 30% to 37%. This data and more perspectives are illustrated in Figure 4.25, Figure 4.26, and Figure 4.27. The more the cell gets thicker, the less space remains for the perforation or the cell width. In addition, the quantitative difference between fine and rough cells indicates that in fine cells, the difference or error between experimental stiffness and strength should be higher than in simulation. Furthermore, the shape of the perforation in fine cells is not equal and contains flaws. Each cell has a unique shape, and the curves and fillets have come together to make a completely different structure from the expected shape. These differences, alongside of resulting higher mechanical response, reduce the difference between D1 and D2. As a result, in the experiment, it can be observed that the stress-strain curves for F_D1 and F_D2 are close.

Table 4.7 Comparing cell thickness from the microscopic measurement and real dimensions.

	Nominal dimension (mm)	**Real dimension (mm)**	**Error %**
RC_ fine cell	0.2	0.28	40
RC_ rough cell	0.4	0.55	37
Cylinder_ fine cell	0.2	0.32	60
Cylinder_ rough cell	0.4	0.52	30

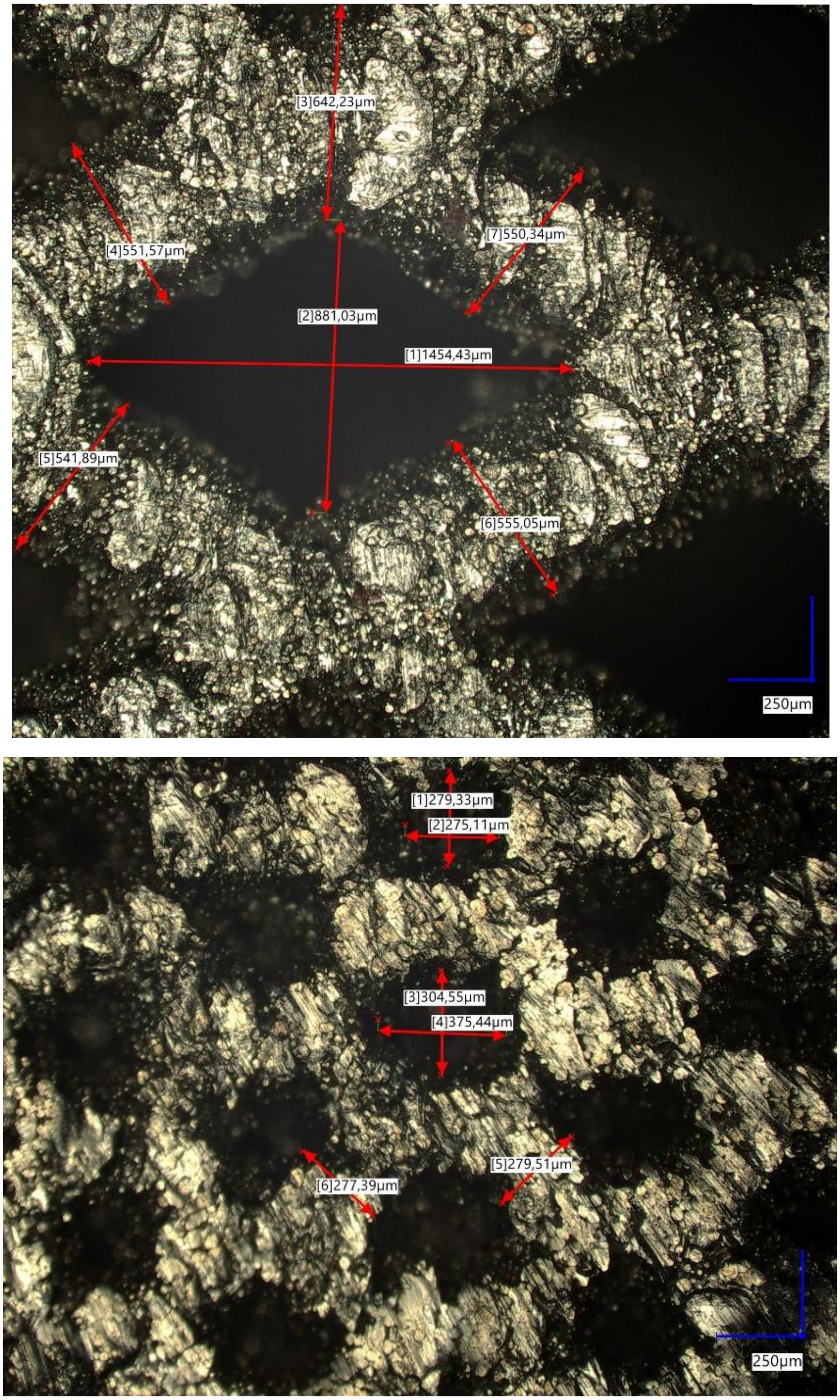
Rough cell

Fine cell

Figure 4.25 Microscopic images from the tested RC specimens.

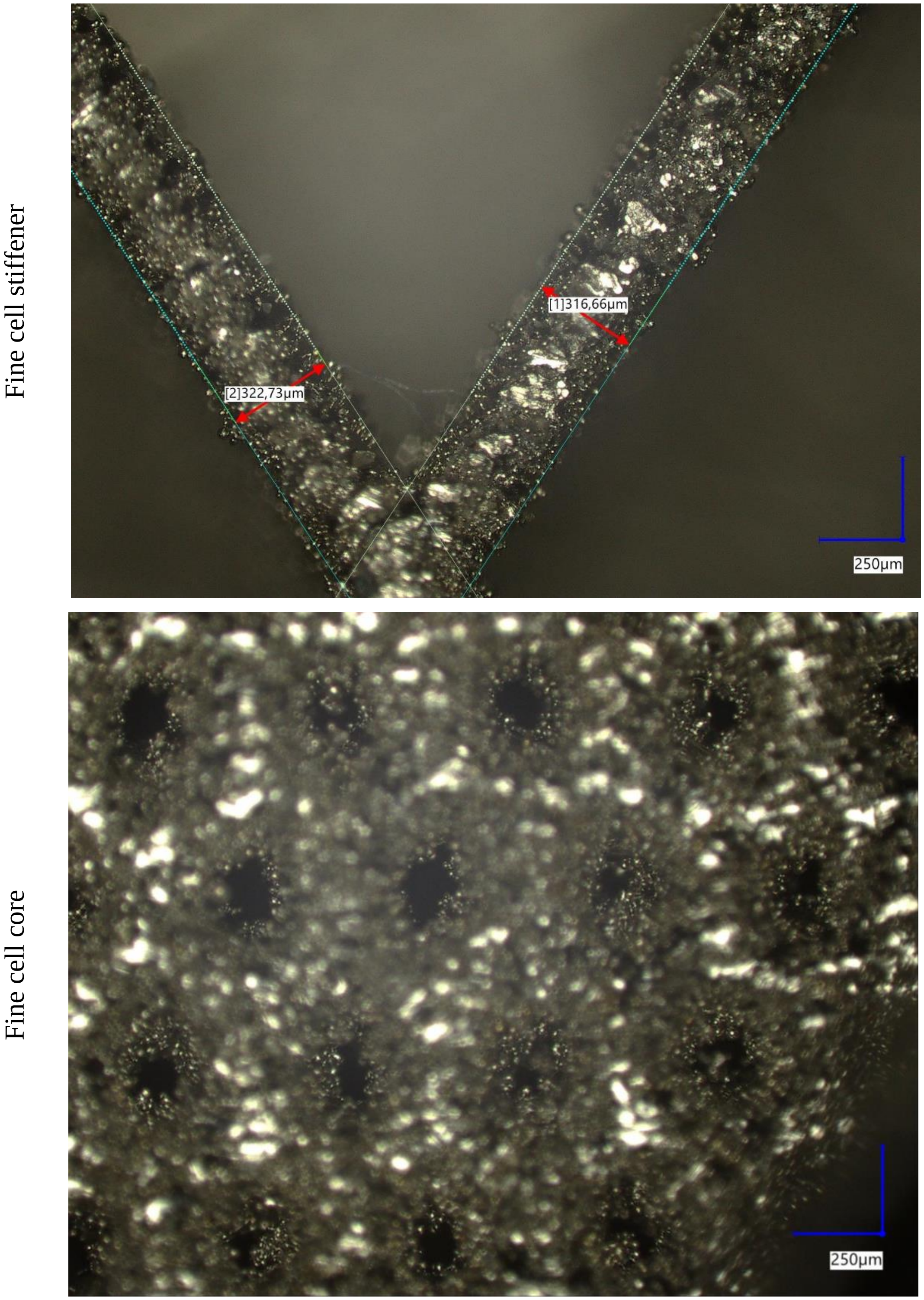

Figure 4.26 Microscopic images from the tested cylindrical specimens (fine cells).

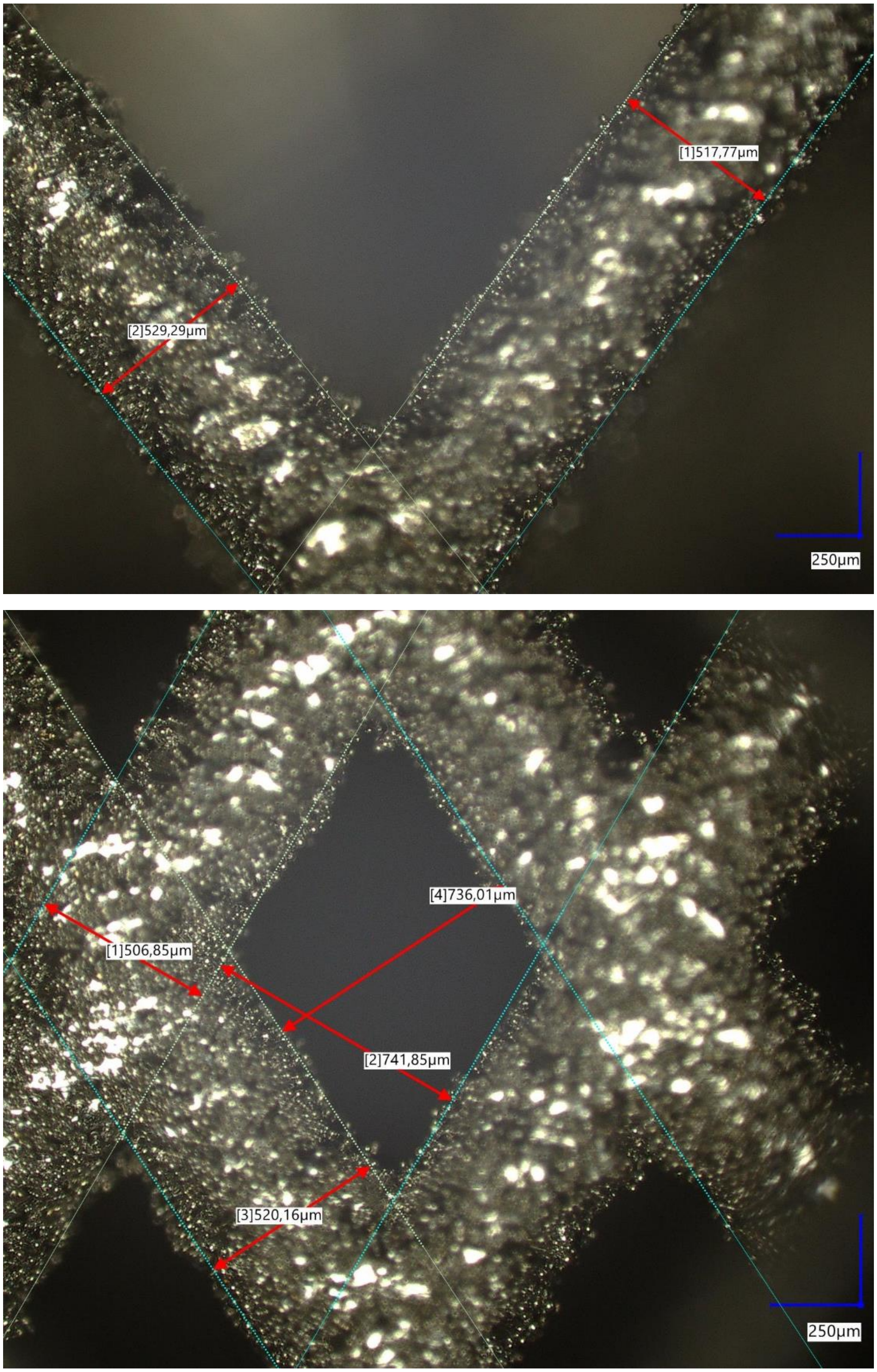

Figure 4.27 Microscopic images from the tested cylindrical specimens (rough cells).

4.4.6 Stress distribution in cylinders

The experimental expansion performed in this chapter was non-destructive and without failure. The measurable parameter to compare with the simulation was expansion. However, the simulation can show the stress distribution, which is insightful and helps to better understand what happens inside the structures under load before they fail.

Figure 4.29 (fine cells) shows the stress concentration in the critical region (the corner of perforations) while the entire structure has low stress. For rough cells (Figure 4.29) correspondingly the stress concentration in sharp corners is more than in the other regions. This means that although local plastic behavior happens under this pressure, it is not too much to cause complete failure. Additionally, in terms of comparison, the stress level in the rough cell is higher, which is in agreement with higher expansion. Another point is that low stress in stiffeners, which proves the fact that the core dense part is the effective section of the cylinder.

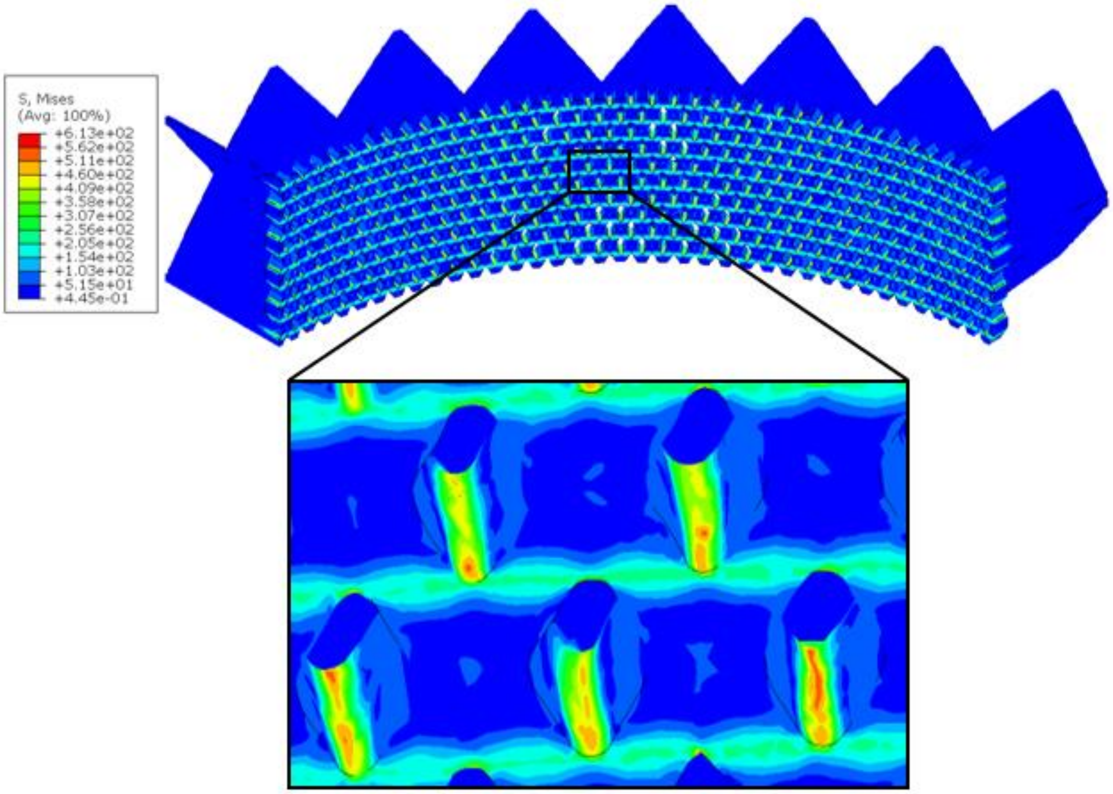

Figure 4.28 Stress distribution contours in cylindrical model for fine cells.

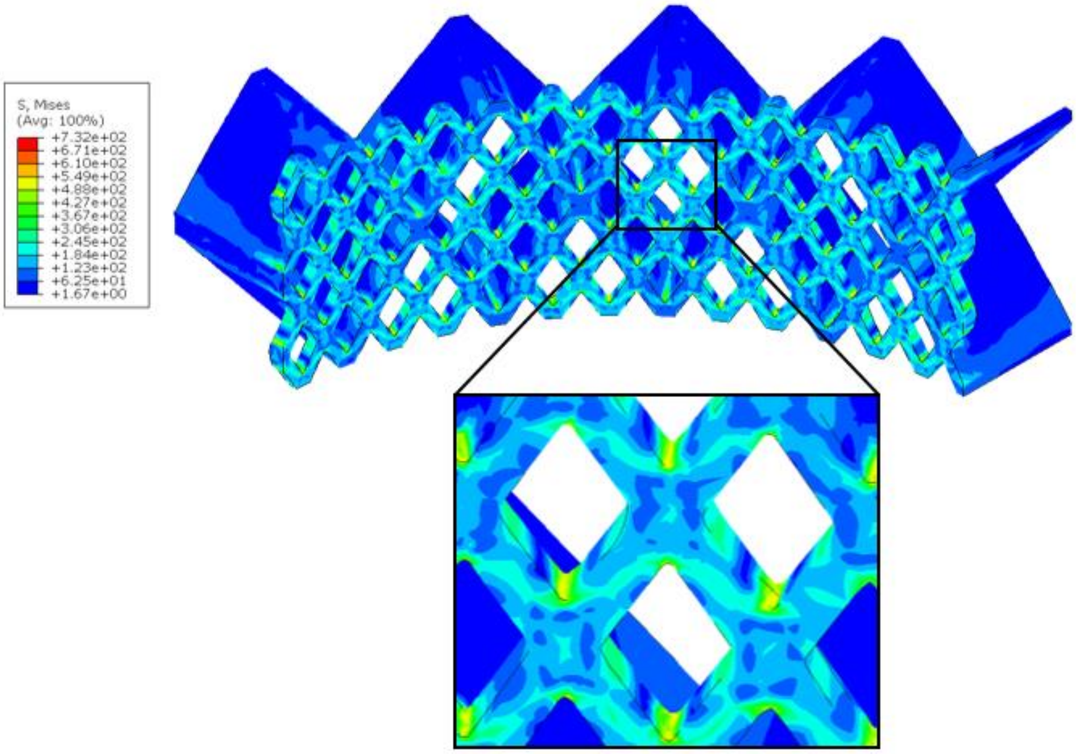

Figure 4.29 Stress distribution contours in cylindrical model for rough cells.

4.4.7 Global vs local stress

Architected structures under loads have two levels of stress/strain. The first is the global stress-strain curve, which is a result of total force and displacement, considering the specimens as a homogeneous bulk material. The second is the local stress-strain curve, which is the values that are detected in elements. The von Mises stress in each increment corresponding to the global strain makes this curve. The stress contour for the RC model is different than the cylindrical model. As shown in Figure 4.30, except for the side open cells in some cases, for this model, the stress is normally distributed. However, this stress is not the global stress, which is calculated by the (Stress = Force/ Section Area) formulation. The so-called local stress observed in Figure 4.30 is compared with the global stress, and they are shown in Figure 4.31. The idea to indicate the stress level is to see how close the model is to the failure point. The mean stress measured in elements (with the highest stress and yellow or red color in stress contour), shown in Figure 4.28 and Figure 4.29, is for fine cells, 387 MPa, and for rough cells, 473 MPa, while in most of the model (with blue color in stress contour), the stress is very low in comparison. These values are adjusted to the stress-strain curve for each load direction to give a perspective that although at some point in the cylinder the stress is too large, in the total structure in under lower stress. It is worth mentioning that, according to the microscopic images presented before, the real structures are stronger than the simulation model. As a result, in real geometry, the dashed lines represent the stress level would shift to the left and a safer mode.

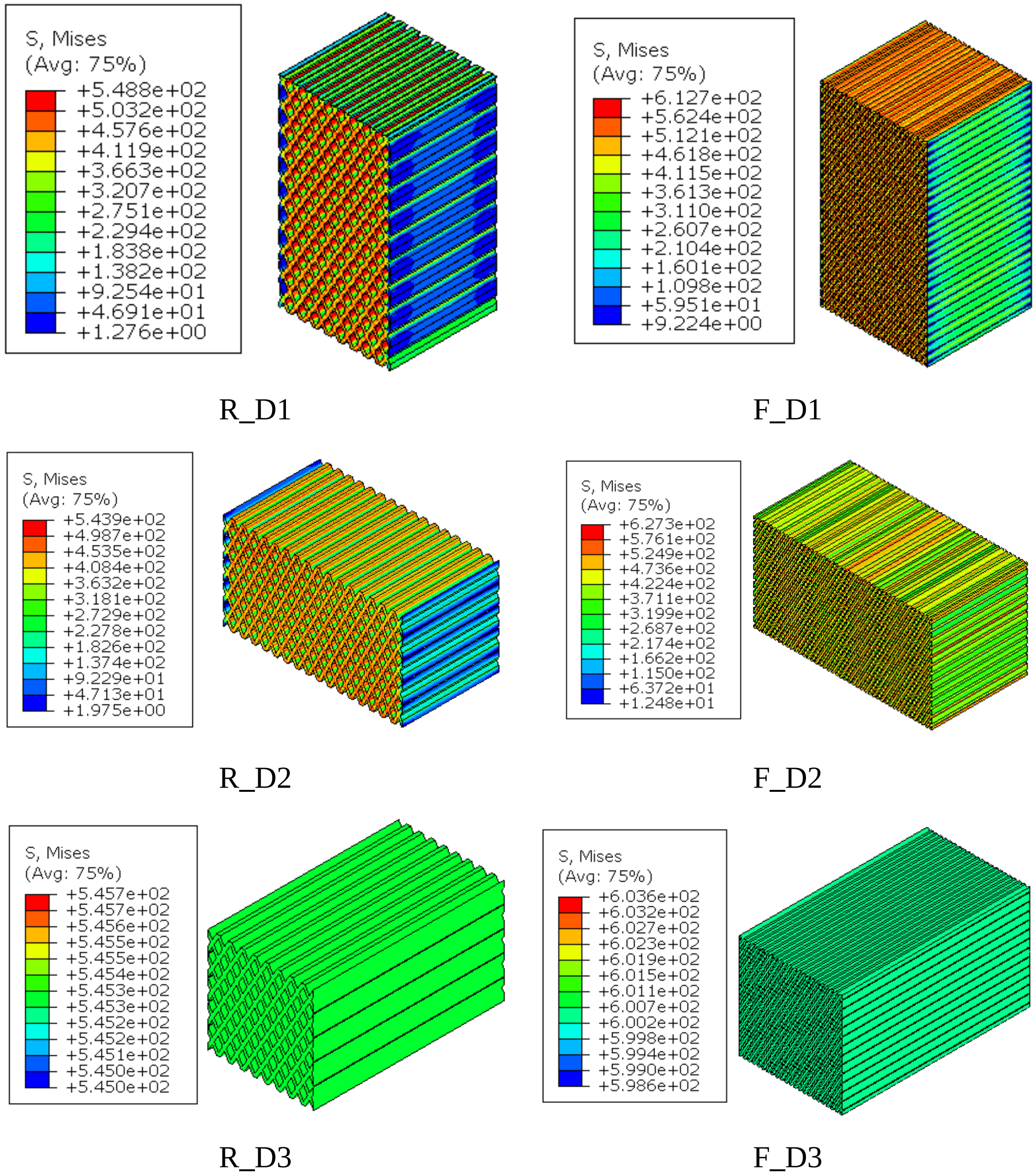

Figure 4.30 Stress contour for three load directions for fine and rough cells.

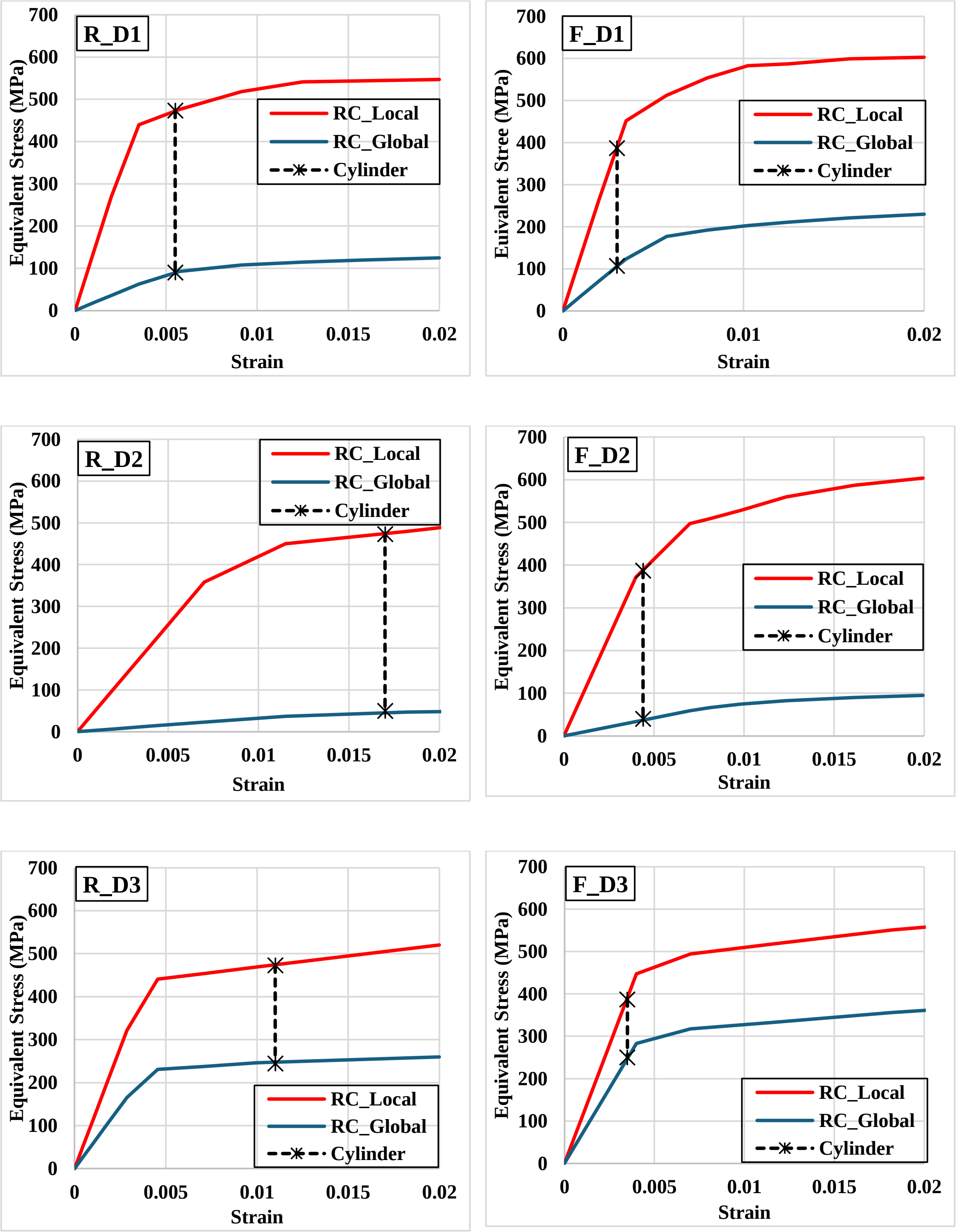

Figure 4.31 Stress – strain curves to compare numerical global and local stress levels.

4.5 Conclusions

This chapter established and validated a design–test–simulate workflow for cylindrical SLM lattices under internal pressure. By systematically varying core cell size (fine vs rough), stiffener geometry width, and outer diameter. The main finding is simple and actionable:

- The dense core cells are the dominant parameter—fine cells hold diameter growth to single-digit micrometers even at 20 bar—while stiffeners provide secondary, incremental gains that do not flip the overall ranking.
- The DIC-based measurement of radial expansion shaped clean expansion histories in both pneumatic (smooth ramp) and hydrostatic (stepwise) tests. Using the FE model, tried to reproduce these micrometer-scale trends across all eight designs to validate the result and observe the stress level.
- Complementary compression tests on rectangular cubes produced by the same cell size (fine and rough) lattices confirmed higher stiffness for fine cells and provided a second validation target. The simulation captured the stiffness ordering and clarified global vs local stress development, offering a rational basis for safety factors.
- Microscopic images revealed the reason for the difference between experiment and simulation. It has been shown that, especially in small cells, diamond shapes turn into a square shape and reduce the different mechanical behavior in the build plate. Additionally, the fillet and imperfections show that the printed parts are usually thicker than the designed version, which may cause an increase in mechanical properties.

Overall Conclusions and future perspective

In this thesis, the mechanical behavior—mainly elastic response—of the AM lightweight cellular architectures was studied under different loading conditions, and it governs stiffness, strength, and deformation when the weight ratio is a key constraint. The key conclusions are:

- For FDM grid infills, elastic response is anisotropic and varies systematically with infill ratio and raster angle. Between 20–80% IR, the build-up direction (E3) exceeded in-plane moduli (E1, E2), while at 100% IR, the trend inverted, with E1, E2 > E3 due to road alignment and load-path continuity in-plane.
- On the modeling side, three different models were compared for FDM cubes: shell (SHL), nominal solid (SLD), and a non-uniform section (NUS) calibrated to microscopy. This method gave 13% to 19% accuracy in the prediction of experimental results. On the other hand, with the RVU method using the PBC-based homogenization workflow, the precision reached 8%. The latter method not only increases the accuracy of prediction but also indicates the layer-wise essence of FDM products.
- For SLM 316L lattices, cylindrical hybrids with fine/rough cell regions and light cell stiffeners were designed and tested. The setup enabled stable pneumatic 8 bar and hydrostatic loading up to 20 bar with DIC-based micrometric expansion tracking.
- Experiments and simulations agreed on the ordering of radial expansion across the eight geometries. The fine-cell designs were consistently stiffer in the hoop direction than rough-cell counterparts at equal pressure. In addition, von Mises fields highlighted benign, localized stress concentrations at perforation corners without global yielding at the applied loads.

In conclusion, the thesis delivers two effective experimental and computational works to design cellular structures by weight. By unifying directional testing, defect-aware modeling, and application-level loading (compression for polymers, internal pressure for metals), it turns infill pattern/density and lattice fineness/stiffeners into quantitative obstacles that can be set early in design with confidence.

Future perspectives for the presented study can be laid down in several areas. First, extending the framework to nonlinearity and damage evaluation and calibrated elasto-plasticity to failure predictions, not just elastic moduli. Second, regarding the durability and loading spectrum, which involves performing cyclic and rate effects (creep/fatigue) for lattice structures. Finally, performing homogenization methods on more complex structures, such as stochastic structures.

References

[1] D. Syrlybayev, B. Zharylkassyn, A. Seisekulova, M. Akhmetov, A. Perveen, D. Talamona, Optimisation of strength properties of FDM printed parts—A critical review, Polymers 13(10) (2021) 1587.

[2] J. Mogan, W. Harun, K. Kadirgama, D. Ramasamy, F. Foudzi, A. Sulong, F. Tarlochan, F. Ahmad, Fused deposition modelling of polymer composite: a progress, Polymers 15(1) (2022) 28.

[3] T.J. Gordelier, P.R. Thies, L. Turner, L. Johanning, Optimising the FDM additive manufacturing process to achieve maximum tensile strength: a state-of-the-art review, Rapid Prototyping Journal 25(6) (2019) 953-971.

[4] E. Monaldo, M. Ricci, S. Marfia, Mechanical properties of 3D printed polylactic acid elements: Experimental and numerical insights, Mechanics of Materials 177 (2023) 104551.

[5] M. Bragaglia, F. Cecchini, L. Paleari, M. Ferrara, M. Rinaldi, F. Nanni, Modeling the fracture behavior of 3D-printed PLA as a laminate composite: Influence of printing parameters on failure and mechanical properties, Composite Structures 322 (2023) 117379.

[6] S. Brischetto, R. Torre, Tensile and compressive behavior in the experimental tests for PLA specimens produced via fused deposition modelling technique, Journal of Composites Science 4(3) (2020) 140.

[7] R. Torre, S. Brischetto, I.R. Dipietro, Buckling developed in 3D printed PLA cuboidal samples under compression: Analytical, numerical and experimental investigations, Additive Manufacturing 38 (2021) 101790.

[8] C. Abeykoon, P. Sri-Amphorn, A. Fernando, Optimization of fused deposition modeling parameters for improved PLA and ABS 3D printed structures, International Journal of Lightweight Materials and Manufacture 3(3) (2020) 284-297.

[9] J. John, D. Devjani, S. Ali, S. Abdallah, S. Pervaiz, Optimization of 3D printed polylactic acid structures with different infill patterns using Taguchi-grey relational analysis, Advanced Industrial and Engineering Polymer Research 6(1) (2023) 62-78.

[10] S. Nigam, P. Ahirwar, A comparative study on the effect of infill density, shape structure, and materials on tensile properties of FDM printed components, Materials Today: Proceedings (2023).

[11] S.S. Ambati, R. Ambatipudi, Effect of infill density and infill pattern on the mechanical properties of 3D printed PLA parts, Materials Today: Proceedings 64 (2022) 804-807.

[12] A.P. Agrawal, V. Kumar, J. Kumar, P. Paramasivam, S. Dhanasekaran, L. Prasad, An investigation of combined effect of infill pattern, density, and layer thickness on mechanical properties of 3D printed ABS by fused filament fabrication, Heliyon 9(6) (2023).

[13] C.-H. Liu, P.-T. Hung, Effect of the infill density on the performance of a 3D-printed compliant finger, Materials & Design 223 (2022) 111203.

[14] V. Akhil, S. Aravind, R. Kiran, S. SP, S. Mohan, Experimental investigations on the effect of infill patterns on PLA for structural applications, Materials Today: Proceedings 76 (2023) 636-639.
[15] J.J. Fekiač, L. Kakošová, M. Krbata, M. Kohutiar, M. Eckert, Z. Studeny, A. Dubec, Influence of Infill Geometry and Density on the Mechanical Properties of 3D-Printed Polylactic Acid Structure, Journal of Manufacturing and Materials Processing 9(4) (2025) 134.
[16] H. Al Khawaja, H. Alabdouli, H. Alqaydi, A. Mansour, W. Ahmed, H. Al Jassmi, Investigating the mechanical properties of 3D printed components, Proceedings of the 2020 Advances in Science and Engineering Technology International Conferences (ASET), 2020, pp. 1-7.
[17] S. Rodríguez-Reyna, C. Mata, J.H. Díaz-Aguilera, H.R. Acevedo-Parra, F. Tapia, Mechanical properties optimization for PLA, ABS and Nylon+ CF manufactured by 3D FDM printing, Materials Today Communications 33 (2022) 104774.
[18] M.A. Muflikhun, D.A. Sentanu, Characteristics and performance of carabiner remodeling using 3D printing with graded filler and different orientation methods, Engineering Failure Analysis 130 (2021) 105795.
[19] A.S. Karad, P.D. Sonawwanay, M. Naik, D. Thakur, Experimental study of effect of infill density on tensile and flexural strength of 3D printed parts, Journal of Engineering and Applied Science 70(1) (2023) 104.
[20] B. Pernet, J.K. Nagel, H. Zhang, Compressive strength assessment of 3D printing infill patterns, Procedia CiRP 105 (2022) 682-687.
[21] D. Abbot, D. Kallon, C. Anghel, P. Dube, Finite element analysis of 3D printed model via compression tests, Procedia Manufacturing 35 (2019) 164-173.
[22] S. Tabacu, C. Ducu, Numerical investigations of 3D printed structures under compressive loads using damage and fracture criterion: Experiments, parameter identification, and validation, Extreme Mechanics Letters 39 (2020) 100775.
[23] M.Ö. Öteyaka, F.H. Çakir, M.A. Sofuoğlu, Effect of infill pattern and ratio on the flexural and vibration damping characteristics of FDM printed PLA specimens, Materials Today Communications 33 (2022) 104912.
[24] R. Srinivasan, K.N. Kumar, A.J. Ibrahim, K. Anandu, R. Gurudhevan, Impact of fused deposition process parameter (infill pattern) on the strength of PETG part, Materials Today: Proceedings 27 (2020) 1801-1805.
[25] A. Forés-Garriga, G. Gómez-Gras, M.A. Pérez, Mechanical performance of additively manufactured lightweight cellular solids: Influence of cell pattern and relative density on the printing time and compression behavior, Materials & Design 215 (2022) 110474.
[26] M.T. Birosz, M. Andó, Effect of infill pattern scaling on mechanical properties of FDM-printed PLA specimens, Progress in additive manufacturing 9(4) (2024) 875-883.
[27] N. Dialami, M. Chiumenti, M. Cervera, U. Chasco, G. Reyes-Pozo, M.A. Pérez, A hybrid numerical-experimental strategy for predicting mechanical response of components manufactured via FFF, Composite Structures 298 (2022) 115998.
[28] J. Cañero-Nieto, R. Campo-Campo, I. Díaz-Bolaño, E. Ariza-Echeverri, C. Deluque-Toro, J. Solano-Martos, Infill pattern strategy impact on the cross-sectional area at gauge length of material extrusion 3D printed polylactic acid parts, Journal of Intelligent Manufacturing (2025) 1-22.

[29] T.W. Kerekes, H. Lim, W.Y. Joe, G.J. Yun, Characterization of process–deformation/damage property relationship of fused deposition modeling (FDM) 3D-printed specimens, Additive Manufacturing 25 (2019) 532-544.

[30] A. Al Rashid, M. Koç, Experimental validation of numerical model for thermomechanical performance of material extrusion additive manufacturing process: Effect of infill design & density, Results in Engineering 17 (2023) 100860.

[31] E. Provaggi, C. Capelli, B. Rahmani, G. Burriesci, D.M. Kalaskar, 3D printing assisted finite element analysis for optimising the manufacturing parameters of a lumbar fusion cage, Materials & Design 163 (2019) 107540.

[32] G. Alaimo, S. Marconi, L. Costato, F. Auricchio, Influence of meso-structure and chemical composition on FDM 3D-printed parts, Composites Part B: Engineering 113 (2017) 371-380.

[33] Y. Tao, F. Kong, Z. Li, J. Zhang, X. Zhao, Q. Yin, D. Xing, P. Li, A review on voids of 3D printed parts by fused filament fabrication, Journal of Materials Research and Technology 15 (2021) 4860-4879.

[34] M. Spahic, N. Di Cesare, A. Le Duigou, V. Keryvin, Multi-scale analysis of the flexural behaviour of 3D printed cellular polymer materials: Comparison between morphing and sandwich beams, Composite Structures 273 (2021) 114249.

[35] R. Spina, B. Cavalcante, S. Di Rosa, G. Morandina, A. Mellone, Multiscale modelling of additive tensile test specimens, Procedia CIRP 118 (2023) 777-780.

[36] E. Monaldo, S. Marfia, Multiscale technique for the analysis of 3D-printed materials, International Journal of Solids and Structures 232 (2021) 111173.

[37] P. Parnian, M. Shojaee, O. Weeger, A. D'Amore, Multiscale modelling and characterisation of fused filament fabricated neat and graphene nanoplatelet reinforced G-polymers, Progress in Additive Manufacturing 10(4) (2025) 2861-2876.

[38] S. Garzon-Hernandez, D. Garcia-Gonzalez, A. Jérusalem, A. Arias, Design of FDM 3D printed polymers: An experimental-modelling methodology for the prediction of mechanical properties, Materials & Design 188 (2020) 108414.

[39] M. Somireddy, C. Singh, A. Czekanski, Analysis of the material behavior of 3D printed laminates via FFF, Experimental Mechanics 59(6) (2019) 871-881.

[40] M. Anoop, P. Senthil, Microscale representative volume element based numerical analysis on mechanical properties of fused deposition modelling components, Materials Today: Proceedings 39 (2021) 563-571.

[41] A. Corvi, L. Collini, Combined rve-cohesive elements approach to the multi-scale modelling of fdm 3d-printed components, Theoretical and Applied Fracture Mechanics 128 (2023) 104140.

[42] M. Somireddy, A. Czekanski, C.V. Singh, Development of constitutive material model of 3D printed structure via FDM, Materials Today Communications 15 (2018) 143-152.

[43] M. Somireddy, A. Czekanski, Computational modeling of constitutive behaviour of 3D printed composite structures, Journal of Materials Research and Technology 11 (2021) 1710-1718.

[44] A. Özen, D. Auhl, Modeling of the mechanical properties of fused deposition modeling (FDM) printed fiber reinforced thermoplastic composites by asymptotic homogenization, Composites and Advanced Materials 31 (2022) 26349833221132296.

[45] I.M. Alarifi, Mechanical properties and numerical simulation of FDM 3D printed PETG/carbon composite unit structures, journal of materials research and technology 23 (2023) 656-669.

[46] E. Polyzos, D. Van Hemelrijck, L. Pyl, Numerical modelling of the elastic properties of 3D-printed specimens of thermoplastic matrix reinforced with continuous fibres, Composites Part B: Engineering 211 (2021) 108671.

[47] E. Polyzos, D. Van Hemelrijck, L. Pyl, Modeling elastic properties of 3D printed composites using real fibers, International Journal of Mechanical Sciences 232 (2022) 107581.

[48] S. Atatreh, M.S. Alyammahi, H. Vasilyan, T. Alkindi, R.A. Susantyoko, Evaluation of the infill design on the tensile properties of metal parts produced by fused filament fabrication, Results in Engineering 17 (2023) 100954.

[49] C.Y. Yap, C.K. Chua, Z.L. Dong, Z.H. Liu, D.Q. Zhang, L.E. Loh, S.L. Sing, Review of selective laser melting: Materials and applications, Applied physics reviews 2(4) (2015).

[50] A. Nazir, A.B. Arshad, S.-C. Lin, J.-Y. Jeng, Mechanical performance of lightweight-designed honeycomb structures fabricated using multijet fusion additive manufacturing technology, 3D Printing and Additive Manufacturing 9(4) (2022) 311-325.

[51] M. Marco, R. Belda, M.H. Miguélez, E. Giner, Numerical analysis of mechanical behaviour of lattice and porous structures, Composite Structures 261 (2021) 113292.

[52] C. Bonatti, D. Mohr, Mechanical performance of additively-manufactured anisotropic and isotropic smooth shell-lattice materials: Simulations & experiments, Journal of the Mechanics and Physics of Solids 122 (2019) 1-26.

[53] E.W. Jost, D.G. Moore, C. Saldana, Evolution of global and local deformation in additively manufactured octet truss lattice structures, Additive Manufacturing Letters 1 (2021) 100010.

[54] F. Günther, F. Hirsch, S. Pilz, M. Wagner, A. Gebert, M. Kästner, M. Zimmermann, Structure-property relationships of imperfect additively manufactured lattices based on triply periodic minimal surfaces, Materials & Design 222 (2022) 111036.

[55] B. Lozanovski, D. Downing, R. Tino, A. Du Plessis, P. Tran, J. Jakeman, D. Shidid, C. Emmelmann, M. Qian, P. Choong, Non-destructive simulation of node defects in additively manufactured lattice structures, Additive Manufacturing 36 (2020) 101593.

[56] C. Wang, C. Wang, Z. Li, Y. He, Z. Zhang, Y. Zhang, Mechanical properties of novel 3D printing 316L stainless steel honeycomb structure reinforced aluminum matrix composites, Intermetallics 181 (2025) 108743.

[57] Z. Kong, X. Wang, N. Hu, Y. Jin, Q. Tao, W. Xia, X.-M. Lin, G. Vasdravellis, Mechanical properties of SLM 316L stainless steel plate before and after exposure to elevated temperature, Construction and Building Materials 444 (2024) 137786.

[58] L. Zhao, J. Zhang, J. Yang, J. Hou, J. Li, J. Lin, Microstructure and mechanical properties of 316L stainless steel manufactured by multi-laser selective laser melting (SLM), Materials Science and Engineering: A 913 (2024) 147053.

[59] G. Haugou, H. Morvan, J.D. Guérin, E. Markiewicz, Evaluation of compression behaviour of 316L SS Gyroid and Diamond structures using SLM process–Experimental programme under static and dynamic compression loadings, International Journal of Impact Engineering 195 (2025) 105147.

[60] Ö.F. Çakır, M. Erdem, Investigation of lattice geometries formed by metal powder additive manufacturing for energy absorption: A comparative study on Ti6Al4V, Inconel 718, and AISI 316L, Machines 13(4) (2025) 316.

[61] P. Płatek, J. Sienkiewicz, J. Janiszewski, F. Jiang, Investigations on mechanical properties of lattice structures with different values of relative density made from 316L by selective laser melting (SLM), Materials 13(9) (2020) 2204.

[62] Z. Luo, Q. Tang, Q. Feng, M. Jin, S. Ma, J. Song, Q. Han, Finite element analysis on mechanical properties of selective laser melting-produced stainless steel 316l lattice structures under impact loading, Journal of Materials Engineering and Performance 32(1) (2023) 438-449.

[63] M. Khan, M.R.u. Haq, Y.S. Ahmed, A. Nazir, Advanced Mechanical Metamaterials: Hybrid Lattice Structures, Design Strategies, Multifunctionality, and Challenges for Additive Manufacturing, Advanced Engineering Materials (2025) 2500308.

[64] S. Thirupathi, A.R. Dixit, P.K. Shaw, S. Dwivedi, Machine learning-assisted stress and deformation prediction for 316 L stainless steel hybrid lattice structures fabricated through laser powder bed fusion, Materials Today Communications 44 (2025) 112037.

[65] Y. Yin, F. Li, D. Zhu, Enhanced energy absorption characteristics of TPMS lattice structures with linear and circular hybrid designs, Engineering Structures 340 (2025) 120759.

[66] M. Mazur, M. Leary, S. Sun, M. Vcelka, D. Shidid, M. Brandt, Deformation and failure behaviour of Ti-6Al-4V lattice structures manufactured by selective laser melting (SLM), The International Journal of Advanced Manufacturing Technology 84(5) (2016) 1391-1411.

[67] T. Yu, X. Li, M. Zhao, X. Guo, J. Ding, S. Qu, T.W.J. Kwok, T. Li, X. Song, B.W. Chua, Truss and plate hybrid lattice structures: Simulation and experimental investigations of isotropy, large-strain deformation, and mechanisms, Materials Today Communications 35 (2023) 106344.

[68] T.A. Alwattar, A. Mian, Development of an elastic material model for BCC lattice cell structures using finite element analysis and neural networks approaches, Journal of composites science 3(2) (2019) 33.

[69] M. Smith, Z.-w. Guan, W. Cantwell, Finite element modelling of the compressive response of lattice structures manufactured using the selective laser melting technique, International Journal of Mechanical Sciences 67 (2013) 28-41.

[70] L. Li, Z. Guo, F. Yang, P. Li, M. Zhao, Z. Zhong, Additively manufactured acoustic-mechanical multifunctional hybrid lattice structures, International Journal of Mechanical Sciences 269 (2024) 109071.

[71] L. Romanelli, C. Santus, I. Senegaglia, F. Tamburrino, M. Controzzi, A. Corrado, M. Perini, D. Kumar, R. De Biasi, M. Benedetti, Lightweight design of polymeric thin-walled components: Latticization and elastic–plastic homogenization, Journal of Materials Research and Technology 36 (2025) 2977-2993.

[72] M.S. Mahmud, M.S. Hassan, A. Marinelarena-Diaz, J.Z. Dantzler, S. Zaman, P.C. Roy, D. Dieguez, D. Leyva, A. Lopez, S. Arroyo, Design and evaluation of selective laser sintering of thermoset lattice structures, Progress in Additive Manufacturing 10(4) (2025) 2227-2246.

[73] A. International, Standard test method for compressive properties of rigid plastics, ASTM international2010.

[74] E. ISO, 527-2; Plastics—Determination of Tensile Properties—Part 2: Test Conditions for Moulding and Extrusion Plastics, Organization of Standardization: Geneva, Switzerland (2012).
[75] M. Abolfathi, A.A. Nia, Optimization of energy absorption properties of thin-walled tubes with combined deformation of folding and circumferential expansion under axial load, Thin-Walled Structures 130 (2018) 57-70.
[76] T. Klöppel, M.W. Gee, W.A. Wall, A scaled thickness conditioning for solid-and solid-shell discretizations of thin-walled structures, Computer methods in applied mechanics and engineering 200(9-12) (2011) 1301-1310.
[77] M. Lei, Y. Wang, Q. Wei, M. Li, J. Zhang, Y. Wang, Micromechanical modeling and numerical homogenization calculation of effective stiffness of 3D printing PLA/CF composites, Journal of Manufacturing Processes 102 (2023) 37-49.
[78] S.L. Omairey, P.D. Dunning, S. Sriramula, Development of an ABAQUS plugin tool for periodic RVE homogenisation, Engineering with Computers 35(2) (2019) 567-577.
[79] G. Sinclair, J. Helms, A review of simple formulae for elastic hoop stresses in cylindrical and spherical pressure vessels: What can be used when, International Journal of Pressure Vessels and Piping 128 (2015) 1-7.
[80] D. Pamplona, P. Goncalves, S. Lopes, Finite deformations of cylindrical membrane under internal pressure, International journal of mechanical sciences 48(6) (2006) 683-696.
[81] Y. Sun, S. Hu, Y. Huang, X. Xue, Analytical stress model for embedded bar-wrapped cylinder concrete pressure pipe under internal load, Thin-Walled Structures 149 (2020) 106540.
[82] M. Staat, D.K. Vu, Limit loads of circumferentially flawed pipes and cylindrical vessels under internal pressure, International journal of pressure vessels and piping 83(3) (2006) 188-196.
[83] Y. Kwon, T. Ponshock, J. Molitoris, Failure loading of metallic and composite cylinders under internal pressure loading, Journal of Pressure Vessel Technology 138(6) (2016) 060903.
[84] A. Bonfanti, S. Syngellakis, A. Bhaskar, Structural analysis of cyclically periodic rings and its application to the mechanics of balloon expandable stents, International Journal of Solids and Structures 185 (2020) 46-56.
[85] G. Chouhan, B. Gunji, Additive manufacturing TPMS lattice structures: Experimental study on airflow resistivity, Results in Materials 20 (2023) 100478.
[86] G. Di Frisco, R.Y. Nooraie, M. Guagliano, S. Bagherifard, Structural design and characterization of hybrid hierarchical lattice structures based on sheet-network Triply periodic Minimal surface topology, Materials & Design 246 (2024) 113336.
[87] M.R. Condruz, T.A. Badea, A. Paraschiv, Numerical and experimental investigation on flexural properties of selective laser melting (SLM) manufactured strut lattices structures from Ti-6Al-4V and Inconel 625, Materials Today Communications 40 (2024) 110150.
[88] I. 13314, ISO 13314 mechanical testing of metals, ductility testing, compression test for porous and cellular metals, (2011).
[89] D.D.I.f.N.e. V., Testing of metallic materials — Tensile test pieces, DIN, Berlin, 2016.